Fall 2020

Fabrication of micro-/nanofluidic models and their applications for enhanced oil recovery mechanism study

Yandong Zhang

Department: Geosciences and Geological and Petroleum Engineering

FABRICATION OF MICRO-/NANOFLUIDIC MODELS AND THEIR APPLICATIONS FOR ENHANCED OIL RECOVERY MECHANISM STUDY

by

YANDONG ZHANG

A DISSERTATION

Presented to the Graduate Faculty of the

MISSOURI UNIVERSITY OF SCIENCE AND TECHNOLOGY

In Partial Fulfillment of the Requirements for the Degree

DOCTOR OF PHILOSOPHY

in

PETROLEUM ENGINEERING

2020

Approved by:

Dr. Baojun Bai, Advisor
Dr. Wen Deng
Dr. Mingzhen Wei
Dr. Ralph Flori
Dr. Shari Dunn-Norman

PUBLICATION DISSERTATION OPTION

This dissertation consists of the following three articles, formatted in the style used by the Missouri University of Science and Technology:

Paper I, which can be found on pages 24-56, has been published in *Journal of Geophysical Research: Solid Earth*.

Paper II, which can be found on pages 57-89, has been published in *Journal Lab on a Chip*.

Paper III, which can be found on pages 90-123, is intended for submission to *Journal ACS Applied Materials & Interfaces*.

ABSTRACT

Micro-/nanofluidic model, as a potential powerful tool, has been used for decades for investigating fluid flow at pore-scale in energy field. It is still increasingly imperative nowadays to use different micromodels to direct observe pore-level fluid flow and analyze mechanisms of different enhanced oil recovery methods. In this work, three main tasks including three dimensional micromodels (1D,2D,3D) are proposed to fabricate and use for investigating different mechanisms of different enhanced oil recovery methods. For 1D capillary tube micromodel, we fabricate and use it to investigate the dynamics of a trapped oil droplet under seismic vibration. Seismic stimulation is a promising technology aimed to mobilize the entrapped non-wetting fluids in the subsurface. The applications include enhanced oil recovery or CO_2 sequestration. For 2D micromodel, we fabricate to mimic unconventional dual-porosity shale-like tight porous media and investigate the fluid flow behavior under such conditions. Unconventional oil reservoirs have become significant sources of petroleum production and have even better potential in the future. Many shale oil systems consist of nanoscale pores and micro-scale fractures that are significantly smaller than those from conventional reservoirs. Therefore, it is increasingly important to investigate fluid flow behaviors in nanoscale channels. For 3D micromodel, we packed and sintered glass beads into quartz tubes to mimic 3D porous media. Because of difficulties for direct visualization, almost all the micromodels available are two-dimensional models which cannot represent real interconnected pore network of a real reservoir porous media. Thus, we build fully transparent 3D models to direct visualize and investigate the in-situ emulsification mechanism for nanogel flooding.

ACKNOWLEDGMENTS

Completion of this Ph.D. dissertation was not possible without the support of my advisors, my committees, my family, and my friends.

Firstly, I would like to express my sincere gratitude to my advisor, Dr. Baojun Bai, for his continuous financial support and critical guidance on the research throughout my doctoral study. Secondly, I would like to thank Dr. Wen Deng for his financial support on the experiments and helpful advice and guidance on paper writing and revision skills.

I would like to sincerely appreciate my committee members: Dr. Mingzhen Wei, Dr. Ralph Flori and Dr. Shari Dunn-Norman. They are always willing to help and motivate me with their expertise and insightful comments. I also sincerely would like to express my thanks and respects to my colleagues and friends: Chao Zeng, Songyuan Liu, Jiaming Geng, Ze Wang, Yifu Long, Chuang Qu, Chuanle Zhou, Jingyang Pu, Na Zhang, Xindi Sun, Xinrui Zhao, Bowen Yu, Haifeng Ding, Mustafa, Ali, Juncheng Liu, Tao Song and for their help in both research and my daily life.

Last but not the least, I am deeply and sincerely grateful to my parents, without their unselfish support and encouragement throughout my study overseas, I would have never been successful in pursuing a Ph.D. degree.

TABLE OF CONTENTS

LIST OF ILLUSTRATIONS

LIST OF TABLES

1. INTRODUCTION

1.1. BACKGROUND OF THE PROBLEM

Multiphase flow through porous media is important for a diverse range of applications, including aquifer remediation, CO_2 sequestration, and oil recovery. These often involve the displacement of an immiscible non-wetting fluid from a porous medium by a wetting fluid, a process known as imbibition. The random structure of the pore space typically leads to complex fluid displacement through the pores; consequently, imbibition can lead to the formation of disconnected ganglia of the non-wetting fluid. Some ganglia can be mobilized and removed from the medium; however, many ganglia become trapped within it. This phenomenon may be particularly important in oil recovery, where over 90% of the oil within a reservoir can remain trapped after primary recovery.

The trapping and releasing of non-wetting droplets in porous media have been studied extensively for many decades. Different methods across a variety of research areas were investigated to mobilize the droplets more efficiently, such as the surface tension reduction used in surfactant flooding (Sheng, Leonhardt, & Azri, 2015), the sweep efficiency improvements used in foam flooding (Farajzadeh, Andrianov, Krastev, Hirasaki, & Rossen, 2012), and the physical vibration used in ultrasound wave stimulation (Alhomadhi, Amro, & Almobarky, 2014; Mullakaev, Abramov, & Abramova, 2015; Z. Wang & Yin, 2017).

When the three-dimensional (3D) pore space is highly disordered, the fluid displacement through it is complicated; this leads to the formation and trapping of discrete ganglia of the non-wetting fluid within the porous medium. Elucidating the physics

underlying ganglion trapping and mobilization is thus critically important; however, despite its enormous industrial relevance, a clear understanding of this phenomenon remains lacking. Unfortunately, systematic experimental investigations of it are challenging, requiring direct measurements of the pore-scale ganglia configurations within a 3D porous medium, combined with measurements of the bulk transport through it, over a broad range of flow conditions. The complex flow behavior leading to nonwetting fluid displacement and trapping has been visualized in two dimensional (2-D) micromodels; however, a complete understanding of the physics underlying the formation and trapping of ganglia requires experimental measurements on three- dimensional (3-D) porous media. Optical techniques typically cannot be used to directly image the flow through such media due to the light scattering caused by the differences in the indices of refraction, when multiple fluid phases are used. Instead, magnetic resonance imaging (MRI) and X-ray microcomputer tomography (X-ray lCT) have been used to visualize either the bulk flow dynamics, or the individual ganglia, within 3-D porous media; however, fast visualization at pore-scale resolution is typically challenging. As a result, despite its broad technological importance, the dependence of ganglion formation and trapping on the pore-scale flow conditions remains unclear.

However, due to the difficulty of direct visualization of the flow process in core-scale, the mechanisms for recovering more oil using different EOR methods cannon be easily investigated. Therefore, in this research, 1D, 2D and 3D micro-/nanofluidic models were fabricated and used to analyze the EOR mechanisms on recovering more capillary-trapped oil ganglia. The whole dissertation is consisted with three publications. Followed are the research objectives of these three tasks.

1.2. SCOPE OF THE WORK

The goal of this PhD work is to fabricate different types of micro-/nano fluidic models and improve the understanding of EOR mechanisms. The overall research scope is shown in a diagram below.

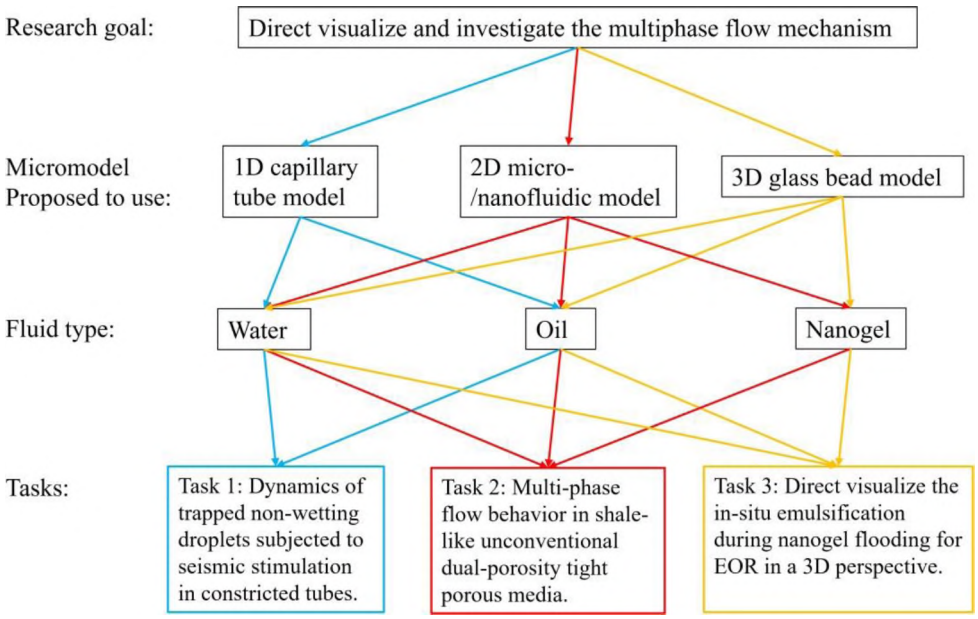

Figure 1.1. Scope of this research

Research Objectives. Three main tasks were carried out to achieve this goal and the objectives of these tasks are listed below.

- Objective 1: Fabricate 1D constricted capillary tubes and implement vibration experiments using shaker system to investigate the dynamics of trapped non-wetting droplets subjected to seismic stimulation in constricted tubes.

- Objective 2: Fabricate 2D glass-silicon-glass micro-/nanofluidic models and implement flooding experiments to investigate multi-phase flow behavior in shale-like unconventional dual-porosity tight porous media.
- Objective 3: Fabricate 3D glass-bead micromodels for direct visualizing and investigating nanogel mechanism for enhanced oil recovery in a 3D perspective.

Paper I: In this paper, we made an experimental effort to obtain reliable data to study the dynamics of non-wetting droplets and validate the previous theoretical fluid dynamics conceptual model in 1D constricted tubes. In our experiments, we considered not only the frequencies and acceleration amplitudes of the seismic stimulation, but also different initial positions of the non-wetting droplets, aspect ratios of the constricted tubes, and viscosities of non-wetting phases. We used a high-speed camera to capture video of the mobilization process of droplets inside capillary tubes, and then manually tracked the displacement of the droplets. Our experimental observation revealed a strong dependence on the critical acceleration amplitude for mobilization on the initial position of a droplet's front menisci. Finally, the reliability of the theoretical model was validated against the experimental data on amplitude amplifications in oscillation experiments and critical amplitudes in mobilization experiments, as dependent on the frequency.

Paper II: In the second paper, we proposed to develop a lab-based, quick-processing and cost-effective 2D micro-/nanofluidic model fabrication method using lift-off process combined with anodic bonding method, which opts out of using any etching methods. A dual-porosity matrix/micro-fracture pattern, which can mimic the topology of the shale with random non-regularly grain shapes was designed by Voronoi algorithm. The pore channel width range is 3 μm to 10 μm for matrices and 100-200 μm for micro-fractures.

Silicon is used as the material to evaporate and deposit onto the glass wafer and then bonded with another glass wafer. The channel depth is the same 250 nm to the deposited silicon thickness. By using the advanced confocal laser scanning microscopy system (CLSM), we directly visualized the pore level flow within micro-/ nano dual-scale channels with fluorescent-dyed water and oil phases.

Paper III: In this work, we used three-dimensional transparent micromodel to directly visualize the in-situ emulsification during nanogel flooding process for EOR after water flooding. By synthesizing the nanogel with fluorescent dye, we found the nanogels adsorbed on the whole oil-water interface to lower the total interfacial energy and emulsify the large oil droplets into small Pickering oil-in-water emulsions. A potential mechanism for in-situ emulsification by nanogels was proposed and discussed.

2. LITERATURE REVIEW

2.1. MICRO-/NANOFLUIDIC MODELS FOR OIL RECOVERY

Micro-/nano fluidic models, also known as micromodels, are semi- or fully transparent devices, which enables the direct visualization of the fluid flow dynamics inside the micro-/nanoconfined channels. The complex fluid flow in the porous media is common in subsurface porous rock and related closely to the oil recovery process as the oil travels through the porous media or the naturally formed micro-fractures before being produced (Blunt et al., 2013). The fluid flow physics in such micro-/nanoscale are dominated by the interfacial forces which is different from that been predicted in larger scale flow domain (Gad-el-Hak, 1999). Due to the difficulties of studying the micro-/nano flow behaviors using core-sample macroscale experiments, micro-/nanofluidic models have become powerful tools to help improve our understandings of the fundamental mechanisms of how the fluid phases behave during the oil recovery processes. The first micromodels developed for oil industry can date back to 1950s (Chatenever & Calhoun Jr, 1952). Since then, aiming for different research purposes, different micromodels were fabricated using different methods and materials such as glass, some transparent polymers and other additive manufacturing technique(Bultreys, De Boever, & Cnudde, 2016; Lifton, 2016), and the pore-level observation and investigation can be visualized under the microscope with cameras(Heshmati & Piri, 2014). Most used micromodels are 2D micromodels with random porous structures in only two-dimensional fluid channels. However, it is not qualified for 2D micromodels to investigate the physics of fluid flow in a real porous media with three-dimensional pore connections and tortuosity that are critical

for the fluid break up phenomena (Krummel, Datta, Münster, & Weitz, 2013). Followed, we give a detailed and comprehensive review of the micro-/nanofluidic model fabrications methods based on the materials and their applications for oil recovery.

2.1.1. Polymeric Materials. PDMS (poly-di-methyl-siloxane) is one of the most used organic materials for fabricating micromodels because its low cost and easy fabrication process that can be easily bonded with glass or another PDMS plate(N. Karadimitriou et al., 2013). It is also ideal for rapid replication of different structures by using soft lithography process so that it has been widely used to fabricate microfluidic devices (N. Karadimitriou et al., 2013; Marin, Grossi, Bianchi, Dubini, & Lacroix, 2017). However, according to the solvent compatibility test(J. N. Lee, Park, & Whitesides, 2003), the PDMS material has a value that similar to hexane and n-heptane, which indicates that the PDMS would swell when contacts with these nonpolar solvents and affect the pore space volume and material balance. Besides, it will deform easily at very low injection pressure as low as 13.8 kPa (0.14 bar) (W. Xu, Ok, Xiao, Neeves, & Yin, 2014). Therefore, it is not a good candidate for conducting flow experiments with oil phases. To remedy these issues and broaden the application possibilities for PDMS models, many improvements including wettability control, protection from oil diffusion by adding epoxy structures or treated with plasma have been reported recently(Bounds et al., 2013; Gitlin, Schulze, Ohla, Bongard, & Belder, 2015; N. K. Karadimitriou, Mahani, Steeb, & Niasar, 2019; Ma, Rivera, Hirasaki, & Biswal, 2011; Rostami, Sharifi, Aminshahidy, & Fahimpour, 2019; Vavra, Zeng, Xiao, Hirasaki, & Biswal, 2018). Except for changing the wettability to oil wet, it can also be changed to mixed wet condition by using the stop-flow-lithography (SFL) technique (H. Lee, Lee, & Doyle, 2015). Although without the remediations, PDMS

models can be used for study of flow behavior that is not sensitive to surface properties, such as single foam flow (Lv, Liu, Ji, Jia, & Jiang, 2018; Lv, Liu, Jia, & Ji, 2020) or foam and emulsion flooding in an oil-wet condition (Conn, Ma, Hirasaki, & Biswal, 2014; Z. Liu et al., 2019), and two phase flow in an geo-material coated condition (Alzahid et al., 2018; Yeh & Juárez, 2019) .

2.1.2. Glass Materials Based Micromodels. To achieve fully transparency and for the superiorities of compatibility with many solvents (Doryani, Malayeri, & Riazi, 2016; Ren, Zhou, & Wu, 2013) high stiffness for handling high pressure fluid flow experiments (Bora, Maini, & Chakma, 2000; Kazemifar, Blois, Kyritsis, & Christensen, 2015; Sohrabi, Tehrani, Danesh, & Henderson, 2001) and the easiness of surface wettability alteration by different methods, (Grate et al., 2013; Maghzi, Mohammadi, Ghazanfari, Kharrat, & Masihi, 2012) the glass itself has long been a preferred microfluidic model substrate. Although glass substrates can also be dry-etched,(Bu, Melvin, Ensell, Wilkinson, & Evans, 2004; Kutchoukov et al., 2004) the low etching rate, low etching selectivity and high facility cost make wet etching a more popular way, which make use of buffered hydrofluoric acid or mixtures of acids as the etchant solutions to etch channels on glass substrates. (Castano-Alvarez et al., 2008; Iliescu, Chen, & Miao, 2008; Wan, Tokunaga, Tsang, & Bodvarsson, 1996) The wettability of the glass surface and the roughness can also be modified by different methods (Mittal, 2007). Besides, the glass microfluidic models can stand very high internal pressures up to a few tens of MPa by different designs (Oosterbroek et al., 2006; Tiggelaar et al., 2007). 2D glass models were used widely to investigate different enhanced oil recovery mechanisms. Nanofluids for enhanced oil recovery was studied in a glass porous network, which concluded that the colloidal silica

particles could reduce the interfacial tension and form water-in-oil emulsions while the fumed silica particles formed the oil-in-water emulsions (S. Li & Torsæter, 2014). A glass micromodel which represents the pore structure of a sandstone reservoir was built with pore throats diameters of 70 μm to study the nanoparticle-stabilized gas-in-brine foams stability and effectiveness (Nguyen, Fadaei, & Sinton, 2014b). Another N_2 foam flooding assisted with nanoparticle and surfactant was also conducted using etched glass model that replicates the actual core structures (Sun et al., 2014). Polymer flooding and Rhamnolipid biosurfactant flooding were also studied using etched glass micromodels (Amani, 2015; Meybodi, Kharrat, & Araghi, 2011). The main drawback is that the isotropic wet etching process cannot reach perfect vertical walls (Castano-Alvarez et al., 2008), yet this imperfect trapezoidal shape can be leveraged to generate a 2.5D micromodel by controlling the etching depths of two neighboring pores (K. Xu, Liang, et al., 2017). The 2.5D micromodels have the pore throats shallower than adjacent pore bodies that mimic the 'convergent-divergent' structures in real porous media. By using this characteristic of the 2.5D model, the dynamic behavior of the microemulsion generated during surfactant flooding and nanoparticles flooding (Tagavifar, Xu, Jang, Balhoff, & Pope, 2017; K. Xu, Agrawal, & Darugar, 2018) and also the Ostwald ripening phenomenon of a bubble(K. Xu, Bonnecaze, & Balhoff, 2017) can be observed and investigated. The 3D glass-based micromodel can be built by lightly sintering the borosilicate glass beads in a square capillary tubing to mimic the real connected porous media in reservoirs (Krummel et al., 2013). By utilizing this 3D model, one can direct visualize the two-phase fluids flow behaviors and a core-shell nanohydrogel for conformance control under a confocal microscope (Datta, Dupin, & Weitz, 2014; Datta, Ramakrishnan, & Weitz, 2014; do

Nascimento, Junior, Paciornik, & Carvalho, 2019; Krummel et al., 2013; L. Zhang et al., 2020).

2.1.3. Silicon Materials Based Micromodels. Silicon-based micromodels are preferred than glass-based micromodels for better quality control and very high geometry resolution (sub-nanometer) and accuracies while keeping the advantages of glass-based micromodels (Marcinkevičius et al., 2001). Pore network patterns can also be generated on silicon wafer surfaces using the similar fabrication techniques as on glass wafers (Iliescu, Taylor, Avram, Miao, & Franssila, 2012). Since silicon has no transparency to visible light, a glass wafer is always being a transparent cover plate anodic bonded over the silicon substrate to make it possible for direct observation under a microscope (Grate, Kelly, Suter, & Anheier, 2012; Q. Wu et al., 2014; Q. Wu et al., 2013). The drawback of this silicon-glass micromodel is the wettability and surface property differences between the silicon and the glass sides. Silanization method was reported as an approach to make the silicon substrate and glass cover the same oil-wet condition (Grate et al., 2013). The silicon-based micromodels have been used widely for investigating multiphase flow mechanisms, such as oil layer role in a three-phase flow (Keller, Blunt, & Roberts, 1997), solution-gas drive mechanism in viscous oils(George, Hayat, & Kovscek, 2005) and the trapping and mobilization mechanism of CO_2 phase(Markus Buchgraber, Kovscek, & Castanier, 2012). Other examples for EOR mechanism study were also investigated using silicon-based micromodels, including the oil mobilization and osmosis mechanism in low-salinity water flooding (Sandengen, Kristoffersen, Melhuus, & Jøsang, 2016; M. Wu et al., 2012) , microbial EOR(Armstrong & Wildenschild, 2012). Most recently, the etched silicon-based nanofluidic models with depth of 5 nm and pore diameter of 60 nm were reported

to investigate the natural gas vaporization in nanoconfined throat and N2 flooding and miscible (CO2) gas flooding for tight oil reservoirs (Jatukaran et al., 2019; Zhong et al., 2018), which quantified the fundamental transport and phase change mechanisms in nanoconfined channels of unconventional porous media.

2.1.4. Geomaterial Based Micromodels. Although different micromodels with complex pore structures has been fabricated to mimic more realistic pore structures in real rock samples, the materials used (silicon, glass, PDMS, etc.) for fabricating the micromodels cannot capture the fluid and rock interactions in terms of surface roughness, wettability and reactive flow, etc(Porter et al., 2015). To modify the micromodel surface properties as realistic as possible, the strategies can be divided into three main categories that are wettability alteration(Chang, Kneafsey, Wan, Tokunaga, & Nakagawa, 2020; Hiller, Ardevol-Murison, Muggeridge, Schröter, & Brinkmann, 2019; Hu, Wan, Kim, & Tokunaga, 2017; H. Lee et al., 2015; Murison et al., 2014; M. Schneider et al., 2010; M.H. Schneider & Tabeling, 2011), using geomaterials (crystal or a section of rock sample) as model substrates or inserting real rock samples into the glass or silicon micromodels(Bowden, Tanino, Akamairo, & Christensen, 2016; Gerami et al., 2017; Porter et al., 2015; Singh et al., 2017; Song, de Haas, Fadaei, & Sinton, 2014; Soulaine, Roman, Kovscek, & Tchelepi, 2017), and coating the micromodel surface with geomaterials(S. G. Lee, Lee, Gupta, Chang, & Doyle, 2016; Song & Kovscek, 2015, 2016; W. Wang, Chang, & Gizzatov, 2017). Recently, some 3D functionalized micromodels were also reported to mimic the real reservoir rock conditions by using 3D printing technique (Ishutov et al., 2017; Kong, Ostadhassan, Liu, Li, & Liu, 2019; Kong, Ostadhassan, Zamiran, et al., 2019; H. Li, Raza, Ge, Lu, & Zhang, 2020). However, it is

harder to obtain good quality control when using those geo-materials than polymer, glass and silicon-based micromodels due to the limitations of their mechanical properties.

2.1.5. Additive Manufacturing Based Micromodels. Additive manufacturing mainly refers to stereolithography, or 3D printing technique, has been used to construct 3D micromodels by depositing different materials layer by layer onto a position- controllable stage(Bultreys et al., 2016; Crandall, Ahmadi, Leonard, Ferer, & Smith, 2008). The foam flooding for EOR was reported using a 3D printed porous medium recently (Osei-Bonsu, Grassia, & Shokri, 2017). Additive manufacturing using electron- beam physical vapor deposition was reported recently to build a 2D glass-silicon-glass micro-/nanofluidic model with dual-porosity porous medium (Y. Zhang et al., 2019). Other additive manufacturing methods involve the liquid solidification or melted material to form the predesigned structure. Although additive manufacturing has been widely used to construct 3D structures of a variety of materials, such as resin, metal, and hydrogel, its application in making micromodels for multiphase flow study is still in an early stage (Au, Huynh, Horowitz, & Folch, 2016). With larger selection of optically transparent materials and more accurate printing resolution, this method could be very promising in constructing micromodel for fluid flow study in a 3D perspective.

2.2. SEISMIC STIMULATION FOR EOR

The trapping and releasing of non-wetting droplets in porous media has been studied extensively for many decades. Different methods across a variety of research areas were investigated to mobilize the droplets more efficiently, such as the surface tension reduction used in surfactant flooding (Sheng et al., 2015), the sweep efficiency

improvements used in foam flooding (Farajzadeh et al., 2012), and the physical vibration used in ultrasound wave stimulation (Alhomadhi et al., 2014; Mullakaev et al., 2015; Z. Wang & Yin, 2017). Due to the high cost, potential environmental contamination, and conformance control limitations of methods such as chemical flooding, enthusiasm about earthquake-induced seismic stimulation to geologic formations has increased recently. Passing seismic waves were found to be capable of mobilizing non-wetting droplets trapped in capillaries by adding a seismic-wave-induced inertial force to the background pressure gradient to help overcome the capillary force and unblock inaccessible pores (I. A. Beresnev, 2006). Because of this mechanism, seismic dislodgement of droplets was proposed for various applications, such as using seismic stimulation to mobilize residual oil for enhanced oil recovery (I. A. Beresnev & Deng, 2010; Jeong, Kallivokas, Kucukcoban, Deng, & Fathi, 2015; Pride, Flekkøy, & Aursjø, 2008; P. M. Roberts, 2005; P.M. Roberts, Esipov, & Majer, 2003), estimating the impact of earthquakes on CO_2 residual trapping for CO_2 sequestration (W. Deng & Cardenas, 2013), enhancing the permeability of geological formations (Elkhoury, Brodsky, & Agnew, 2006; Elkhoury, Niemeijer, Brodsky, & Marone, 2011; Geballe, Wang, & Manga, 2011; Manga et al., 2012; C. Y. Wang & Manga, 2010), and altering seismic wave propagation through fluid-structure interaction (Ali, Berteussen, Small, & Barkat, 2010; Lambert, Schmalholz, Saenger, & Steiner, 2009; T. M. Müller, Gurevich, & Leb edev, 2010; Saenger et al., 2009). Although this method has shown great potential in various applications, the physical mechanism for droplet mobilization enhanced by seismic stimulation at the pore-scale level remains unclear.

2.2.1. Theoretical Study. Hilpert, Jirka, and Plate (2000) proposed that a volume of capillary-trapped oil ganglia can be mobilized to its maximum at its resonance frequency using elastic wave excitation. Iassonov and Beresnev (2003) built a model that considered the yield-stress behavior of the flow of fluids while being mobilized through vibrations in straight tubes. To further clarify the understanding of the physical mechanism, an oscillator model was later proposed by I. A. Beresnev (2006) that could be used to depict the mobilization. However, the viscous effect caused by the water film on the capillary tube wall was ignored. Although I. A. Beresnev and Deng (2010) later improved their model by considering the viscous force exerted on the droplet, the assumption that the droplet maintained constant length and velocity profiles was not convincing in a constricted tube. They also simply assumed a constant pressure gradient condition, which is not true in a single constricted tube that has a varied pressure gradient inside, even for laminar flow, due to the convergent-divergent geometry. A well- developed theoretical model in a constricted tube built on a moving-boundary control volume was proposed by W. Deng and Cardenas (2013), where the momentum balance equation was established by considering the derivative of the momentum change with respect to time, the pressure force of the upstream and downstream menisci, the capillary force of the upstream and downstream menisci, the viscous force and pressure force along the tube wall, and the oscillatory inertial force due to the seismic stimulation. A frequency-based criterion was also proposed for the appropriate usage of the Poiseuille flow assumption in their model.

2.2.2. Numerical Study. Graham and Higdon (2000) quantitatively demonstrated the unplugging process of a trapped non-wetting phase by developing computational fluid dynamics (CFD) models based on one-dimensional sinusoidal axisymmetric channels. Igor

A Beresnev et al. (2005) demonstrated the release of an entrapped blob by vibrations through a CFD simulation in constricted pores. Hilpert (2007) further used Lattice–Boltzmann (LB) modeling to perform numerical experiments and validated the analytical solutions of the resonance of droplets against the LB model. Using concepts from thermodynamics, Kurzeja and Steeb (2014) developed a model to describe the response of wetting clusters to seismic stimulation. This model can be upscaled well to describe the dynamics of wetting clusters in unsaturated soils, but it cannot describe the mobilization behavior of non-wetting droplets in porous media. Deng and Cardenas's theoretical model was validated against the CFD simulations by W. Deng and Cardenas (2013).

2.2.3. Experimental Study. Although considerable progress was made both numerically and theoretically, laboratory evidence of the seismic stimulation in constricted tubes for ganglia mobilization remained limited. Along with the simulation results, Igor A Beresnev et al. (2005) experimentally observed the mobilization of entrapped organic ganglia in a two-dimensional (2D) micromodel with pore constrictions etched on two glass plates. By fixing the vibration frequency and acceleration amplitude separately, the highest rate of organic ganglia production was found at 10 Hz, 3.5 m/s^2 and 30 Hz, 7.5 m/s^2, respectively. W. Li, Vigil, Beresnev, Iassonov, and Ewing (2005) also designed a 2D glass micromodel to show evidence that vibrations will be most effective at greater amplitudes and lower frequencies. Then, Pride et al. (2008) incorporated this mechanism into an LB model, simulating that seismic stimulation will increase residual oil production under sufficiently large acceleration amplitudes and sufficiently small stimulation frequencies. Chrysikopoulos and Vogler (2006) used a monolayer of packed glass beads to study acoustically enhanced ganglia dissolution and mobilization. The flow rate and capillary

number were correlated to the efficiency of acoustically stimulated ganglia dissolution and mobilization. Hsu, Katz, and Hilpert (2012) used a planar laser-induced fluorescence technique to investigate the frequency response of the blob in three-dimensional (3D) porous media under seismic stimulation, and they verified their theory by predicting the resonance frequency. These 2D and 3D experiments were important in understanding the mechanism of seismic stimulation for enhanced multiphase flow in complex geometries, but they cannot directly contribute to the understanding of the basic mechanism of seismic stimulation in a single constricted tube, which is fundamentally important for understanding the mechanism of the permeability changes of porous media subjected to seismic stimulation.

More recently, I. Beresnev, Gaul, and Vigil (2011) experimentally demonstrated the unplugging phenomenon of a non-wetting droplet under a critical longitudinal vibration amplitude within a constricted capillary tube. However, the reported threshold pressure and ganglion lengths appeared to be inconsistent with the Young-Laplace equation. Therefore, we cannot use their data to further validate the theoretical model developed by W. Deng and Cardenas (2013).

2.3. MICROMODELS FOR UNCONVENTIONAL RESERVOIRS

Followed sections reviewed different micromodel fabrications for unconventional reservoirs.

2.3.1. Characteristics of Unconventional Reservoirs. Unconventional reservoirs, including shales and other types of tight formations, which intrinsically have much lower permeability than conventional reservoirs with micro-/nano scale dual-porosity features,

can exhibit highly varying properties within microscopic confinement. According to the average pore-throat diameter size of unconventional shale and other tight oil/gas reservoirs, the ratio of pore surface area to the pore volume which can be 50×10^{4} cm^{-1} (over 700 if represented by the ratio of channel width to depth in a microfluidic model), is much larger than that of conventional porous media which can be 1.8×10^{-4} cm^{-1} (nearly 0.01 if represented by the ratio of channel width to depth in a microfluidic model)(Boruah, Rasheed, Mendhe, & Ganapathi, 2019; Nelson, 2009). Hence, the hypothesized surface interfacial phenomena dominated fluid flow make the liquid and gas transportation through shale are still uncertain.(Civan, Rai, & Sondergeld, 2011)

2.3.2. Dual-Porosity Micromodel Fabrications. Microfluidic model, as a powerful pore-scale level approach is needed to better understand the flow behavior and mechanism within the heterogeneous porous media of the shale-like tight oil/gas reservoirs. Although some of microfluidic devices possessing dual-scale matrix/fractures network features have been built by using different fabricating method,(M Buchgraber, Al-Dossary, Ross, & Kovscek, 2012; Conn et al., 2014; K. Xu, Zhu, Colon, Huh, & Balhoff, 2017; Yun, Ross, Roman, & Kovscek, 2017) the channels are all in micro scale
for any dimensions and not having large width-to-depth ratio (2-26), which cannot represent fluid pathways of shale or tight duel-scale reservoirs.

2.3.2.1. PDMS based micromodels. Until recently, though the first micro-/nano PDMS-glass and quartz-glass duel-scale microfluidic models come up to represent dual scale shale, (Kelly, Torres-Verdín , & Balhoff, 2016) the width-to-depth ratio (1-25) still stay small. Besides, the fabrication method cannot guarantee oil flow on PDMS-glass model and high-pressure experiments on glass-glass model due to the bonding issue.

Although PDMS micromodel now can realize sub-100 nm dimensions, (Kelly et al., 2016; Peng & Li, 2016) it is still not a proper candidate for conducting experiments involving organic nonpolar fluids,(J. N. Lee et al., 2003) which is ubiquitous in many petroleum and environmental scenarios.(Geng, Ding, Han, Wu, & Bai, 2018; Geng, Pu, Wang, & Bai, 2018; Herrick, McClean, Meeker, Baxter, & Weymouth, 2004; Weaver, 1984)

2.3.2.2. Silicon based micromodels. Nonorganic materials based silicon-glass or glass-glass microfluidic models have risen in response and widely been used to fabricate micro-/nanofluidic models capable of handling harsh physical and chemical conditions for energy fields.(Alfi, Nasrabadi, & Banerjee, 2016; Gunda, Bera, Karadimitriou, Mitra, & Hassanizadeh, 2011; Lefortier, Hamersma, Bardow, & Kreutzer, 2012; Lin, Yu, Wang, Tu, & Wang, 2010; Parsa, Yin, & Ozkan, 2015) For silicon-glass ones, since silicon has no transparency to visible light, a glass wafer is always being a transparent cover plate anodic bonded over the silicon substrate to make it possible for direct observation under a microscope.(Grate et al., 2012; Q. Wu et al., 2014; Q. Wu et al., 2013)

2.3.2.3. Glass based micromodels. To achieve fully transparency and for the superiorities of compatibility with many solvents,(Doryani et al., 2016; Ren et al., 2013) high stiffness for handling high pressure fluid flow experiments(Bora et al., 2000; Kazemifar et al., 2015; Sohrabi et al., 2001) and the easiness of surface wettability alteration by different methods,(Grate et al., 2013; Maghzi et al., 2012) the glass itself has long been a preferred microfluidic model substrate. The choice between the two is mainly depending on the goals and needs. Silicon substrate would be chosen when one needs more precise channel sizes and straight channel side walls when using dry etching method.(Kawai, Yamaguchi, Nakahara, & Shoji, 2010) Although glass substrates can also

be dry-etched,(Bu et al., 2004; Kutchoukov et al., 2004) the low etching rate, low etching selectivity and high facility cost make wet etching a more popular way, which make use of buffered hydrofluoric acid or mixtures of acids as the etchant solutions to etch channels on glass substrates. (Castano-Alvarez et al., 2008; Iliescu et al., 2008; Wan et al., 1996) The main drawback is that the isotropic wet etching process cannot reach perfect vertical walls,(Castano-Alvarez et al., 2008) yet this imperfect trapezoidal shape can be leveraged to generate a 2.5 D micromodel by controlling the etching depths of two neighboring pores.(K. Xu, Liang, et al., 2017) Other fabrications of semi or fully transparent microfluidic models for energy and other fields can be found elsewhere in details.(Anbari et al., 2018; X. Chen & Zhang, 2018; Iliescu et al., 2012; N. Karadimitriou & Hassanizadeh, 2012; Kovarik & Jacobson, 2009; Lifton, 2016)

2.4. NANOPARTICLES FOR EOR

Followed sections reviewed current EOR method by using nanoparticles and current micromodels proposed to conduct experiments involved nanotechnology.

2.4.1. Nanoparticles Applications. As the fossil energy remains one of the most essential global resources, the demand for oil and natural gas resources is still urgently rising in next few decades (Pan et al., 2020; Ramasamy & Amanullah, 2020; ShamsiJazeyi, Miller, Wong, Tour, & Verduzco, 2014). It is well-known that there is still much oil, about 60%-70%, left in subsurface after primary and secondary recovery trapped by capillary force (Green & Willhite, 1998). Therefore, different enhanced oil recovery (EOR) methods, such as thermal, miscible and chemical methods were then applied to extract 30%-60% more oil from the reservoir (Thomas, 2008). Nevertheless, new technologies were still

inevitably to develop due to the high demand of the energy. Nanoparticles (NPs) have been very attractive to be studied and applied in many areas such as civil engineering (Ganesh, 2012), medical applications (Kubik, Bogunia-Kubik, & Sugisaka, 2005; Kumari, Yadav, & Yadav, 2010; Liong et al., 2008; Soppimath, Aminabhavi, Kulkarni, & Rudzinski, 2001), food science(Duncan, 2011) and solar cells(Saunders & Turner, 2008). Recently, it also appeared to be successful alternatives for improving different engineering processes in the oil and gas industry, including reservoir characterization(Rahmani et al., 2015), reservoir management(Turkenburg, Chin, & Fischer, 2012), drilling(Hoelscher, De Stefano, Riley, & Young, 2012; J. Zhang et al., 2015) and completion process(Mohammadizadeh, Pourabbas, Mahmoodian, Foroutani, & Fallahian, 2014). Besides, injection of nanoparticles in the form of nanodispersions were also caught attention of being used as an potential enhanced oil recovery method due to its small size (1-100 nm) and many other promising interfacial properties(Alomair, Matar, & Alsaeed, 2015; Bennetzen & Mogensen, 2014; Cheraghian & Hendraningrat, 2016; Hashemi, Nassar, & Almao, 2014; Hendraningrat & Torsaeter, 2014).

2.4.2. Nanoparticle Potential Mechanisms for EOR. Currently, it is widely accepted that the NPs could adsorb onto two miscible fluid interface(Bhattacharya & Basu, 2013; Du, Glogowski, Emrick, Russell, & Dinsmore, 2010; C. Tian, Feng, Cho, Datta, & Prud'homme, 2018), which helps recover more oil by reducing the interfacial tension (IFT)(Cheraghian & Hendraningrat, 2016; Du et al., 2010; X. Li et al., 2014; Saigal et al., 2013), altering wettability(Cao, Mohammed, & Babadagli, 2017; S. Li, Torsæter, Lau, Hadia, & Stubbs, 2019; Roustaei, 2014), modifying disjoining pressure(Alex Nikolov, Kondiparty, & Wasan, 2010; AD Nikolov & Wasan, 2003) and stabilizing Pickering

emulsions(Shen & Ye, 2011; Son, Kim, Lee, Kim, & Sung, 2014; T. Zhang, Davidson, Bryant, & Huh, 2010). However, the mechanisms of nanoparticles for enhanced oil recovery are still not well understood so that field applications were not widely applied and remained mostly based on laboratory core flooding research(Agista, Guo, & Yu, 2018; Ding, Zhang, Zhang, Wei, & Bai, 2019; Hendraningrat, Li, & Torsæter, 2013; Kanj, Rashid, & Giannelis, 2011).

Among the suggested mechanisms of NPs for EOR, oil-in-water Pickering emulsion generation and stabilization by NPs have been increasingly researched in recent years due to its better resistance under harsh conditions than surfactants and can be injected for improved mobility control at high salinity condition(I. Kim et al., 2017; T. Zhang et al., 2010). However, most of current used NPs are inorganic NPs and can be tailor-made for specific surface modifications with grafted polymer chains, without which the stable Pickering emulsion with high resistance to harsh conditions cannot be formed(Saha, Uppaluri, & Tiwari, 2018; ShamsiJazeyi et al., 2014; S. Tian, Gao, Liu, Kang, & Yang, 2020; Zhou et al., 2020; Zhou et al., 2019). These modifications significantly raised the budget and increased production time. Except for polymer grafted NPs, another choice is the hybrid polymer nanofluid suspension by direct mixing or blending nanoparticles into the polymer. Although it was reported easily synthesized, it is hard to obtain a uniform dispersion due to the strong tendency of nanoparticle aggregation in polymer matrix (Gbadamosi et al., 2018).

2.4.3. In-situ Emulsification by Polymeric Nanoparticles. Compared to Pickering emulsion stabilized by rigid NPs, the soft nanogel stabilized Pickering emulsions have gained much attention due to their temperature and pH-responsive properties (Geng

et al., 2019). When adsorbing onto oil-water interface, their inherent high hydrophilicity, sufficient steric repulsion can prevent coalescence of oil droplets, which enables the long-term stabilization of Pickering emulsions, even in high temperatures (Destribats et al., 2011; Geng, Pu, et al., 2018). Other than injecting repared micro/nano emulsions or NP-stabilized surfactant or foam injections for EOR (Almahfood & Bai, 2018), it was also observed that the solely nanogel dispersion injection after water flooding in a sandstone could generate in-situ shear-induced oil-in- water emulsion as the produced effluent after water flooding was in bulk oil phase while in oil-in-water emulsion state after nanogel flooding. The adsorbed nanogel layer ensured the emulsified oil droplets were stable and isolated before being produced to the surface (Geng, Ding, et al., 2018).

2.4.4. Microfluidic Approaches for Nanogel In-situ Emulsification Study. Due to the difficulty of direct visualization of the fluid flow process within a core, the in-situ emulsification phenomenon during nanogel flooding cannot be easily visualized (Qin, Goual, Piri, Hu, & Wen, 2020). Therefore, microfluidic models have become a powerful tool to investigate the microscopic mechanisms of NPs for EOR, including the in-situ emulsification (S. Li, Hendraningrat, & Torsaeter, 2013). Since most available microfluidic research were based on a 2D micromodel that is inherently difficult to study emulsion or foam flow due to the limited pore geometry(Conn et al., 2014; Y. Zhang et al., 2019), most of which focused only on the investigations of IFT reduction and wettability alteration caused by NPs(Cheraghian, Kiani, Nassar, Alexander, & Barron, 2017; Nguyen, Fadaei, & Sinton, 2014a; Tajik, Shahrabadi, Rashidi, Jalilian, & Yadegari, 2018; K. Xu, Zhu, Huh, & Balhoff, 2015) while few discussed the NP stabilized emulsion flow using emulsion generator or 2.5D micromodel(K. Xu et al., 2018; K. Xu, Liang, et al., 2017; K.

Xu et al., 2015; Yang et al., 2020). The most recent 3D transparent micromodel packed with glass beads were only used to direct visualize the two-phase fluids flow behaviors and a core-shell nanohydrogel for conformance control under a confocal microscope(Datta, Dupin, et al., 2014; do Nascimento et al., 2019; Krummel et al., 2013; L. Zhang et al., 2020). To our best knowledge, no research has been done to direct visualize the in-situ emulsification during nanogel flooding using a 3D micromodel, which is a more proper candidate to study the emulsification mechanism with more realistic discontinuous pore throats and pore bodies.

PAPER

I. EXPERIMENTAL INVESTIGATION OF THE DYNAMICS OF TRAPPED NON-WETTING DROPLETS SUBJECTED TO SEISMIC STIMULATION IN CONSTRICTED TUBES

ABSTRACT

Multi-phase fluid flow in porous media can be affected by the dynamic stressing caused by earthquakes or human-made blasts. Changes in the permeability of porous media can be induced by the mobilization of trapped colloids, immiscible droplets or bubbles due to such dynamic stressing. In order to analyze the mechanism of this seismic-induced mobilization, a theoretical fluid dynamics conceptual model had been developed to describe this phenomenon in constricted tubes. In the research presented in this paper, we made an experimental effort to obtain reliable data to study the dynamics of non-wetting droplets and validate the previous theoretical fluid dynamics conceptual model in constricted tubes. In our experiments, we considered not only the frequencies and acceleration amplitudes of the seismic stimulation, but also different initial positions of the non-wetting droplets, aspect ratios of the constricted tubes, and viscosities of non- wetting phases. We used a high-speed camera to capture video of the mobilization process of droplets inside capillary tubes, and then manually tracked the displacement of the droplets. Our experimental observation revealed a strong dependence on the critical acceleration amplitude for mobilization on the initial position of a droplet's front menisci. Finally, the reliability of the theoretical model was validated against the experimental data on

amplitude amplifications in oscillation experiments and critical amplitudes in mobilization experiments, as dependent on the frequency.

1. INTRODUCTION

The trapping and releasing of non-wetting droplets in porous media has been studied extensively for many decades. Different methods across a variety of research areas were investigated to mobilize the droplets more efficiently, such as the surface tension reduction used in surfactant flooding (Sheng et al., 2015), the sweep efficiency improvements used in foam flooding (Farajzadeh et al., 2012), and the physical vibration used in ultrasound wave stimulation (Alhomadhi et al., 2014; Mullakaev et al., 2015; Z. Wang & Yin, 2017).

Due to the high cost, potential environmental contamination, and conformance control limitations of methods such as chemical flooding, enthusiasm about earthquake-induced seismic stimulation to geologic formations has increased recently. Passing seismic waves were found to be capable of mobilizing non-wetting droplets trapped in capillaries by adding a seismic-wave-induced inertial force to the background pressure gradient to help overcome the capillary force and unblock inaccessible pores (I. A. Beresnev, 2006). Because of this mechanism, seismic dislodgement of droplets was proposed for various applications, such as using seismic stimulation to mobilize residual oil for enhanced oil recovery (I. A. Beresnev & Deng, 2010; Jeong et al., 2015; Pride et al., 2008; P. M. Roberts, 2005; P.M. Roberts et al., 2003), estimating the impact of earthquakes on CO_2 residual trapping for CO_2 sequestration (W. Deng & Cardenas, 2013), enhancing the permeability

of geological formations (Elkhoury et al., 2006; Elkhoury et al., 2011; Geballe et al., 2011; Manga et al., 2012; C. Y. Wang & Manga, 2010), and altering seismic wave propagation through fluid-structure interaction (Ali et al., 2010; Lambert et al., 2009; T. M. Müller et al., 2010; Saenger et al., 2009). Although this method has shown great potential in various applications, the physical mechanism for droplet mobilization enhanced by seismic stimulation at the pore-scale level remains unclear. Numerous researchers have attempted to clarify this mechanism. Hilpert et al. (2000) proposed that a volume of capillary-trapped oil ganglia can be mobilized to its maximum at its resonance frequency using elastic wave excitation. Hilpert (2007) further used Lattice–Boltzmann (LB) modeling to perform numerical experiments and validated the analytical solutions of the resonance of droplets against the LB model. Graham and Higdon (2000) quantitatively demonstrated the unplugging process of a trapped non- wetting phase by developing computational fluid dynamics (CFD) models based on one- dimensional sinusoidal axisymmetric channels. Using concepts from thermodynamics, Kurzeja and Steeb (2014) developed a model to describe the response of wetting clusters to seismic stimulation. This model can be upscaled well to describe the dynamics of wetting clusters in unsaturated soils, but it cannot describe the mobilization behavior of non-wetting droplets in porous media. Iassonov and Beresnev (2003) built a model that considered the yield-stress behavior of the flow of fluids while being mobilized through vibrations in straight tubes. Igor A Beresnev et al. (2005) demonstrated the release of an entrapped blob by vibrations through a CFD simulation in constricted pores. To further clarify the understanding of the physical mechanism, an oscillator model was later proposed by I. A. Beresnev (2006) that could be used to depict the mobilization. However, the viscous effect caused by the water film on the capillary

tube wall was ignored. Although I. A. Beresnev and Deng (2010) later improved their model by considering the viscous force exerted on the droplet, the assumption that the droplet maintained constant length and velocity profiles was not convincing in a constricted tube. They also simply assumed a constant pressure gradient condition, which is not true in a single constricted tube that has a varied pressure gradient inside, even for laminar flow, due to the convergent-divergent geometry. A well-developed theoretical model in a constricted tube built on a moving-boundary control volume was proposed by W. Deng and Cardenas (2013), where the momentum balance equation was established by considering the derivative of the momentum change with respect to time, the pressure force of the upstream and downstream menisci, the capillary force of the upstream and downstream menisci, the viscous force and pressure force along the tube wall, and the oscillatory inertial force due to the seismic stimulation. A frequency-based criterion was also proposed for the appropriate usage of the Poiseuille flow assumption in their model. Finally, Deng and Cardenas's theoretical model was validated against the CFD simulations.

Although considerable progress was made both numerically and theoretically, laboratory evidence of the seismic stimulation in constricted tubes for ganglia mobilization remained limited. Along with the simulation results, Igor A Beresnev et al. (2005) experimentally observed the mobilization of entrapped organic ganglia in a two-dimensional (2D) micromodel with pore constrictions etched on two glass plates. By fixing the vibration frequency and acceleration amplitude separately, the highest rate of organic ganglia production was found at 10 Hz, 3.5 m/s^2 and 30 Hz, 7.5 m/s^2, respectively. W. Li et al. (2005) also designed a 2D glass micromodel to show evidence that vibrations will be most effective at greater amplitudes and lower frequencies. Then, Pride et al. (2008)

incorporated this mechanism into an LB model, simulating that seismic stimulation will increase residual oil production under sufficiently large acceleration amplitudes and sufficiently small stimulation frequencies. Chrysikopoulos and Vogler (2006) used a monolayer of packed glass beads to study acoustically enhanced ganglia dissolution and mobilization. The flow rate and capillary number were correlated to the efficiency of acoustically stimulated ganglia dissolution and mobilization. Hsu et al. (2012) used a planar laser-induced fluorescence technique to investigate the frequency response of the blob in three-dimensional (3D) porous media under seismic stimulation, and they verified their theory by predicting the resonance frequency. These 2D and 3D experiments were important in understanding the mechanism of seismic stimulation for enhanced multiphase flow in complex geometries, but they cannot directly contribute to the understanding of the basic mechanism of seismic stimulation in a single constricted tube, which is fundamentally important for understanding the mechanism of the permeability changes of porous media subjected to seismic stimulation.

More recently, I. Beresnev et al. (2011) experimentally demonstrated the unplugging phenomenon of a non-wetting droplet under a critical longitudinal vibration amplitude within a constricted capillary tube. However, the reported threshold pressure and ganglion lengths appeared to be inconsistent with the Young-Laplace equation. Therefore, we cannot use their data to further validate the theoretical model developed by W. Deng and Cardenas (2013).

In this research, we implemented an experimental approach to quantitatively investigate the dynamics of trapped non-wetting droplets subjected to the shaking of constricted capillary tubes. We considered not only the frequencies and acceleration

amplitudes of the shaking, but also the different initial positions of the non-wetting droplets (i.e., the initial position of the droplet menisci), aspect ratios of the constricted tubes, and viscosities of the non-wetting fluids. By using a shaker system combined with a high-speed camera, the whole mobilization process of the droplet was captured and then analyzed using Phantom Camera Control software. Later, we manually tracked the motion of the droplet's meniscus and then compared the experimental data with calculations of the theoretical model proposed by W. Deng and Cardenas (2013). Our experimental work validated the reliability of the theoretical model by considering these parameters and provided reliable data that would benefit further research in this area.

2. METHODOLOGY

2.1. CONCEPT OF THEORETICAL MODEL

The conceptual figure of the constricted tube used in the experimental study can be found in Figure 1. The external pressure drop in Figure 1 moves from left to right. Therefore, we define the left side as "upstream" or "back" and the right side as "downstream" or "front." We further define the narrowest part of the tube as the "throat."

The middle section of the tube is sinusoidally shaped and connects to straight tubes on the left and right. The profile of the tube can be given by:

$$\lambda(x) = \begin{cases} r_{max}, & L_1 \le x < -L \\ r_{min}\left[\frac{r_{max}}{r_{min}} + \left(1 - \frac{r_{max}}{r_{min}}\right)\left(1 + \cos\left(\pi \frac{x}{L}\right)\right)\right], & -L \le x < L \\ r_{max}, & -L \le x \le L_2 \end{cases} \quad (1)$$

where 2L is the spatial wavelength of the sinusoidally curved portion.

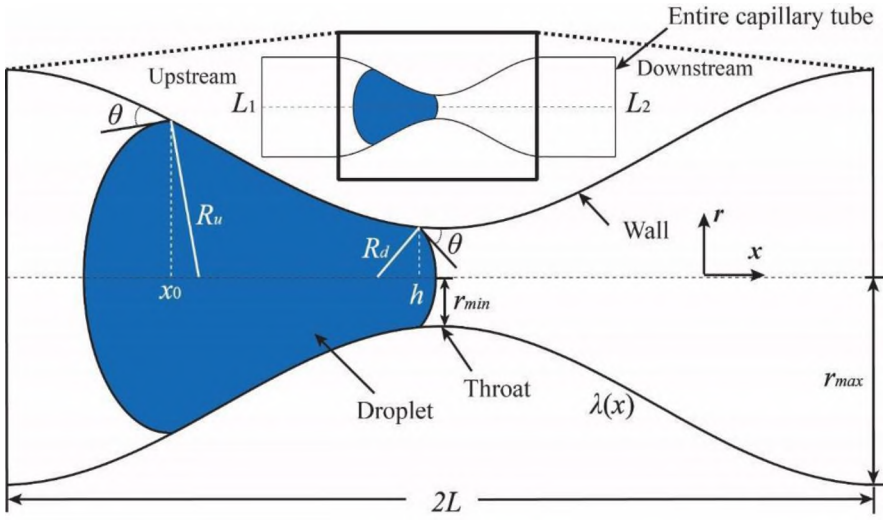

Figure 1. Conceptual geometry of the constricted tube with the trapped droplet. A non-wetting droplet is initially entrapped in the constricted tube. Ru is the radius of the curvature of the upstream meniscus; Rd is the radius of the curvature of the downstream meniscus; θ is the contact angle of the wall; x_0 is the x coordinate of the three-phase contact position at the upstream meniscus; h is the x coordinate of the three-phase contact position at the downstream meniscus; L_1 and L_2 are the positions of the left and right ends of the tube, respectively; $\lambda(x)$ refers to the wall profile of the tube. This figure is modified from Deng and Cardenas (2013)

The macroscopic momentum balance equation on this moving-boundary control volume is:

$$\rho_n \frac{d}{dt} \int_V \bar{v}_n dV = F_x + F_p + F_a + P_{nu} A_u - P_{nd} A_d \tag{2}$$

The left-hand side specifies the momentum accumulation term within the control volume V, ρ_n is the density of the non-wetting fluid and v_n (average) is the cross-sectional mean velocity of the non-wetting droplet. On the right-hand side, F_x, F_p, F_a, $P_{nu}A_u$ and $P_{nd}A_d$ denote the viscous drag, the pressure force along the wetting/non-wetting interface (or along the tube wall if there is no film present), the oscillatory inertial force, the entrance force due to pressure and the exit force due to pressure, respectively. P_{nu} and P_{nd} are the pressures at the upstream and downstream menisci of the non-wetting fluid, and A_u and A_d

are the cross-sectional areas at the three-phase contact positions for the upstream and downstream menisci of the non-wetting fluid.

Assuming a Hagen-Poiseuille flow profile within the tube and expressing each term of Equation (1) as a function front meniscus displacement h, the governing equation for the motion of the droplet can be given as a highly nonlinear ordinary differential equation:

$$\rho_n\left[h - x_0 + \frac{2}{3}\left(\lambda(x_0) + \lambda(h) - 2t_f\right)\right]\frac{d^2h}{dt^2} + \rho_n\left(1 - \frac{\left(\lambda(h) - t_f\right)^2}{\left(\lambda(x_0) - t_f\right)^2}\right)\left(\frac{dh}{dt}\right)^2 +$$

$$8\mu_n int1(h)\frac{dh}{dt} = \Delta P_e - \Delta P_c - \frac{8\mu_w}{\pi}S(h)\frac{dh}{dt}\left(\int_{L_1}^{x_0}\frac{1}{\lambda^4(x)}dx + \int_h^{L_2}\frac{1}{\lambda^4(x)}dx\right) - 2c \cdot int3(h) +$$

$$\rho_n A \cdot sin(2\pi ft)(h - x_0) + \rho_w A \cdot sin(2\pi ft)(x_0 - L_1 + L_2 - h) \quad (3)$$

where x_0 is the position of the three-phase contact position at the upstream meniscus (Figure 1); t_f is the thickness of the wetting film deposited between the wall and the non-wetting phase; ΔP_e is the pressure drop across the constricted tube; ΔP_c is the capillary pressure difference between the downstream and upstream menisci; μ_w is the viscosity of the wetting phase; A is the amplitude of the oscillatory acceleration applied to the fluid and f is the frequency of the oscillatory acceleration. A simple version of the description of the theoretical model also can be found in the Supporting Information (SI). The more complex functions, $S(h)$, $int1(h)$, $int2(h)$ and $int3(h)$, are further explained in the SI.

The momentum balance in Equation (2) describing the dynamics of the downstream meniscus of a trapped droplet is a second-order nonlinear ordinary differential equation. A fourth-order Runge-Kutta method was used to numerically solve the initial value problem. The initial condition was such that a non-wetting droplet of a certain mass was initially trapped in a stable configuration. Its downstream meniscus was therefore slightly upstream of the throat and was stationary.

The initial conditions were given by Deng and Cardenas (2013):

$$h = \varepsilon \text{ at } t = 0 \tag{4}$$

$$x_0 = \delta \text{ at } t = 0 \tag{5}$$

$$\frac{dh}{dt} = 0 \text{ at } t = 0 \tag{6}$$

where ε and δ are the initial positions of the downstream and upstream menisci, respectively. This model was compared against the corresponding CFD simulations.

2.2. EXPERIMENTAL SETUP

We divided our experiments into two parts. One part was to study the droplet dynamics in the constriction of the tube when the droplet cannot pass through the throat, which we call oscillation. The second part was to study the droplet passing through the throat after gradually increasing the acceleration amplitude of the vibration, which we call mobilization. For each part, we chose five different frequencies from 10 Hz to 50 Hz, with an interval of 10 Hz, as well as different acceleration amplitudes, to implement the droplet tracking process. Two capillary tubes with aspect ratios of 4.5 and 9.0, respectively, were used. The aspect ratio here was defined as the ratio of the maximum inner radius r_{max} to the minimum inner radius r_{min} of the tube. All experimental parameters were input into the theoretical model for calculations, and comparisons were generated thereafter. More discussion of the rationale behind the development of the theoretical model can be found in the previous publication of W. Deng and Cardenas (2013) and will not be detailed in this paper.

Capillary tubes with an outer diameter of 2 mm and an inner diameter of 1.12 mm were pulled using a micropipette puller (Figure 2(a)) to form the sinusoidally-constricted tubes, as demonstrated in Figure 2(b). By controlling the pulling velocity and heating temperature of the micropipette puller, the wavelength and radius of the constricted section of the tube can be controlled, and thus, the desired aspect ratio r_{max}/r_{min} of the constricted tube can be achieved. By using the micropipette puller, r_{max} was kept constant at 1.12 mm in our experiments, but r_{min} varied to achieve different aspect ratios. The value of r_{min} was measured using camera imaging in the experiments. For the constricted tubes used in the experiments, $L_1 = -30$ mm, $L_2 = 30$ mm and $2L = 7.1$ mm.

We modified the wettability of the tube to be highly hydrophilic in order to make the experimental setup consistent with the theoretical model, which made an assumption of the hydrophilic wall. By having the highly hydrophilic wall, only sliding would occur at the three-phase (i.e., solid wall, wetting and non-wetting phases) contact points, and pinning would be prevented. The tube was first sanitized using the piranha solution (H_2SO_4 and H_2O_2) in an ultrasonic cleaner before pulling, and then silanized using trimethoxysilane after pulling. Finally, the tube was glued flat onto a glass microslide to avoid breaking apart during later shaking.

The LW13.141-75 electrodynamic shaker system from Labworks Inc. was connected to the mounting table, on which capillary tubes were steadily fixed as shown in Figure 2(c). The output frequencies of the shaker can be adjusted from 2 Hz to 500 Hz with a minimum interval of 0.2 Hz, and the acceleration amplitudes can be adjusted from 0.1 g (1 g $\approx$ 9.8 m/s^2) to 10 g with a minimum interval of 0.1 g. A high-speed camera, the Phantom Miro M110 with Canon EF 100mm f/2.8L IS USM Macro lens, was mounted

vertically just above the middle section of the tube to ensure the scope of the observation and diminish error due to skewed angles. We used the highest resolution of 1280×8 00 at a recording speed of 400 fps to acquire the best quality of images possible to implement the dynamic point-tracking process. Before tracking, the videos were calibrated by providing the software with a reference length. We picked two points on the upper and lower outer tube and then set the distance of these two points to 2 mm, which is the outer diameter of the tube. Therefore, the frames in their entirety were accurately calibrated to 5.52μm/pixel for oscillation videos that have a longer focal length when recorded, and 19.4μm/pixel for mobilization videos that have a shorter focal length. Instead of using auto-tracking, we used manual tracking for better post processing of the data. As shown in Figure 2(e), two points were manually tracked: one (yellow) was the point selected on the reference marker attached to the tube, and the other (blue) was the very front point of the downstream meniscus of the droplet. In the experiments, the tracks did not run in perfect straight lines due to a slightly rotational motion of the shaker. However, the maximum deviation of this non-perfect straight motion normal to the vibration direction was as small as 10 μm at a frequency of 10 Hz, which is equivalent to a 0.04 m/s^2 acceleration normal to the vibration direction. We estimated that such a small normal acceleration should not significantly affect our experimental results.

Deionized water with a viscosity of 1 cP was used as the wetting fluid to rinse the tube for several rounds and then fill up the tube. The non-wetting fluids used in the experiments included hexane (0.297 cP, 0.655 g/cm^3), decane (0.92 cP, 0.73 g/cm^3), and dodecane (1.36 cP, 0.75 g/cm^3), respectively. The interfacial tension, measured at room temperature, was 0.052 N/m between water and hexane, 0.054 N/m between water and

decane, and 0.054 N/m between water and dodecane is. Tubing with an outer diameter of 0.385 mm, much thinner than the capillary tube, was used to deliver the non-wetting fluid slowly and controllably to the upstream part of the throat of the tube. It was possible to adjust the volume of the non-wetting droplet by altering the speed at which the syringe was pushed. The ideal non-wetting droplet would be not too small or too large. Too small of a size would make it quite difficult to capture the full motion of the upstream front meniscus with the small inertial force exerted on the droplet. Too large of a size would initiate a snap-off phenomenon when the droplet was shaken while trying to pass through the constricted section, which could seriously affect the experimental results. A discussion of the snap-off mechanism, which is beyond the scope of this paper, can be found in Wen Deng, Cardenas, and Bennett (2014) and Wen Deng, Balhoff, and Bayani Cardenas (2015). The criteria for the droplet size included that the downstream meniscus was not to touch the inlet of the tube when the droplet was oscillating, and the droplet was not to snap off when passing through the throat; otherwise, the droplet was to be as long as possible. The volume of the droplet was calculated by first digitizing its periphery and then integrating these digitized points axisymmetrically.

One example of a non-wetting droplet being trapped upstream of the constricted section at its initial balanced condition is shown in Figure 2(d). The non-wetting phase was dyed by Oil Blue N to distinguish it from the wetting phase. The contact angle of this tube was approximately $\theta = 15°$, which was in the best range, from 10°-20°, that we were able to obtain experimentally for the contact angle. A schematic of the whole experimental setup is demonstrated in Figure 2(c). The initial condition of droplet trapping was obtained by adjusting the height of the cylindrical water tank. The height difference between the

water level in the tank and the outlet of the tube provided a constant external pressure difference within the capillary tube. For the trapped droplet, this pressure difference was balanced by the capillary pressure difference at the downstream and upstream menisci in the constricted tube.

For each experiment, we first entrapped the droplet at the upstream of the throat by carefully controlling the external pressure difference. The downstream meniscus of the droplet was ideally not too close to or far away from the throat. Depending on the initial volume of the droplet being introduced into the capillary tube, the external pressure difference could be different for each experiment.

After the entrapment of the droplet, we applied a vibration with a fixed frequency in the direction parallel to the tube. We initially set a very small acceleration amplitude at which the droplet would oscillate but not be mobilized.

In the oscillation experiments, after several tens of periods of vibration for approximately 5-10 seconds, we stopped the vibration, and the video was saved as a cine file that can be played frame by frame for post processing. Before increasing the acceleration amplitudes beyond the critical amplitudes for mobilization, lower acceleration amplitudes were used first to validate the theoretical model by comparing the absolute displacement of both the droplet and the wall under different frequencies of experimental data. By using the absolute displacement of the droplet and tube wall under different frequencies in a forced oscillation system, an amplitude amplification determined by referencing Tongue (2002) was used to quantify the amplifying effect of the oscillating system.

The amplitude amplification was defined as the ratio of the amplitude of output displacement to input acceleration as:

$$R_a = \frac{X_{output}}{A_{input}} = \frac{X_{output}}{X_{input}(2\pi f)^2} \quad (7)$$

where X_{output} refers to the displacement amplitude of the droplet, X_{intput} refers to the displacement amplitude of the tube wall, and A_{input} and f are the acceleration amplitudes and frequencies, respectively, applied to the capillary tube. The correlation between the amplitude amplification and the frequency of the vibration can be used to depict the damping effect in the oscillating system of the droplet in the constricted tube. When the amplitude amplification decreases monotonically as the frequency of the vibration increases, this indicates that the fluid oscillating system is in an overdamped regime; when there is a nonzero peak of the amplitude amplification as the frequency of the vibration increases, this means the fluid oscillating system is in an underdamped regime. However, it is very time consuming to determine whether the flow is overdamped or underdamped because a large number of frequencies must be tested.

In the mobilization experiments, we first set the minimum acceleration amplitude of the seismic stimulation to oscillate the droplet. With no mobilization after ten periods of vibration or even more, we gradually increased the acceleration amplitude of the vibration until the non-wetting droplet was mobilized. We then observed that the equilibrium position of the oscillating droplet shifted gradually towards the throat. With this information, we then were able to predict, before any mobilization, the next amplitude acceleration that would induce mobilization, and get the camera ready to record.

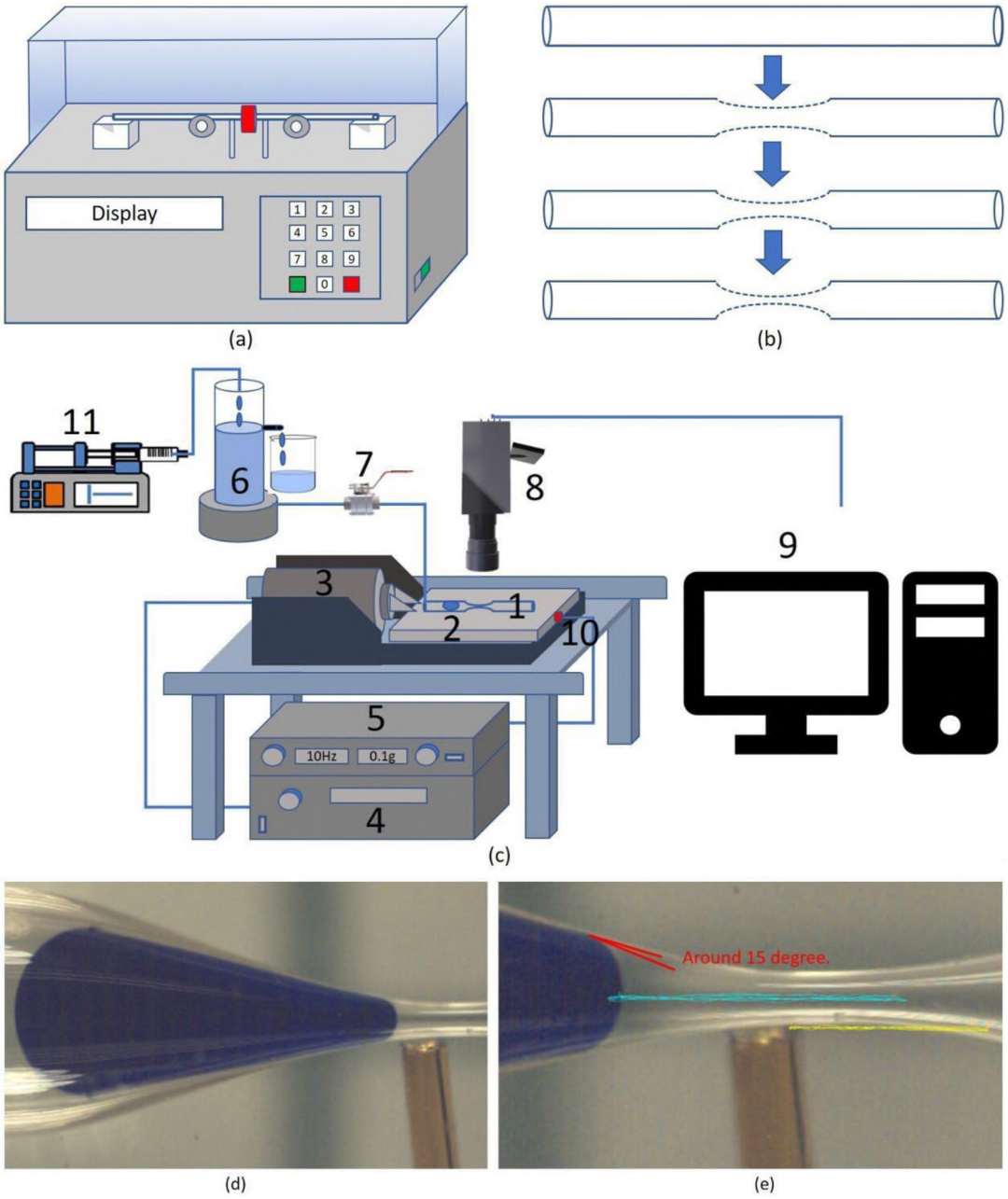

Figure 2. (a) Micropipette puller; (b) capillary tubes with different radii of constricted section; (c) schematic of vibration experimental workflow: 1. constricted capillary tube; 2. non-wetting droplet; 3. shaker; 4. power amplifier; 5. sine controller; 6. water tank; 7. control valve; 8. high-speed camera; 9. imaging system; 10. acceleration sensor; 11. syringe pump; (d) balanced position of non-wetting droplet; (e) motion tracks of non-wetting droplet by manual tracking (blue: front meniscus point; yellow: glass tube wall reference point)

Due to a limitation of the shaker system, the acceleration amplitude of the vibration could only be adjusted at a minimum interval of 0.1 g. That was the major uncertainty of the experiments to determine the critical acceleration amplitude for droplet mobilization. The acceleration amplitude could be over-adjusted by having the minimum adjustment interval as large as 0.1 g to achieve droplet mobilization in the constricted tube. Therefore, the error of the critical acceleration amplitude for mobilization could be systematically up to 0.1 g. The 0.1 g error between the experiment and the theoretical model represents the best agreement we could obtain experimentally for the critical acceleration amplitude due to the limitation of the shaker system.

Calculating the critical acceleration amplitude of the theoretical model required some parameter inputs from the experimental setup. The experimental parameters used as theoretical inputs included the following: the viscosity of the fluids, the contact angle for the wall, the geometry of the tube, the initial position of the upstream and downstream menisci, and the external pressure difference. However, due to limitations of the experiments, we could not measure the external pressure difference precisely. By knowing the initial position of the upstream and downstream menisci and the tube geometry, we were able to calculate the capillary pressure difference for the entrapment of the droplet. When a droplet is statically trapped, the external pressure difference should be equal to the capillary pressure difference. Therefore, based on this force balance, we calculated the external pressure difference and used this calculated value as input for the theoretical calculation.

When we measured the initial positions of the upstream and downstream menisci, the maximum allowed measurement error was approximately ± 0.1 mm. By considering

this measurement error in the experiments, the induced error in calculating the critical acceleration amplitude was approximately ± 0.2 m/s^2. Sometimes the experiments needed to be re-conducted if we found significant differences between the experimental and theoretical results after identifying and correcting the mistakes of the operation and experimental setup in most cases.

In the mobilization experiments, we also observed that the chemical coating used to modify the wettability of the tube wall could degrade with time and the number of experiments conducted, which could cause the contact angle to increase. Due to this alteration, a change of the contact angle from 20° to 60° can result in approximately a 0.2-1.3 m/s^2 error in the prediction of the critical acceleration amplitude. In the heoretical model, we assumed a sinusoidal profile of the tube. However, the tube cannot be a perfectly sinusoidal shape after being pulled by the micropipette puller. We estimated the error caused by the tube's geometry as being no greater than 0.1 m/s^2.

After recording the displacement of the droplet and glass tube, we picked approximately 4 periods of vibration for post processing to generate a motion graph. The data points on the graph were saved with a plot of displacement versus time and further compared with theoretical calculations.

3. RESULTS AND DISCUSSIONS

3.1. OSCILLATION

By using three non-wetting fluids with different viscosities and aspect ratios of the tube, we compared the amplitude amplification of the experimental data with the

theoretical results at the following frequency and acceleration amplitude combinations: 10 Hz, 0.2 g; 20 Hz, 0.4 g; 30 Hz, 0.6 g; 40 Hz, 0.8 g; 50 Hz, 1.0 g. All fluid types and aspect ratios shared the same acceleration amplitudes with corresponding frequencies. Figure 3 shows that the amplitude amplification decreased monotonically as the frequency increased for both aspect ratios. However, we could only measure the amplitude amplification at discrete frequencies in the experiments, instead of along a continuous frequency spectrum. Therefore, based on the experimental data alone, we cannot judge whether the flow was overdamped or underdamped. This demonstrates the advantage of having a reliable theoretical model for this study, as the amplitude amplification can be calculated along a continuous frequency spectrum. With the supplement of the theoretical model, we can observe that the R_a monotonically decreased with the increase of frequency. Therefore, we can further judge that the flow was overdamped at the current experimental parameters, and no resonance was expected to occur in oscillation experiments with small acceleration amplitudes.

Considering the constricted tubes used in our experiments, a syringe-injected droplet was able to be mobilized easily in the d tube with a gentle slope (i.e., small aspect ratio) during the adjustment of the external pressure difference for droplet entrapment. Due to the difficulty of entrapping the droplet in the tube with the small aspect ratio, we chose to entrap the droplet relatively far from the throat to prevent mobilization. The constricted shape of the tube made the oscillation while applying the vibration less significant when the downstream meniscus of the droplet was relatively far from the throat. Therefore, the error for measuring the output displacement for the small aspect ratio was larger than that for the large aspect ratio.

Consequently, compared to the large aspect ratio, the small aspect ratio had larger error in the comparison of the experimental data with the theoretical results.

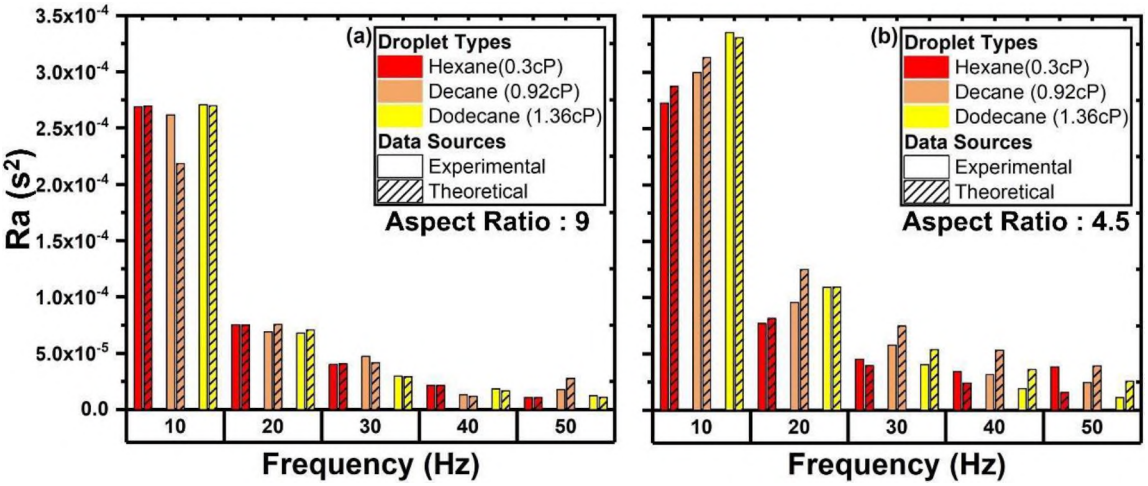

Figure 3. Amplitude amplification comparisons between experimental and theoretical results for three non-wetting droplets under different frequencies in: (a) 9 aspect ratio tube; (b) 4.5 aspect ratio tube

Theoretical displacements of the downstream meniscus and the wall were calculated and matched with the oscillation phase of the experimental data. In the comparison, the absolute displacements of the hexane droplet and tube wall were almost identical to the theoretical results. The only errors were at the wave crests and troughs of the displacement curves. The theoretical model can achieve continuous calculated results, so the curve of the theoretical results was much smoother and more regular than that of the experimental data, which was fitted by discrete data points. We attributed these errors at the wave crests and troughs in the comparison to the density of the sampling points we obtained through the experimental approach. The good agreement of the absolute displacement between the theoretical calculation and the experimental data in the time

domain can also indicate good agreement in the frequency domain. The experimental data show that the simple harmonic stimulation created by the shaker resulted in a simple harmonic oscillation of both the wall and droplet without higher modes of vibration. The experimental observation was also consistent with the theoretical calculation in the modes of vibration.

3.2. MOBILIZATION

Figure 5 shows the comparison between our experiments and the theoretical model in terms of the critical acceleration amplitude at different frequencies. For smaller aspect ratios, the droplet would tend to be mobilized more easily, as we discussed in the oscillation study. If the droplet was placed closer to the throat initially, it would be more difficult to control the external pressure difference to entrap the droplet. Therefore, in the tube with the aspect ratio of 4.5, we chose to entrap the droplet with the downstream meniscus relatively far from the throat, which resulted in that tube requiring a larger acceleration amplitude compared to the tube with the aspect ratio of 9, as shown in Figure 5.

In Figure 5, the trend of the critical acceleration amplitudes changing with the frequency differed from previous studies in which the critical acceleration amplitudes monotonically increased with the frequency (Beresnev and Deng, 2010; Deng and Cardenas, 2013) without considering the resonant effect. This difference can be attributed partially to the initial positions of the upstream and downstream menisci being different for each experiment (see Table 1). Taking as an example the case of the hexane droplet with the aspect ratio of 9, a peak point of critical amplitude exists at 40 Hz.

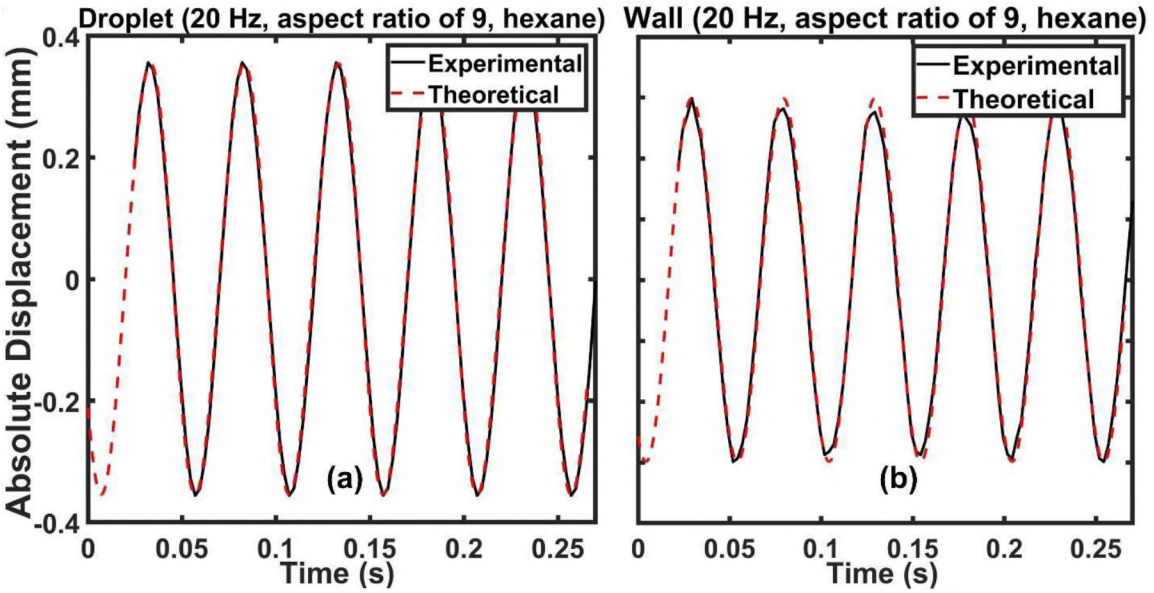

Figure 4. Droplet and tube wall absolute displacement comparisons between experimental and theoretical results for hexane at aspect ratio of 9

In this case, the droplet was entrapped much further upstream (shifted approximately 1 mm further upstream) than other cases at different frequencies, as shown in Table 1. The more upstream trapping for the case at 40 Hz indicates a much smaller background pressure drop, thereby requiring a larger acceleration amplitude to mobilize the droplet. The non- monotonic, frequency-critical amplitude relationship also can be attributed to the resonance in our mobilization experiments. According to our theoretical analysis in the oscillation study, the flow was overdamped, and no resonance occurred. However, the resonance analysis was based on the small A_{input} analysis. Referencing Equation (3), the droplet oscillation system is highly nonlinear, and R_a also depends on A_{input}. Therefore, resonance analysis based on a large A_{input} could be different. Supplementing this with information gained from the theoretical model reveals that the flow was underdamped at a large A_{input}, and resonance could be expected. We further

conducted the theoretical analysis of the critical acceleration amplitude by fixing the initial position of the droplet, as shown in Figure. 5(c) and 5(d). The initial positions of the front and back menisci were fixed at 0.7 and 4.7 mm upstream from the throat, respectively. It was observed that the critical acceleration amplitudes did not monotonically increase with the frequency, but had a lower limit. This lower limit region was consistent with the resonance frequency region as predicted.

During the mobilization experiments, the droplet snapped off after mobilizing and therefore could not be used for the next test. Instead, we had to clean the tube and introduce a new droplet for the new experiment. Due to the difficulty of experimentally controlling the initial entrapment of droplets, we could hardly maintain each droplet in the same initial position for different frequency experiments. Given the large number of experiments, at each frequency, we simply recorded one critical acceleration amplitude of mobilization and the mobilization process using a high-speed camera. Nevertheless, by comparing the experimental data with the theoretical calculations in Figure 5, the reliability of the experimental data can be justified.

In the tube with the aspect ratio of 9, the critical acceleration amplitude generally increased as the frequency increased, except when at a frequency of 50 Hz, while it remained more even in the tube with the 4.5 aspect ratio. However, as the frequency gradually increased, larger and larger acceleration amplitudes were required to mobilize the droplet when the droplet was initially entrapped far from the throat. To avoid using too large of an acceleration amplitude that would induce unstable vibrations of the shaker as the power magnified, we chose to entrap the droplet initially as close to the throat as

possible, and thus a smaller critical acceleration amplitude was required to mobilize the droplet even though the frequency was high.

Droplets of more viscous non-wetting fluids, such as decane and dodecane, generally were more difficult to mobilize in the tube compared to less viscous fluids, such as hexane, as shown by the comparison in Figure 5(a) and (b), respectively. This trend of the viscous effect was consistent with the prediction of the theoretical model.

For the experiments of different non-wetting phases, the initial droplet positions, aspect ratios and frequencies are given in Table 1. The initial positions were varied under various frequencies and viscosities for tubes with two different aspect ratios, which resulted in the need for different critical amplitudes. Generally, as the distance from the front meniscus to the pore throat increased, the critical acceleration amplitude increased, as shown in Figure 6 (a) and (b).

Figure 6 also depicts that the critical acceleration amplitude generally increased as the viscosity of the non-wetting fluid increased. However, the effect of the viscosity, as well as of the frequency, on the critical acceleration is not as significant as the effect of the distance from the front meniscus to the throat. According to the Young-Laplace equation, a larger distance from the meniscus to the throat indicates a smaller external pressure drop for the initial entrapment of the droplet. Therefore, the required critical acceleration amplitude should be greater.

In the comparison shown in Figure 6(b), some inconsistency between the critical amplitude and the distance appears at several points. This is because when the position of the front meniscus exceeded 3.5 mm, the entire droplet initially resided in the straight

portion of the tube, as demonstrated in Figure 1. Therefore, according to the Young-Laplace law, the external pressure drop was zero.

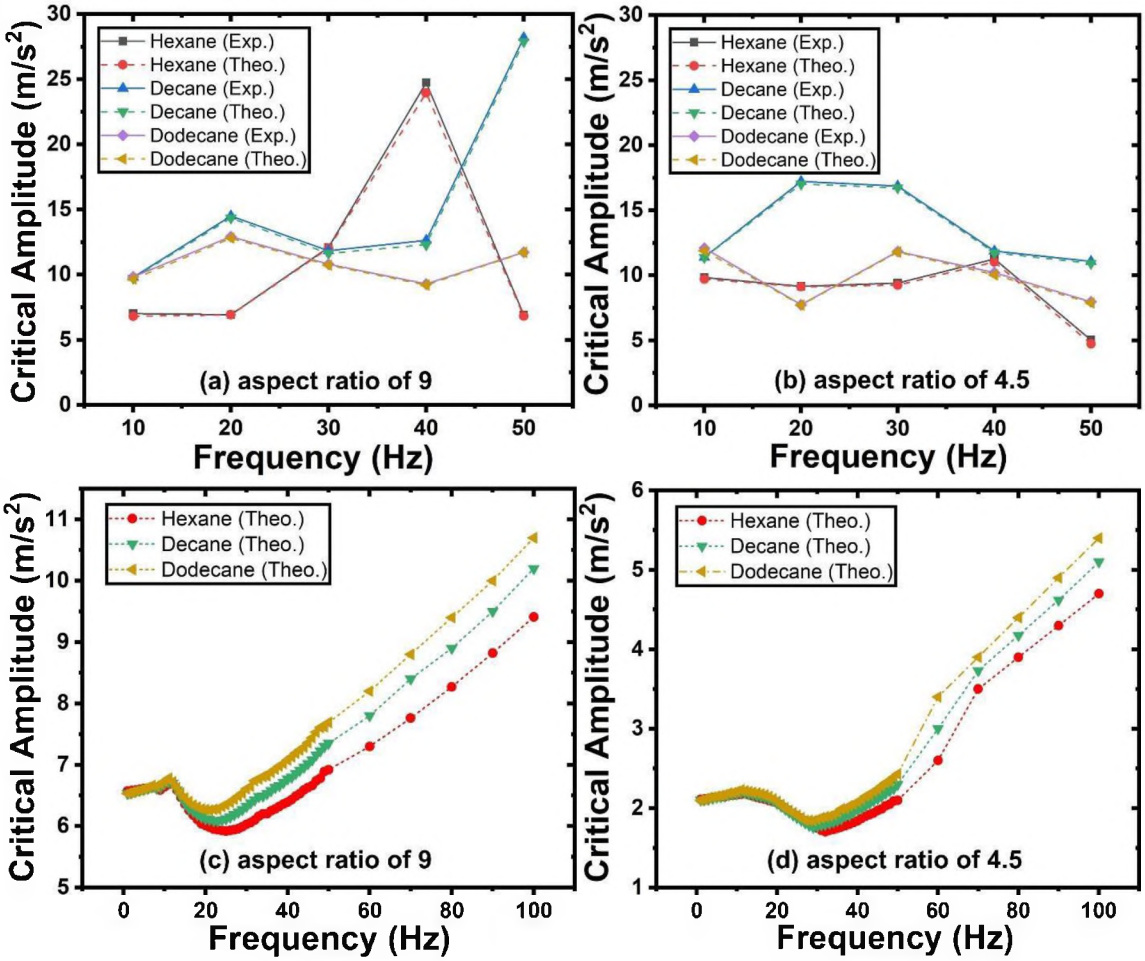

Figure 5. Critical mobilization acceleration amplitude comparison between experimental and theoretical results: (a) aspect ratio of 9, and (b) aspect ratio of 4.5, and theoretical analysis of dependence of critical mobilization acceleration amplitude on frequency: (c) aspect ratio of 9, and (d) aspect ratio of 4.5

Once we applied the seismic stimulation, the longer length of the initial droplet resulted in a larger critical acceleration amplitude. This effect of the position of the front meniscus on the critical amplitude was further investigated through the theoretical analysis,

as shown in Figure 6(c) and (d). In the theoretical analysis, we used the position of front meniscus as given in Table1 but fixed the volume of the droplet by varying the position of back meniscus to exclude the volume effect.

Table 1. Initial positions of the non-wetting droplet

Aspect Ratio (9)									
	Hexane (0.3cP)			Decane (0.92cP)			Dodecane (1.36cP)		
	Distance to throat/mm		Volume size/mm^3	Distance to throat/mm		Volume size/mm^3	Distance to throat/mm		Volume size/mm^3
Frequency /Hz	Front	Back		Front	Back		Front	Back	
10	0.7	4.7	11.3	1.2	5.0	12.4	1.1	5.3	13.6
20	0.8	4.8	11.7	2.0	5.9	15.2	1.8	6.1	16.3
30	1.6	5.6	14.5	1.4	5.3	13.4	1.1	5.3	13.6
40	2.0	6.2	16.4	1.4	5.3	13.4	0.9	5.1	12.8
50	0.7	4.9	12.1	2.0	5.9	15.2	1.1	5.3	13.6
Aspect Ratio (4.5)									
	Hexane (0.3cP)			Decane (0.92cP)			Dodecane (1.36cP)		
	Distance to throat/mm		Volume size/mm^3	Distance to throat/mm		Volume size/mm^3	Distance to throat/mm		Volume size/mm^3
Frequency /Hz	Front	Back		Front	Back		Front	Back	
10	6.6	9.8	13.8	7.0	10.2	14.8	7.2	9.9	12.8
20	3.8	7.1	14.2	6.0	9.2	14.8	3.4	6.1	12.7
30	3.0	6.2	13.5	4.2	7.3	14.4	3.6	6.3	12.8
40	2.8	6.0	13.3	2.9	6.0	13.8	2.6	5.3	11.8
50	1.3	4.5	10.2	2.4	5.5	13.0	2.0	4.7	10.5

In the theoretical analysis, the volume for the tube of aspect ratio 9.0 was 11.3 mm^3, and the volume for the tube of aspect 4.5 was 10.2 mm^3. The frequency and front

meniscus position can be referenced in Table 1. The observation from the theoretical analysis is consistent with the experimental observation: the position of the front meniscus generally has a more significant influence on the critical acceleration amplitudes than the viscosities and frequencies considered in the experiments.

We also compared the experimental absolute displacement of the droplet with the theoretical results in the mobilization scenario. However, due to having too many video files for mobilization to be analyzed point by point, we chose just one example as a comparison, the dodecane as the non-wetting phase to be mobilized at 10Hz in the tube with the aspect ratio of 9 (Figure 7). In the theoretical calculation, it only took about two periods of vibrations for the droplet to be mobilized, while in the experiment, mobilization took many more periods of vibration.

This discrepancy between the experiment and the theoretical model is similar to the comparison between the theoretical model and the CFD simulation in research by (W. Deng & Cardenas, 2013). It is mainly attributed to two simplifications we made in the theoretical model. The first is that a Poiseuille velocity profile was used to derive the theoretical model. When the flow is highly unsteady and the momentum changes rapidly, the velocity profile is relatively flat or plug-like in the central part of the cross section of the tube due to the inertial force term, and the corresponding flow rate should be smaller than that of the parabolic-like velocity profile of Poiseuille flow under the same pressure gradient. Therefore, a Poiseuille velocity profile could overestimate the flow rate under a high-frequency oscillation force. Further discussion about the effect of velocity profile on the theoretical analysis of the droplet mobilization can be found in Zeng, Deng, Fan, and Zhang (2019).

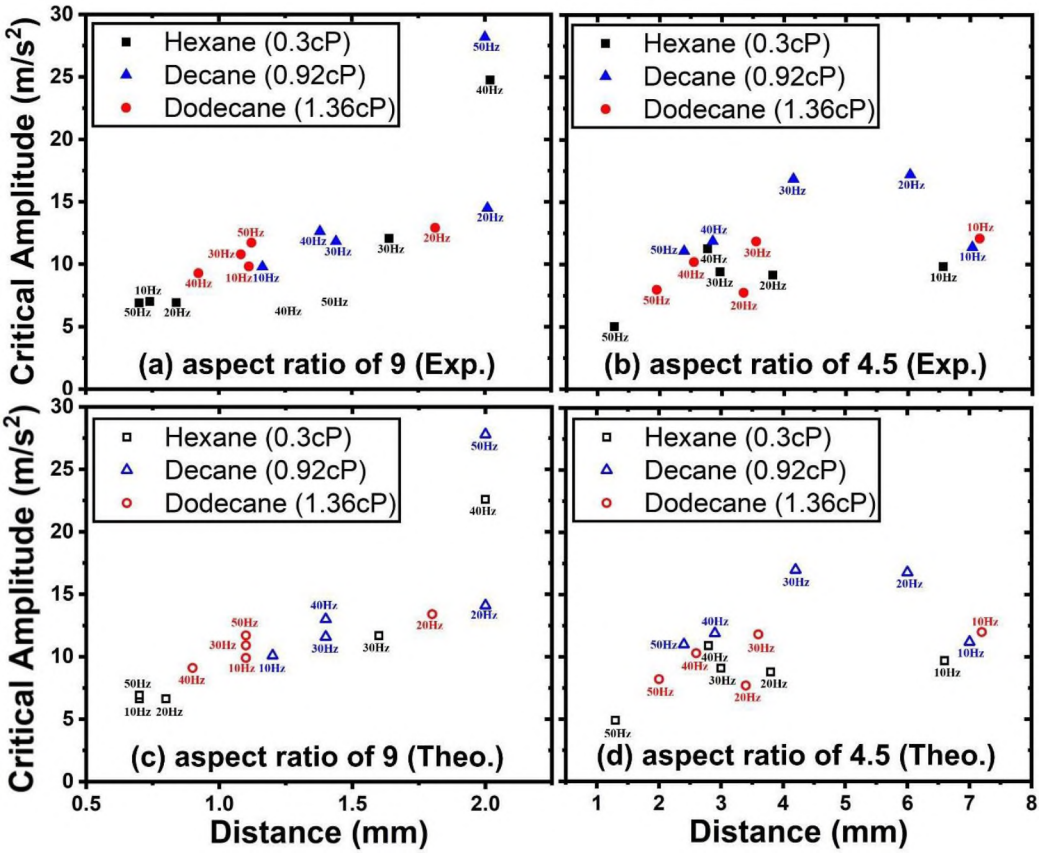

Figure 6. Experimental measurement of the critical amplitudes at different initial distances from front meniscus to throat at aspect ratios of (a) 9 and (b) 4.5, and theoretical analysis of the critical amplitudes at different initial distances from front meniscus to throat at aspect ratios of (c) 9 and (d) 4.5

The second simplification is that the dynamic contact angle of the menisci was neglected; a dynamic contact angle could cause flow resistance if the momentum of the flow were to change rapidly. Both of these simplifications could cause overestimation of the flow in the theoretical model. When the equilibrium position of the oscillation of the droplet shifts gradually, the errors caused by overestimation are superposed. This is why the discrepancy between the experimental and theoretical results of the temporal displacement is more significant in the mobilization process than in the oscillation process.

Moreover, this overestimation and error superposition are more significant with higher excitation frequencies.

4. SUMMARY AND CONCLUSION

Silanized-constricted tubes with high hydrophilicity were made to analyze the dynamic behavior of two immiscible fluids stimulated by a shaker. Three non-wetting fluids with different viscosities were used for the analysis. The motion of downstream meniscus and tube wall were tracked manually using a high-speed camera. The experimental amplitude amplification and absolute displacements in the oscillation experiments, as well as the critical acceleration amplitudes and absolute displacements in the mobilization experiments, were compared with the theoretical results.

The experimental observation shows that a simple harmonic seismic stimulation can only cause a simple harmonic droplet oscillation response without higher modes of vibration in an overdamped condition. The oscillation experiments show that the amplitude amplification decreases monotonically with the frequency, and the effect of viscosity in the range we considered on the amplitude amplification-frequency relationship is not significant when the flow is in an overdamped condition. The mobilization experiments show that the critical acceleration amplitude could be affected by both the resonance of the droplet and the initial trapping position of the front meniscus. Droplet resonance not occurring at a small input acceleration amplitude could occur at a large input acceleration amplitude due to the nonlinearity of the droplet oscillation system. When resonance occurs, it can help reduce the required critical acceleration amplitude to mobilize the droplet.

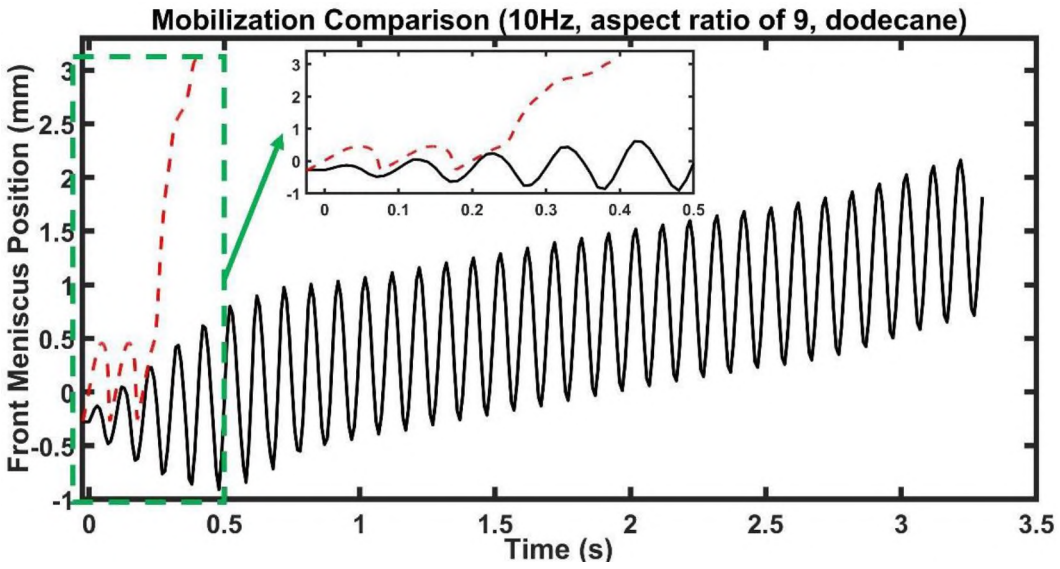

Figure 7. Absolute displacement comparison between experimental and theoretical result for dodecane at 10Hz. The dashed red line was calculated by the theoretical model, and the solid black line represents the experimental measurement

The effect of initial trapping position of the front meniscus can be comparable to or even greater than the effect of the frequency on the critical acceleration amplitude. In the experiment, droplet mobilization could be achieved after multiple periods of vibration instead of occurring suddenly.

Based on the comparisons of the experimental and theoretical results, we concluded that the theoretical model was reliable for predicting the dynamics of the non- wetting droplet in response to seismic stimulation in the experiments with different combinations of critical experimental parameters considered in this study. The minor discrepancy between the experimental and theoretical results can be explained by the known limitations of the theoretical model.

REFERENCES

Alhomadhi, E., Amro, M., & Almobarky, M. (2014). Experimental application of ultrasound waves to improved oil recovery during waterflooding. *Journal of King Saud University-Engineering Sciences, 26*(1), 103-110.

Ali, M. Y., Berteussen, K. A., Small, J., & Barkat, B. (2010). Low-frequency passive seismic experiments in Abu Dhabi, United Arab Emirates: implications for hydrocarbon detection. *Geophysical Prospecting, 58*(5), 875-899.

Beresnev, I., Gaul, W., & Vigil, R. D. (2011). Direct pore-level observation of permeability increase in two-phase flow by shaking. *Geophysical Research Letters, 38*(20).

Beresnev, I. A. (2006). Theory of vibratory mobilization on nonwetting fluids entrapped in pore constrictions. *Geophysics, 71*(6), N47-N56. doi:10.1190/1.2353803

Beresnev, I. A., & Deng, W. (2010). Viscosity effects in vibratory mobilization of residual oil. *Geophysics, 75*(4), N79-N85. doi:Doi 10.1190/1.3429999

Beresnev, I. A., & Johnson, P. A. (1994). Elastic-wave stimulation of oil production: A review of methods and results. *Geophysics, 59*(6), 1000-1017.

Beresnev, I. A., Vigil, R. D., Li, W., Pennington, W. D., Turpening, R. M., Iassonov, P. P., & Ewing, R. P. (2005). Elastic waves push organic fluids from reservoir rock. *Geophysical Research Letters, 32*(13).

Chrysikopoulos, C. V., & Vogler, E. T. (2006). Acoustically enhanced ganglia dissolution and mobilization in a monolayer of glass beads. *Transport in Porous Media, 64*(1), 103-121.

Deng, W., Balhoff, M., & Bayani Cardenas, M. (2015). Influence of dynamic factors on non-wetting fluid snap-off in pores. *Water Resources Research*, Accepted Author Manuscript. doi:10.1002/2015WR017261

Deng, W., & Cardenas, M. B. (2013). Dynamics and dislodgment from pore constrictions of a trapped nonwetting droplet stimulated by seismic waves. *Water Resources Research, 49*(7), 4206-4218.

Deng, W., Cardenas, M. B., & Bennett, P. C. (2014). Extended Roof snap-off for a continuous nonwetting fluid and an example case for supercritical CO2. *Advances in Water Resources, 64*, 34-46. doi:10.1016/j.advwatres.2013.12.001

Dobronrarov, O. (2002). Industry feature: A new technology of reservoir stimulation through exposure to weak seismic waves. *First Break, 20*(6), 379-382.

Elkhoury, J. E., Brodsky, E. E., & Agnew, D. C. (2006). Seismic waves increase permeability. *Nature, 441*(7097), 1135-1138.

Elkhoury, J. E., Niemeijer, A., Brodsky, E. E., & Marone, C. (2011). Laboratory observations of permeability enhancement by fluid pressure oscillation of in situ fractured rock. *Journal of Geophysical Research-Solid Earth, 116*, B02311.

Farajzadeh, R., Andrianov, A., Krastev, R., Hirasaki, G., & Rossen, W. R. (2012). Foam–oil interaction in porous media: implications for foam assisted enhanced oil recovery. *Advances in colloid and interface science, 183*, 1-13.

Geballe, Z., Wang, C. Y., & Manga, M. (2011). A permeability-change model for water-level changes triggered by teleseismic waves. *Geofluids, 11*(3), 302-308.

Graham, D., & Higdon, J. (2000). Oscillatory flow of droplets in capillary tubes. Part 2. Constricted tubes. *Journal of Fluid Mechanics, 425*, 55-77.

Hilpert, M. (2007). Capillarity-induced resonance of blobs in porous media: Analytical solutions, Lattice–Boltzmann modeling, and blob mobilization. *Journal of colloid and interface science, 309*(2), 493-504.

Hilpert, M., Jirka, G. H., & Plate, E. J. (2000). Capillarity-induced resonance of oil blobs in capillary tubes and porous media. *Geophysics, 65*(3), 874-883.

Hsu, S.-Y., Katz, J., & Hilpert, M. (2012). Theoretical and experimental study of resonance of blobs in porous media. *Geophysics, 77*(5), EN61-EN71. doi:10.1190/geo2012-0043.1

Iassonov, P. P., & Beresnev, I. A. (2003). A model for enhanced fluid percolation in porous media by application of low - frequency elastic waves. *Journal of Geophysical Research: Solid Earth, 108*(B3).

Jeong, C., Kallivokas, L. F., Kucukcoban, S., Deng, W., & Fathi, A. (2015). Maximization of wave motion within a hydrocarbon reservoir for wave-based enhanced oil recovery. *Journal of Petroleum Science and Engineering, 129*, 205-220. doi:http://dx.doi.org/10.1016/j.petrol.2015.03.009

Ju, B., Fan, T., & Ma, M. (2006). Enhanced oil recovery by flooding with hydrophilic nanoparticles. *China Particuology, 4*(01), 41-46.

Kurzeja, P. S., & Steeb, H. (2014). Variational formulation of oscillating fluid clusters and oscillator-like classification. I. Theory. *Physics of Fluids, 26*(4), 042106.

Lambert, M.-A., Schmalholz, S. M., Saenger, E. H., & Steiner, B. (2009). Low-frequency microtremor anomalies at an oil and gas field in Voitsdorf, Austria. *Geophysical Prospecting, 57*(3), 393-411.

Li, W., Vigil, R. D., Beresnev, I. A., Iassonov, P., & Ewing, R. (2005). Vibration-induced mobilization of trapped oil ganglia in porous media: Experimental validation of a capillary-physics mechanism. *Journal of colloid and interface science, 289*(1), 193-199.

Lo, W.-C., Yeh, C.-L., & Lee, J.-W. (2015). Effect of viscous cross coupling between two immiscible fluids on elastic wave propagation and attenuation in unsaturated porous media. *Advances in Water Resources, 83*, 207-222.

Manga, M., Beresnev, I., Brodsky, E. E., Elkhoury, J. E., Elsworth, D., Ingebritsen, S. E., . . . Wang, C. Y. (2012). Changes in permeability caused by transient stresses: Field observations, experiments, and mechanisms. *Reviews of Geophysics, 50*(2).

Mullakaev, M., Abramov, V., & Abramova, A. (2015). Development of ultrasonic equipment and technology for well stimulation and enhanced oil recovery. *Journal of Petroleum Science and Engineering, 125*, 201-208.

Müller, T. M., Gurevich, B., & Lebedev, M. (2010). Seismic wave attenuation and dispersion resulting from wave-induced flow in porous rocks—A review. *Geophysics, 75*(5), 75A147-175A164.

Nikolaevskiy, V., Lopukhov, G., Yizhu, L., & Economides, M. (1996). Residual oil reservoir recovery with seismic vibrations. *SPE Production & Facilities, 11*(02), 89-94.

Pentland, C. H., El-Maghraby, R., Iglauer, S., & Blunt, M. J. (2011). Measurements of the capillary trapping of super - critical carbon dioxide in Berea sandstone. *Geophysical Research Letters, 38*(6).

Pride, S. R., Flekkøy, E. G., & Aursjø, O. (2008). Seismic stimulation for enhanced oil recovery. *Geophysics, 73*(5), O23-O35.

Roberts, P. M. (2005). Laboratory observations of altered porous fluid flow behavior in Berea sandstone induced by low-frequency dynamic stress stimulation. *Acoustical Physics, 51*, 160-168.

Roberts, P. M., Esipov, I. B., & Majer, E. L. (2003). Elastic wave stimulation of oil reservoirs: Promising EOR technology? *The Leading Edge, 5*, 448-453.

Roberts, P. M., Sharma, A., Uddameri, V., Monagle, M., Dale, D. E., & Steck, L. K. (2001). Enhanced DNAPL transport in a sand core during dynamic stress stimulation. *Environmental Engineering Science, 18*(2), 67-79.

Saenger, E. H., Schmalholz, S. M., Lambert, M.-A., Nguyen, T. T., Torres, A., Metzger, S., . . . Méndez-Hernández, E. (2009). A passive seismic survey over a gas field: Analysis of low-frequency anomalies. *Geophysics, 74*(2), O29-O40.

Sheng, J. J., Leonhardt, B., & Azri, N. (2015). Status of polymer-flooding technology. *Journal of Canadian Petroleum Technology, 54*(02), 116-126.

Tongue, B. H. (2002). *Principles of vibration* (Vol. 2): Oxford University Press New York.

Wang, C. Y., & Manga, M. (2010). Hydrologic responses to earthquakes and a general metric. *Geofluids, 10*(1-2), 206-216.

Wang, Z., & Yin, C. (2017). State-of-the-art on ultrasonic oil production technique for EOR in China. *Ultrasonics sonochemistry, 38*, 553-559.

Zeng, C., Deng, W., Fan, J., & Zhang, Y. (2019). Effect of flow profiles on the flow subjected to oscillation forcing: an example of droplet mobilization in constricted tubes. *Journal of Hydrology*, 124295.

II. FABRICATION AND VERIFICATION OF A GLASS-SILICON-GLASS MICRO-/NANOFLUIDIC MODEL FOR INVESTIGATING MULTIPHASE FLOW IN SHALE-LIKE UNCONVENTIONAL DUAL-POROSITY TIGHT POROUS MEDIA

ABSTRACT

Unconventional shale or tight oil/gas reservoirs that have micro-/nano sizes of the dual-scale matrix pore throats with micro-fractures may result in different fluid flow mechanisms compared with conventional oil/gas reservoirs. Microfluidic model, as a potential powerful tool, has been used for decades for investigating fluid flow at pore- scale in energy field. However, almost all microfluidic models were fabricated by using etching methods and rare ones were having dual-scale micro-/nanofluidic channels. Herein, we developed a lab-based, quick-processing and cost-effective fabrication method using lift-off process combined with anodic bonding method, which opts out of using any etching methods. A dual-porosity matrix/micro-fracture pattern, which can mimic the topology of the shale with random non-regularly grain shapes was designed by Voronoi algorithm. The pore channel width range is 3 μm to 10 μm for matrices and 100- 200 μm for micro-fractures. Silicon is used as the material to evaporate and deposit onto the glass wafer and then bonded with another glass wafer. The channel depth is the same 250 nm to the deposited silicon thickness. By using the advanced confocal laser scanning microscopy system (CLSM), we directly visualized the pore level flow within micro-/nano dual-scale channels with fluorescent-dyed water and oil phases. We found serious fingering phenomenon when water displacing oil in the conduits even the water has higher viscosity and the residual oil distributed as different forms in the matrices, micro-fractures and

conduits. We demonstrated that different matrix/micro-fracture/macro- fracture geometries would cause different flow patterns that affect the oil recovery consequently. Taking advantage of such a micro-/nano dual-scale 'shale-like' microfluidic model fabricated by a much simpler and lower-cost method, studies on complex fluid flow behavior within the shale or other tight heterogeneous porous media would be benefited significantly.

1. INTRODUCTION

Unconventional reservoirs, including shales and other types of tight formations, which intrinsically have much lower permeability than conventional reservoirs with micro-/nano scale dual-porosity features, can exhibit highly varying properties within microscopic confinement. Therefore, microfluidic model, as a powerful pore-scale level approach is needed to better understand the flow behavior and mechanism within the heterogeneous porous media of the shale-like tight oil/gas reservoirs. According to the average pore-throat diameter size of unconventional shale and other tight oil/gas reservoirs, the ratio of pore surface area to the pore volume which can be 50×10^{4} cm^{-1} (over 700 if represented by the ratio of channel width to depth in a microfluidic model), is much larger than that of conventional porous media which can be 1.8×10^{-4} cm^{-1} (nearly 0.01 if represented by the ratio of channel width to depth in a microfluidic model)(Boruah et al., 2019; Nelson, 2009). Hence, the hypothesized surface interfacial phenomena dominated fluid flow make the liquid and gas transportation through shale are still uncertain.(Civan et al., 2011) Although some of microfluidic devices possessing dual-scale matrix/fractures network features have been built by using different fabricating method (M Buchgraber et

al., 2012; Conn et al., 2014; K. Xu, Zhu, et al., 2017; Yun et al., 2017), the channels are all in micro scale for any dimensions and not having large width- to-depth ratio (2-26), which cannot representing fluid pathways of shale or tight duel- scale reservoirs. Until recently, though the first micro-/nano PDMS-glass and quartz- glass duel-scale microfluidic models come up to represent dual scale shale, (Kelly et al., 2016) the width-to-depth ratio (1-25) still stay small. Besides, the fabrication method cannot guarantee oil flow on PDMS-glass model and high-pressure experiments on glass-glass model due to the bonding issue.

Although PDMS micromodel now can realize sub-100 nm dimensions (Kelly et al., 2016; Peng & Li, 2016), it is still not a proper candidate for conducting experiments involving organic nonpolar fluids,(J. N. Lee et al., 2003) which is ubiquitous in many petroleum and environmental scenarios (Geng, Ding, et al., 2018; Geng, Pu, et al., 2018; Herrick et al., 2004; Weaver, 1984). Hence, nonorganic materials based silicon-glass or glass-glass microfluidic models have risen in response and widely been used to fabricate micro-/nanofluidic models capable of handling harsh physical and chemical conditions for energy fields (Alfi et al., 2016; Gunda et al., 2011; Lefortier et al., 2012; Lin et al., 2010; Parsa et al., 2015). For silicon-glass ones, since silicon has no transparency to visible light, a glass wafer is always being a transparent cover plate anodic bonded over the silicon substrate to make it possible for direct observation under a microscope (Grate et al., 2012; Q. Wu et al., 2014; Q. Wu et al., 2013).To achieve fully transparency and for the superiorities of compatibility with many solvents (Doryani et al., 2016; Ren et al., 2013), high stiffness for handling high pressure fluid flow experiments(Bora et al., 2000; Kazemifar et al., 2015; Sohrabi et al., 2001) and the easiness of surface wettability alteration by different methods (Grate et al., 2013; Maghzi et al., 2012), the glass itself has

long been a preferred microfluidic model substrate. The choice between the two is mainly depending on the goals and needs. Silicon substrate would be chosen when one needs more precise channel sizes and straight channel side walls when using dry etching method (Kawai et al., 2010). Although glass substrates can also be dry-etched,(Bu et al., 2004; Kutchoukov et al., 2004) the low etching rate, low etching selectivity and high facility cost make wet etching a more popular way, which make use of buffered hydrofluoric acid or mixtures of acids as the etchant solutions to etch channels on glass substrates. (Castano-Alvarez et al., 2008; Iliescu et al., 2008; Wan et al., 1996) The main drawback is that the isotropic wet etching process cannot reach perfect vertical walls,(Castano-Alvarez et al., 2008) yet this imperfect trapezoidal shape can be leveraged to generate a 2.5 D micromodel by controlling the etching depths of two neighboring pores.(K. Xu, Liang, et al., 2017) Other fabrications of semi or fully transparent microfluidic models for energy and other fields can be found elsewhere in details.(Anbari et al., 2018; X. Chen & Zhang, 2018; Iliescu et al., 2012; N. Karadimitriou & Hassanizadeh, 2012; Kovarik & Jacobson, 2009; Lifton, 2016)

Among all available fabrication methods, thin film deposition, as a fast, low cost and simple process, has been used to produce micro-/nanochannels in several applications.(Kanno, Ino, Shiku, & Matsue, 2015; Liang et al., 2016; Mao & Han, 2009) However, for energy field microfluidic system, it is rarely used and only as an auxiliary method to deposit a protection layer and hard mask for subsequent wet etching or dry etching process.(Bien, Rainey, Mitchell, & Gamble, 2003; Kelly et al., 2016; R. Müller, Schmid, Munding, Gronmaier, & Kohn, 2004) The aforementioned glass-quartz transparent micro-/nanofludic devices that emulates dual-scale properties of shale and

tight-oil reservoirs also utilized the thin film deposition to help make the model.(Kelly et al., 2016) They used thermal deposition to coat Cu film onto a lacey carbon support film and reactive ion etched the quartz substrate based on the mask. Finally, two glass wafers were bonded by continuously flushing demineralized water between the two wafers and combining them stand for more than 3 hours. (Jia, Fang, & Fang, 2004) However, the reactive ion etching method can produce etching byproducts that would clog the thinner channels and the 'sag' of the lacey carbon film is very likely occurred across larger apertures. Besides, it needs at least 3 to 4 days standing time for two plates bonded at least 80% strength, which is 61.8 ± 2.6 N/cm^2, to use for a fluid flow experiment. Although this bonding method can be realized at room temperature to avoid deformation of glasses at high temperature by using fusion bonding, the bonding strength and temperature resistance are questionable.

How to fabricate a 'shale-like' micro-/nanofluidic model that has a large width-to-depth ratio (12-2000) in a time-efficient and cost-effective way and meanwhile, keeping it fully transparent and strong bonding strength remains challengeable and needful these days. In this work, we, for the first time, deliver such a possibility by using the direct lift- off process combined with the anodic bonding process. For glass-based models, both wet etching and dry etching need to deposit a metal layer at first step and then do the etching at second step. The lift-off process and the etching process on a glass substrate both require the photolithography pattern and thin film deposition (Park, Lee, Lee, Park, & Park, 2005). Therefore, instead of using any etching methods downwards the substrate, we build the grains upwards and use them directly as the intermediate layer for anodic bonding. By skipping the etching process, one may save more than 5 hours a day for fabricating 20

samples (2 cm ×2 cm) excluding other preparation times for etching. This simple, time-saving and cost-effective method improves the efficiency of fabricating a micro-/nanofluidic model significantly. The detailed fabrication processes are presented in the following sections. Finally, the functionality and practicability of the micro-/nanofluidic model are demonstrated based on the multiphase fluid flow experimental results.

2. RESULTS AND DISCUSSION

2.1. DUAL-POROSITY PORE NETWORK DESIGN

To generate a complex heterogeneous porous media for investigating the multiphase flow with a microfluidic model, the Voronoi tessellation algorithm was utilized to mimic the real reservoir with random geometries and labyrinth-like pore networks.(M. Wu et al., 2012) The Voronoi diagram, also called Voronoi tessellation or Voronoi decomposition, is to use a computational geometry algorithm to partition a plane into different sizes of non-overlapping regions based on the closest distances among the randomly preset points on the plane(Okabe, Boots, Sugihara, & Chiu, 2009). However, simple Voronoi tessellation pattern with connected straight channels cannot represent the real 'convergent-divergent' conditions within the porous media and all the channels share the same width. Herein, we used the improved Voronoi tessellation algorithm in AutoCAD software to design a dual-porosity pattern with two matrices and micro- fractures connected with the matrixes with different channel widths. Further, the grains were designed as close as possible to granular shapes rather than polygonal shapes to represent the real rock grains in reservoirs, which make the pore networks have the 'convergent-divergent' profiles. As

shown in Figure 1, the porous media including two matrixes and micro-fractures is sandwiched between two flow conduits, which can be regarded as macro-fractures. The lengths of two flow conduits and the porous media are 1.3 cm and 0.8 cm and the widths are 0.05 cm and 0.2 cm. Connecting to the flow conduits that have side lengths 0.1 cm are the inlet and outlet for flow injection and recovery. The outer squares with 0.3 cm side length are the pre-saturation zone to decrease the probability of blocking when injecting and recovering the fluids. The intergranular channels within the matrixes are of narrowest ones from 3 μm to 10 μm and 100-200 μm for the micro-fractures. Several vugs were also yielded by eliminating amount of grains at left and right side of the porous media. The porous media, excluding the flow conduits, consists of 192 grains with a total porosity of 28%, which could be smaller if the vugs are not counted. The porosity for the two matrixes is approximately 5% and 23% for combined micro-fractures and vugs.

2.2. MICROMODEL FABRICATION

The micromodel was fabricated lab-based and the successive fabrication steps of the micromodel are presented in Figure 2(a-f). A glass substrate was first spin-coated with the S1813 positive photoresist and then the pattern was developed under UV exposure followed with MF321 developer. The substrate was then loaded into a vacuum chamber and coated with an amorphous silicon layer using e-beam evaporation at an average rate of 1.6 Å/s at temperatures 16 – 50 Celsius degree. Finally, lift-off process removed the photoresist in the channels using remover-PG (a proprietary solvent stripper designed for efficient and complete removal of photoresists). The glass substrate was anodic bonded with another glass wafer after two holes were punched as inlet and outlet using UV laser.

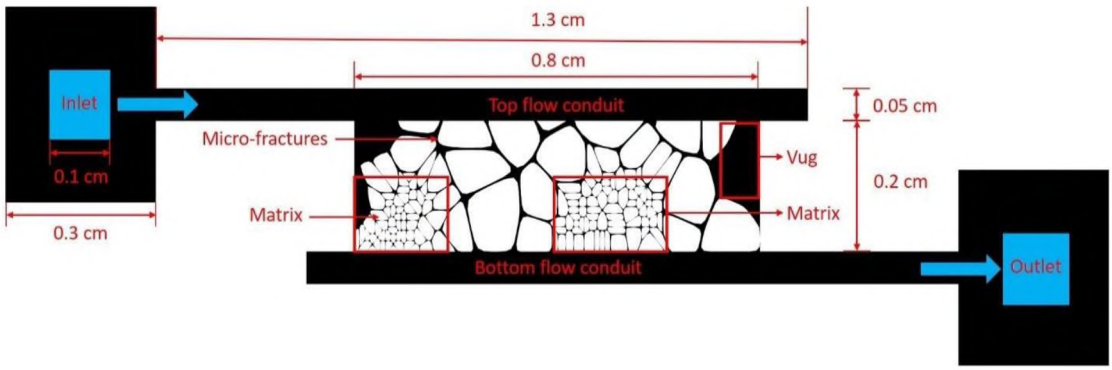

Figure 1. Dual-porosity pattern design using Voronoi algorithm

Contrast to the high cost and long fabrication workflow with wet or dry etching process for a glass-based micromodel with complex porous media patterns, this simple, fast and cost-effective fabricating method may produce amounts of micro-/nanofluidic models in a short time period (average twenty samples per day). Details of each fabrication process was discussed in the following sections.

2.2.1. Materials. For fabricating one complete glass-silicon-glass micromodel, two glass wafers were used as both the substrate and the cover-plate. The Schott Borofloat 33 Glass wafers are square double side polished (University Wafer), with the side length of 5 cm and the thickness of 500 ±20 μm. Silicon pellets (R.D. Mathis) were used as the evaporation material to be coated onto the glass substrate to enable an easy anodic bonding process with glass since they have the similar thermal coefficient of expansion. (For silicon is 2.6 x 10^{-6} /K and Borofloat 33 glass is 3.25 x 10^{-6}/K at 20°C).

2.2.2. Photolithography. First, the glass substrate was first rinsed with acetone and methanol for two times to remove dust and oil, and then blow-dried completely using dry air. The Microposit S1813 positive photoresist was spin coated uniformly onto the glass substrate at 4000 RPM for 40 s with the thickness of 1.3 microns.Then the substrate

was softbaked on the hot plate at 115 Celsius degrees for one minute to eliminate the moisture on the substrate. Later, the substrate was soft contact with the printed polymeric mask and exposed to UV400 ultra-violet (UV) light using Karl Suss MA6 aligner. The UV exposure time depends on the photo resist type. We used S1813 which requires 150mJ/cm^2. The exposure power of our mask aligner is about 11mW/cm^2 so the exposure time is 10-15s for our samples. Lastly, the exposed photoresist was removed by soaking the substrate into the MF321 developer for 50 s until the pattern can be seen clearly and then rinsed using deionized (DI) water for thirty seconds. One substrate contains two patterns to save the space of the substrate.

2.2.3. E-Beam Vapor Evaporation. Choosing a proper evaporation method for depositing a thin silicon film on the glass substrate is of great importance throughout the whole work. Different from chemical vapor deposition method (CVD) that takes place at high temperatures, E-beam evaporation allows depositions at relatively low substrate temperature around 16-50 Celsius degrees while yielding a high deposition rate (1.6 Å/s at temperatures 16 - 50 Celsius degree) and has been used for micro-electro-mechanical systems (MEMS) for a long time. (Bu et al., 2004; Han et al., 2003; J. Kim, Li, & Park, 2011) The low deposition temperature prevents the deformation of the glass wafers at high temperatures around 550 Celsius degrees. Thermal evaporation, being as another physical evaporation, may as well heat up the substrate to over 250-300 Celsius degree during deposition process.(Piegari & Flory, 2018) Besides, chemical vapor deposition may generate gaseous or liquid byproducts which may lead to impurities on the substrate. Except for these two reasons in terms of deposition temperature and contaminants, the most important reason for choosing e-beam physical evaporation is the consideration of the poor

step coverage of deposited film as shown in Figure 2(g) and (h). Although chemical deposition and physical sputtering both have better step coverage with isotropic deposition, this will lead to the full coverage of the surface of the substrate.

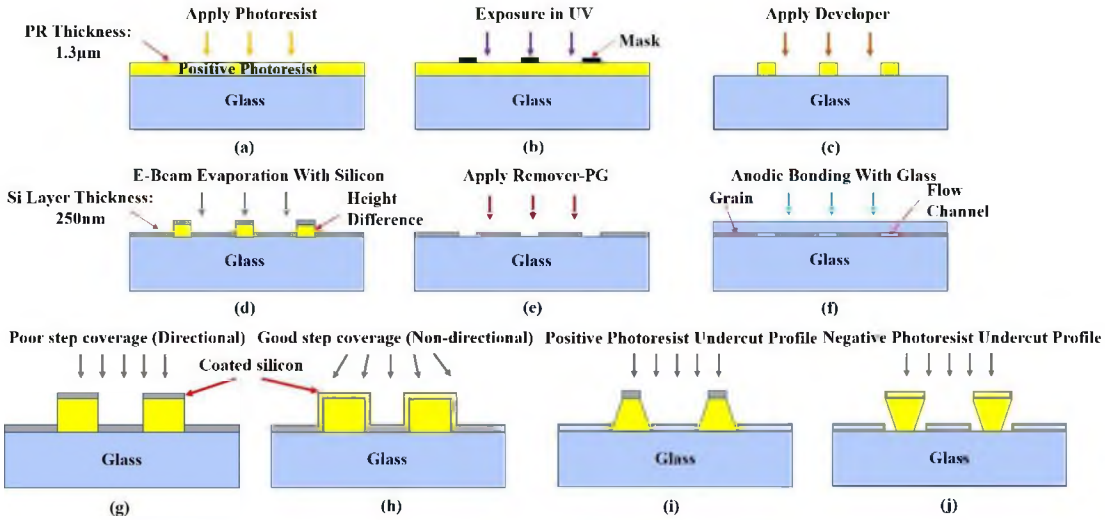

Figure 2. Schematic workflow of micro-/nanofluidic model fabrication process: (a) photoresist spin-coated on the glass substrate; (b) UV exposure to change the chemical properties of uncovered photoresist; (c) developer applied to wash away exposed photoresist; (d) e-beam evaporation used to deposit thin silicon later onto the glass substrate; (e) remover-PG used to remove residual photoresist in the channels; (f) anodic bonded with another glass wafer on top; (g)(h): illustration of deposition poor and good step coverage comparison; (i)(j): positive and negative photoresist undercut profile comparison when coated on the substrate

The deposition would happen not only on the top of the photoresists in the channels but also the sides, which prevents the photoresist from being washed away through the open sides. On the other hand, by leveraging the directional deposition of e-beam deposition with poor step coverage, the silicon will be only deposited onto the top of the photoresist, leaving the sides open to the air. Therefore, the photoresist can be washed away easily through the open sides. To ensure the thorough removal of the photoresist, the

silicon layer should be better coated less than one fourth of the photoresist layer thickness, which is 1.3 μm, to give more height difference between the photoresist layer and the silicon layer on the substrate. Thus, we chose to deposit 250 nm silicon layer. The photoresist patterned substrate was loaded in the E- beam evaporation chamber, which was pumped down to $2e^{-6}$ Torr base pressure. The E- beam deposition is at an average rate of 1.6 Å/s at temperatures 16 – 50 Celsius degree, thus it only takes no more than thirty minutes to reach ~250 nm for all loaded samples (20 per load with the sample dimension of 2 cm ×2 cm).

2.2.4. Lift-off Process. The lift-off process after thin film deposition has been used for decades in semiconductor and integrated circuit (IC) areas as a simple and quick method for patterning thin metal material films. (Y.-J. Chen, Hsu, & Lin, 2005; Weichel, De Reus, & Lindahl, 1998; Widmann, 1976) However, it has rarely been brought into microfluidic model fabrication field. We herein utilized direct lift-off process after the E- beam evaporation process to wash away the remaining photoresists in the channels. The substrate was first soaked in the Remover-PG solution and let it stand for 10 mins. Then, the ultrasonic cleaner with deionized water was used to clear out most of the photoresist preliminarily. Later, the substrate was cleaned intensively by immersing into the Piranha Solution (3:1 H_2SO_4:H_2O_2) for 20 mins to remove the photoresist residue and other contaminants. Finally, the substrate was rinsed by deionized water and blow-dried thoroughly. The lift-off process would peel off the photoresist with top-coated silicon layers from the substrate completely, leaving the channels clean to give spaces for fluid flow. However, in some situations due to improper and incomplete dissolution of the photoresist, the retention problem would occur. The top coated silicon would adhere to the

bottom silicon grain that should remain. To handle this problem, we conducted several lift-off processes with deposited silicon layers of different thickness from 100 nm to 500 nm with interval of 50 nm. It was not surprised that the thicker the deposited silicon layers, the more possible for retention problem occurs which causes more difficultulties to wash away the photoresist. Either the side windows were too small to let the remover-PG flush completely or the silicon grains were peeled off together with the photoresist. The deposited material layer should not be thicker than two thirds of the photoresist to ensure a complete separation.(Smith, 1974) However, we found that it began to become difficult when the deposited silicon layer thickness is above 300 nm, which is about one fourth of the photoresist thickness (1.3 μm). It i s also the nature of the positive photoresist that limits the height of the deposition layer. As shown in Figure 2(i) and (j), the undercut profiles are different between positive and negative photoresist with the silicon deposited on the top. They both have trapezoidal shapes after exposion. However, the undercut profile of positive resist is less advantageous than that of the negative photoresist whose inverted one has much bigger open access to the remover-PG solution. Although negative resist has been used mostly in lift-off process in microelectronic field, the higher cost and the difficult removal process still need to be considered. A diffuser by diverting the UV light can be utilized to change the positive photoresist undercut profile to the re-entrant profile for facilitating the lift-off process.(H. S. Lee & Yoon, 2005) For our experiment, we did not use any other auxiliary method to ease the lift-off process since we seriously controlled the deposited silicon layer thickness below one fourth of the positive photoresist thickness to achieve a complete lift-off process.

2.2.5. Surface and Channel Characteristics. After the lift-off process, the surface and the channel characteristics were analyzed. The thickness of the deposited silicon was measured using Sloan Dektak 3030 surface profiler measuring system. The probe went 300 μm across of two random grains and measured the channel depth between them. Inside the test area, the channel width is approximately 20 μm and the depth is about 277.7 nm. The surface is of good flatness, except for a few sharp peaks caused possibly by the dusts on the substrate surface. To demonstrate the profile of channel side wall, scanning electron microscopy (SEM) images of the model in tilt 45 degrees angle were taken using Hitachi S-4700 FESEM microscope as shown in Figure 3. Figure 3(a) shows the top overview of one part of the matrix and adjacent micro-fractures generated using Voronoi tessellation algorithm, which shows the matrix parts with smaller pore size while the micro-fractures with the larger pore size. Although the channel may have some degree of roughness due to the lift-off process, as shown in Figure 3(b) and (c), the channel side wall is shown to be vertical to the substrate as shown in Figure 3(d), which has better profile than wet etching.

2.2.6. Anodic Bonding. Anodic bonding can deliver strong bonding strength while keeping the substrate at low temperature.(Knowles & Van Helvoort, 2006) Glass to glass anodic bonding can be realized by using silicon or other metal films as the intermediate layers and anodic bonding at no more than 400 Celsius degrees and 700 Volts to make it possible for optical detection with fluorescence microscopy in biological and biomedical field, microfluidic systems where transparent walls were demanded.(Berthold, Nicola, Sarro, & Vellekoop, 2000; Kameoka & Craighead, 2001; Knapkiewicz et al., 2011; Kutchoukov et al., 2004)

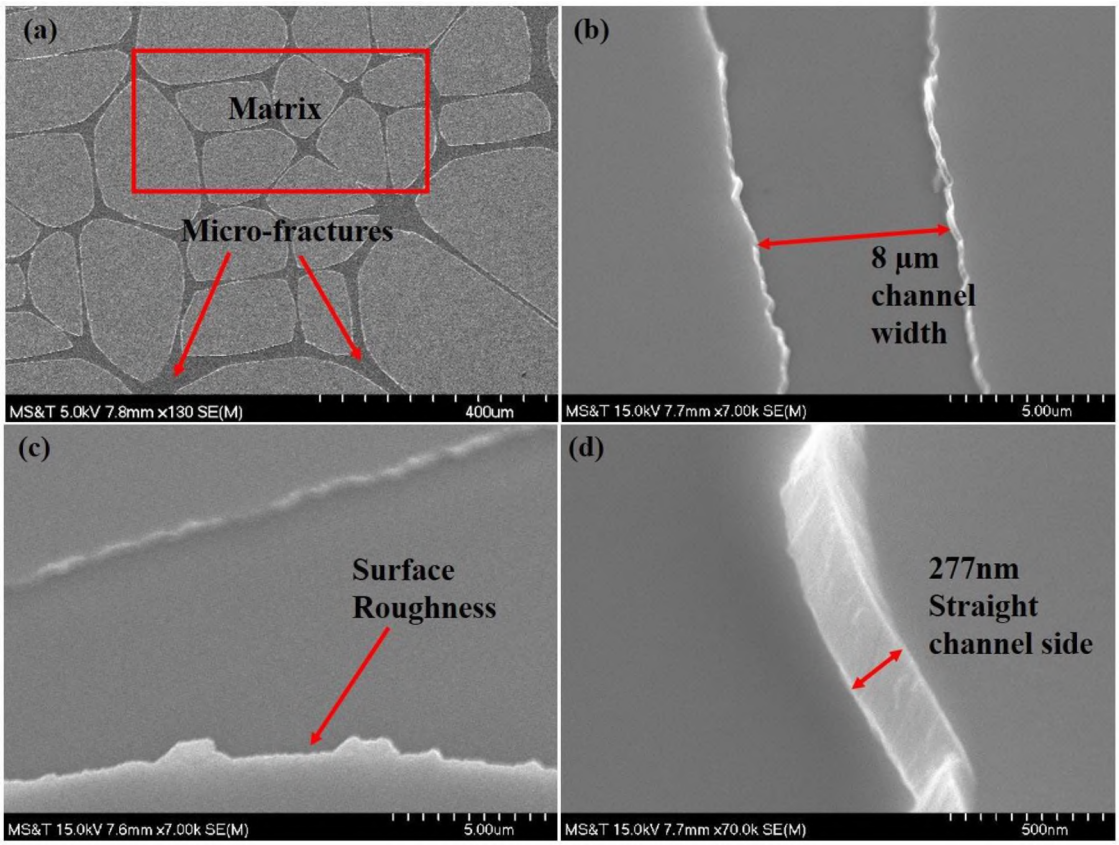

Figure 3. SEM images of (a) matrixes and micro-fractures demonstration; (b) matrix channel with the width of 8 µm; (c) sidewall roughness; (d) straight channel wall profile with the depth of 277 nm

We used our self-assembly anodic bonding device to conduct the final anodic bonding process to seal the glass substrate with silicon layer and the plain glass cover hermetically. As shown in Figure 4, Our self-assembly anodic bonding device includes a HP Keysight 6515A high voltage DC power supple (0-1600V, 5mA), a hot plate with an aluminum-foil paper covered, an ammeter and a probe stand with a metal probe fixed. An aluminum-foil paper was wrapped over the hot plate surface tightly as the conducting layer. The substrate with the silicon layer was placed first onto the aluminum as layer 1, followed with the placement of the cover glass onto the substrate as layer 2. Before placing, the

substrate and the cover glass were already rinsed together in Piranha Solution (3:1 H_2SO_4:H_2O_2) for 20 mins after lift-off process to avoid bonding issue because of the residual contaminants.

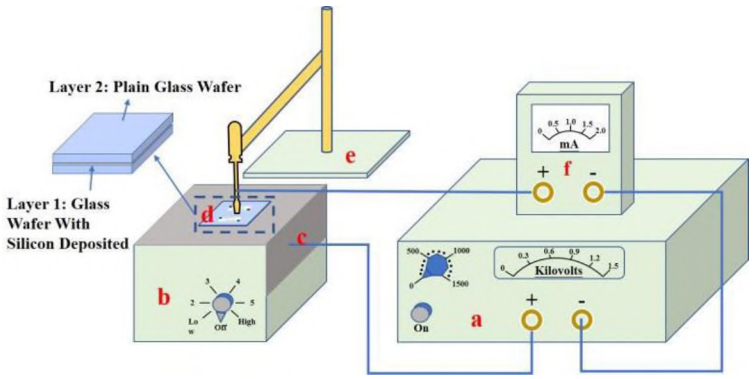

Figure 4. Schematic of the lab-based anodic bonding apparatus. A. high voltage DC power supple (0-1600V,5mA); b. hot plate; c. aluminum paper; d. two glass wafers with an intermediate silicon layer; e. probe stand; f. amperemeter

The SEM images also show there are not visible additive residues in the channels. In the meantime, they were both changed to have strong hydrophilicity. The conductive probe was adjusted vertically to press onto the cover glass to initially apply a force for a pre-bond. By connecting the anode to the aluminum-foil paper and cathode to the probe through the ammeter, the preparation for bonding was finished. We then switched on the hotplate and set the goal temperature to around 350 Celsius degrees and wait the substrate be pre-heated for 10 minutes. We used an infrared thermometer to measure the surface temperature. After the temperature was stable around 350 Celsius degrees, we slowly increased the voltage to 1200V and check the ammeter at the same time. The ammeter was being an indicator whether there is a short circuit occurred when increasing the voltage. If

the current is over 1 mA at any time during voltage incensement, the voltage should decrease to zero and check the electrodes connections. The bonding process using point cathode electrode contact method can be observed, spread radially outwards from the probe pinpoint. This radial propagation process also avoids air rapping between the interface of glass and silicon. However, the bonding process cannot be completed only by contacting one point due to the large area of the chip surfaces. Therefore, whenever the spread stopped, we moved the conductive probe to another point to continue the bonding process until all parts were bonded together. This point contact bonding method is much faster than the flat cathode electrode contact method and also costless.(Tripathi, Jain, Joshi, Sood, & Kumar, 2008) It is also noteworthy that there were no collapsed channels found after the anodic bonding process. The channel aspect ratio (depth to width) has been demonstrated to be a crucial diameter when conducting a bonding process for either glass-silicon or glass-glass models.(Mao & Han, 2005) For a glass cover anodic bonded onto a silicon substrate, due to the applied strong electrical force, the top and bottom surfaces would contact and seal the channel permanently if the aspect ratio is smaller than 0.004. For a fusion bonding process between two glass wafers, the high temperature would deform the glass material and thus cause the collapse of the channels if the aspect ratio is smaller than 0.0005. For our anodic bonding process under low temperature, there are also no strong electrical interactions between the top and bottom glass wafers. Therefore, the channels were all survived with the aspect ratio even smaller than 0.0005.(e.g. conduits and the vugs).

3. EXPERIMENTAL VERIFICATION FOR THE GLASS-SILICON-GLASS MICROMODEL

We tested the practicability of the glass-silicon-glass micromodel by conducting a two-phase fluid displacement experiment. Deionized water (DI water) was used as the wetting phase and decane as the non-wetting phase. The fluid flow process was investigated by utilizing confocal laser scanning microscopy (CLSM). To distinguish the two kinds of fluids under different lasers, they were both fluorescent-dyed using Alexa Flour 594 for the water phase and Nile Red for the oil phase (both from Sigma-Aldrich), respectively. The DI water was in red and the decane was in green after separately excited by lasers at 488 nm and 561 nm. The micromodel was firstly saturated with the decane injected by using syringe pump (Harvard Apparatus, model 88-3015). Then the decane was displaced by the DI water at the flow rate of 0.02 mL/hr. Because it is a large field micromodel, even if we used 10 X objective lens that have the biggest vision of field among all lenses, we can only observe partial areas. Therefore, the stage was set moved automatically from left corner inlet to the right corner outlet with 19 horizontal steps and 5 vertical steps. All fields were then stitched together to obtain a whole image which covers all parts of the model. We scanned and recorded the whole injecting process using resonant scanning mirrors instead of traditional galvanometer mirrors to acquire high scanning speed. Although the resolution became worse, the scanning speed can be up to 7.7 frame per second and it takes only 40 seconds to scan the whole model. All experiments were conducted at room temperature.

3.1. OIL SATURATION PROCESS

In this research, since our focus is to fabricate the model and verify its usability to conduct a flooding experiment, we did not consider the irreducible water saturation to mimic the real reservoir saturation history as it is neglectable for verifying the usability of this model. Therefore, we only did the water flooding imbibition test by directly saturating the model with oil first. Decane (0.92 cP at 20°C) was injected using 1/16-inch inner diameter tubing into the inlet nanoport (IDEX Health & Science LLC) at flow rate of 0.02mL/L. As shown in Figure 5, it took about 10 hours to fully saturate the microfluidic model with decane phase. The flow direction was from top left corner inlet to the bottom right outlet where was always open to the air with no backpressure added. From the time sequence from top to the bottom with the time interval of 2 hours, we can observe that the intensity of fluorescent was increased with the gradually saturation of the oil phase. From T =4 hrs, the flow started to flow into the bottom conduit, mostly from the middle micro-fractures other than the matrix at left, which verifies the assumption for the interface conditions in to govern the coupled flow in a dual-porosity media and its adjacent conduits(Hou et al., 2016). At T = 6 hrs, the bottom conduit has more fluid flown into than the matrix at right. Until the end of the injection, except for the left corner of the bottom conduit, all the top and bottom conduits were saturated, together with the two matrixes and micro-fractures. The bonding failure may occur at the edges of the inlet and outlet, as well as some edges at the matrix boundaries as indicated in Figure 5 (T= 10 hrs). The partial bonding failure would not affect the general trend of the fluid flow inside the porous media seriously. We did not observe any leakage from the chip until the injecting pressure was higher than 420 Psi when the solidified epoxy that fixed the nanoport on the chip started to

crack and leak but not for other parts of the model. However, our injecting pressure was no more than 200 Psi so there was no leakage observed throughout the experiments.The water phase was then ready to be injected until there was no fluorescent intensity increase observed which means the porous media was fully saturated with the decane oil phase.

3.2. FORCED WATER IMBIBITION PROCESS

We conducted the water imbibition processes in two directions with constant flow rate of 0.02mL/hr. One is positive injection from the inlet, another one is reverse injection from the outlet. The two matrixes were adjacent to the bottom conduit when the water was forwardly injected into the micromodel, while adjacent to the top conduit when the water was reversely injected. The decane oil phase and water phase were in true excitation color of green and red. Both two imbibition processes were successful with no leakage found and stopped at about fifty minutes when no more significant phase changes after water breakthrough within the models. Because of the strong hydrophilicity of glass and silicon layer after rinsed in piranha solution before bonding, and with the very low flow rate, the water intended to be imbibed into the matrixes first other than micro- fractures from top conduit. For the forward injection process as shown in Figure 6, the water started to invade into the top conduit and imbibed into the first matrix at the same time at around 5 minutes from the imbibition beginning. The waterflow then branched into two different directions. One branch continued to flow in the conduit and another branch flew into the bottom conduit. Although some of the water in the matrix flew into the middle micro-fractures, quicker flow velocity was found at top and bottom conduits. Consequently, at T=8

minutes, the water from the top conduit was imbibed into the second matrix and started to displace the oil into the bottom conduit forced by the backpressure of water behind it.

Since the decane oil is less viscous than the water, a fingering phenomenon was observed as the oil flow had a finger-like structure as it travelled towards the outlet while remained connected. Besides, as the pressure built up within the whole model, part of the remaining oil at upstream conduit was also started to be displaced and also acted finger-like when it met the water that has already been in the top conduit as shown at T=10 and 15 minutes. The fingering became more remarkable at T=30 minutes at both conduits and some of the matrixes and micro-fractures were re-saturated by some upstream remaining oil. From T=30 minutes to T=50 minutes, there were no other significant changes, but some connected finger-like oil was stretched longer or disconnected into dispersed oil droplets by the continuously water flooding. The fingering phenomenon was also found in the reverse injection process. However, it happened mostly only in the bottom conduit while only rare were found in the top conduit as shown in Figure 7. At the beginning, the water flew uniformly into the top conduit with much less remaining oil left at upstream conduit. The water reached the first matrix on the top at T=6 to T=8 minutes and imbibed into it. Meanwhile, some water was also diverted towards the left-side vug. At T=9 minutes, the water in the first matrix started to flow into the bottom conduit and continued to flow right to the middle micro-fractures afterwards. As the water in the top conduit insisted to reach the second matrix at the top right corner, the water in the micro- fractures firstly flew into the bottom conduit and converge with water from the second matrix later at T=10 minutes.

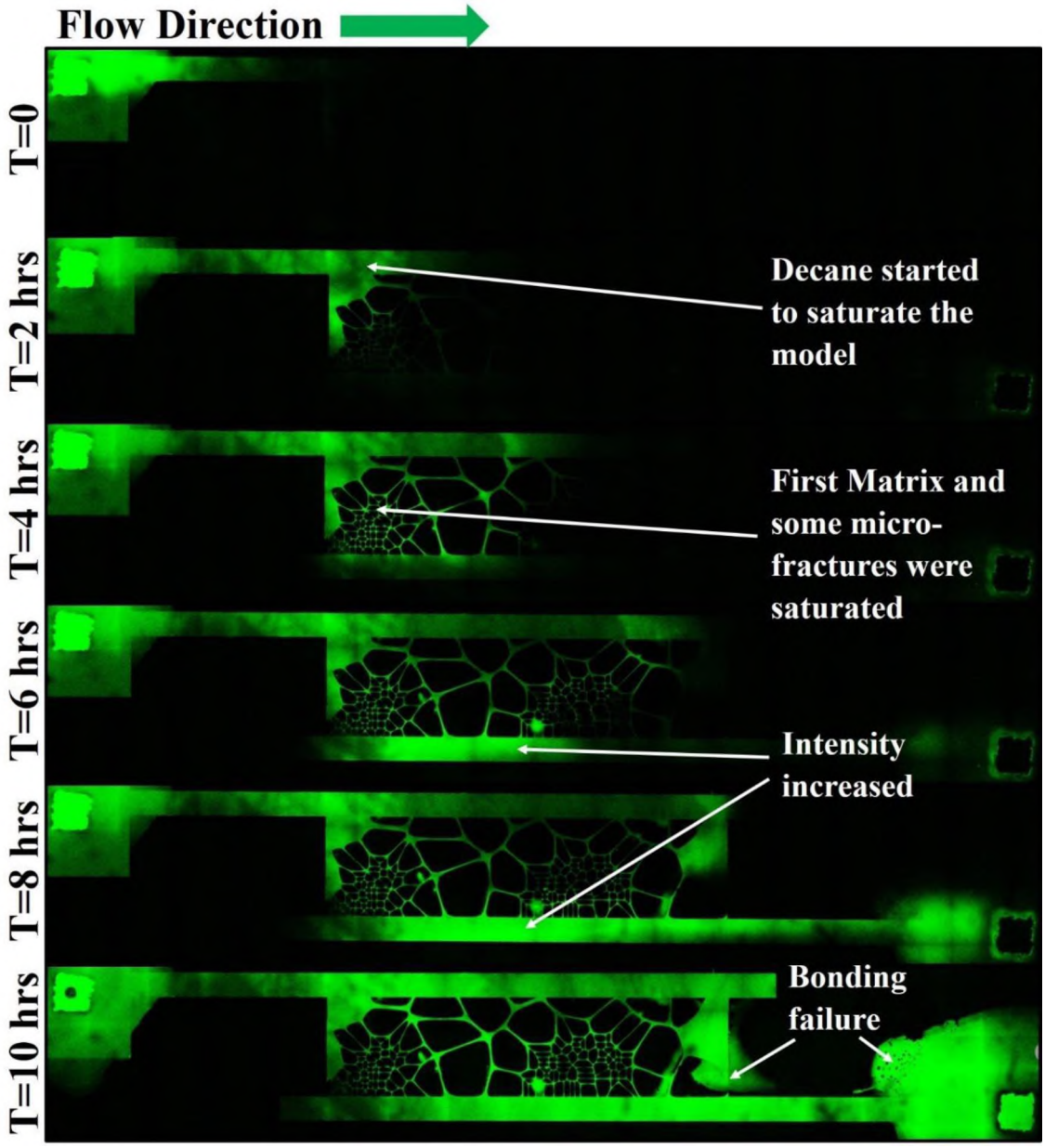

Figure 5. Oil saturation process in a time sequence (top to bottom) with flow direction (left to right)

The fingering occurred in the bottom conduit at T=15 minutes as the upstream remaining oil in the bottom conduit was displaced towards the outlet and became the most serious at T=50 minutes. Although there was also some fingering observed at the boundaries of the top conduit, it was much less significant than that of the scenario in

which the water was forwardly injected. The hypothesized reason is that, when the water was forwardly injected, the two matrixes were much closer to the inlet, which may generate a strong imbibition area for the water at the very beginning of the flooding process. On the contrast, the two matrixes were adjacent to the top conduit and farther to the inlet. Therefore, the water would not prefer to flow into the micro- fracture at the beginning, but rather to flow steadily in the top conduit until reached the first matrix. Thus, there were much less remaining oil left at the upstream since most of them were already been displaced through the top conduit. As a result, the fingering was not likely to be found in the top conduit for the reverse injection scenario, which in return leads to a higher oil recovery.

3.3. RESIDUAL OIL DISTRIBUTION COMPARISON

The residual oil is the oil that cannot be recovered by simple conventional water flooding method. We repeated the experiments in other two models built with the same method and still found the residual oil was much less when the two matrixes were adjacent to the top conduit than that of the case in which the two matrixes were adjacent to the bottom conduit. For both cases, the residual oil would exist in different forms within the matrixes as shown in Figure 8(a) and (b) and the microfractures as shown in Figure 8(c) and (d). Some of them were adhered to the rough surface and cannot be displaced by the water while most of them left in the middle of the channel in different shapes. Besides, snap-off was also observed at very thin matrix channel, resulting in slugs of oil droplet trapped in the pore throat with water phase filled among them. It was also found that the re-saturated oil can be hardly driven by following water flooding process when the two

matrixes were adjacent to the bottom conduit, which causes much more residual oil as shown in Figure 8(b) and (d) than that of reverse injection case as shown in Figure 8(a) and (c). However, the residual oil distributed similarly in the bottom conduit for both cases, as the finger-structured oil plumes were destroyed by constantly water flooding and randomly dispersed with the direction pointing to the outlet.

4. CONCLUSIONS AND FUTURE WORK

We successfully used e-beam physical evaporation deposition, lift-off process and anodic bonding method to fabricate a fully transparent, shale-like dual-porosity glass-silicon- glass micro-nonofluidic model in a simple, fast and low-cost way. The fabrication process gets rid of the time-consuming and complicated etching method while still generates complex porous media network with uniform channels in a much shorter time. To verify the functionally and practicability of the model, two phase fluid flow displacement experiments with two injection modes were conducted separately and visualized using confocal laser scanning microscope. Owing to the large width-to-depth ratio range (12-2000) of the model, especially for two conduits at top and bottom, the fingering phenomena that may happen in a Hele-Shaw cell were brought into sight. Moreover, we observed that it is possible the fingering problem could exist when displacing phase viscosity is higher than that of the displaced phase due to the geometry of the porous media. Besides, the residual oil distributed as different forms in the matrixes, micro-fractures and conduits. Snap-offed oil droplets trapped in thin channel pore throat, oil chains left in the wider matrix channels, boundary-adhered oil films due to the surface

roughness, and the dispersed oil droplets in the conduits were found, respectively. By changing the flow pattern by shifting two matrixes adjacent to the bottom and then top conduits, we demonstrated that different matrix/micro- fracture/macro-fracture interlacing geometries that may affect flow patterns, which would affect the oil recovery seriously for dual-porosity heterogeneous shale porous media. Although this micro-/nanofluidic model provides with a quick and simple platform for direct visualizing the fluid flow dynamically in a dual-scale porous media, there are still further expectations for the future work. The micro-/nanofludic model can be improved by designing more different patterns that representing more complicated reservoir conditions. The limitation of depth-to-width aspect ratio by using glass-glass anodic bonding method still needs further investigated, which would provide the possibility of fabricating the micromodel even at sub-10 nm scale. The residual oil distribution, flow velocity, pressure difference and fingering problem are still need further researched quantitatively and systematically to get a comprehensive understanding of the fluid flow within dual-scale micro-/nano channels at pore level.

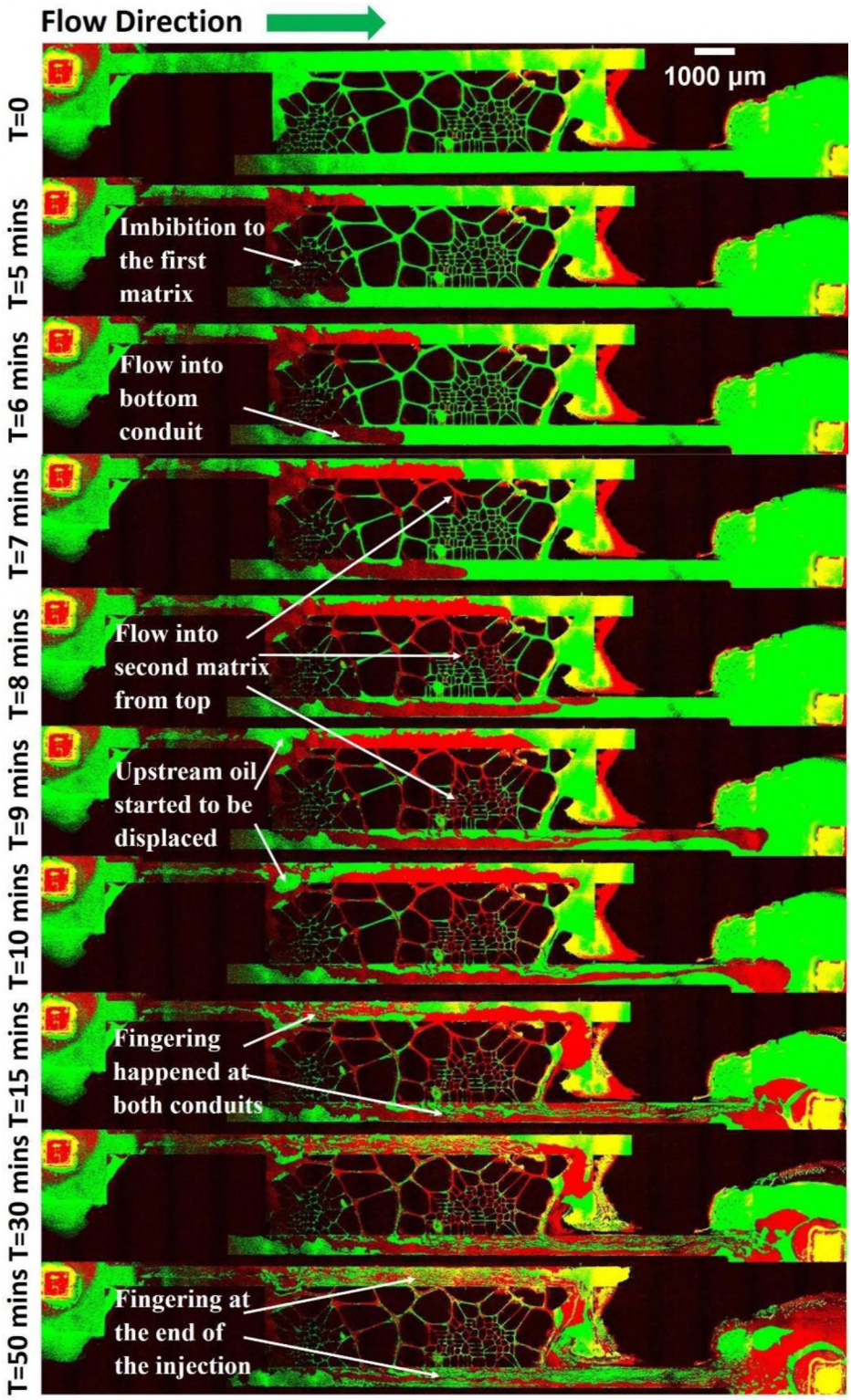

Figure 6. Water imbibition process in a time sequence (top to bottom) with flow direction (left to right)

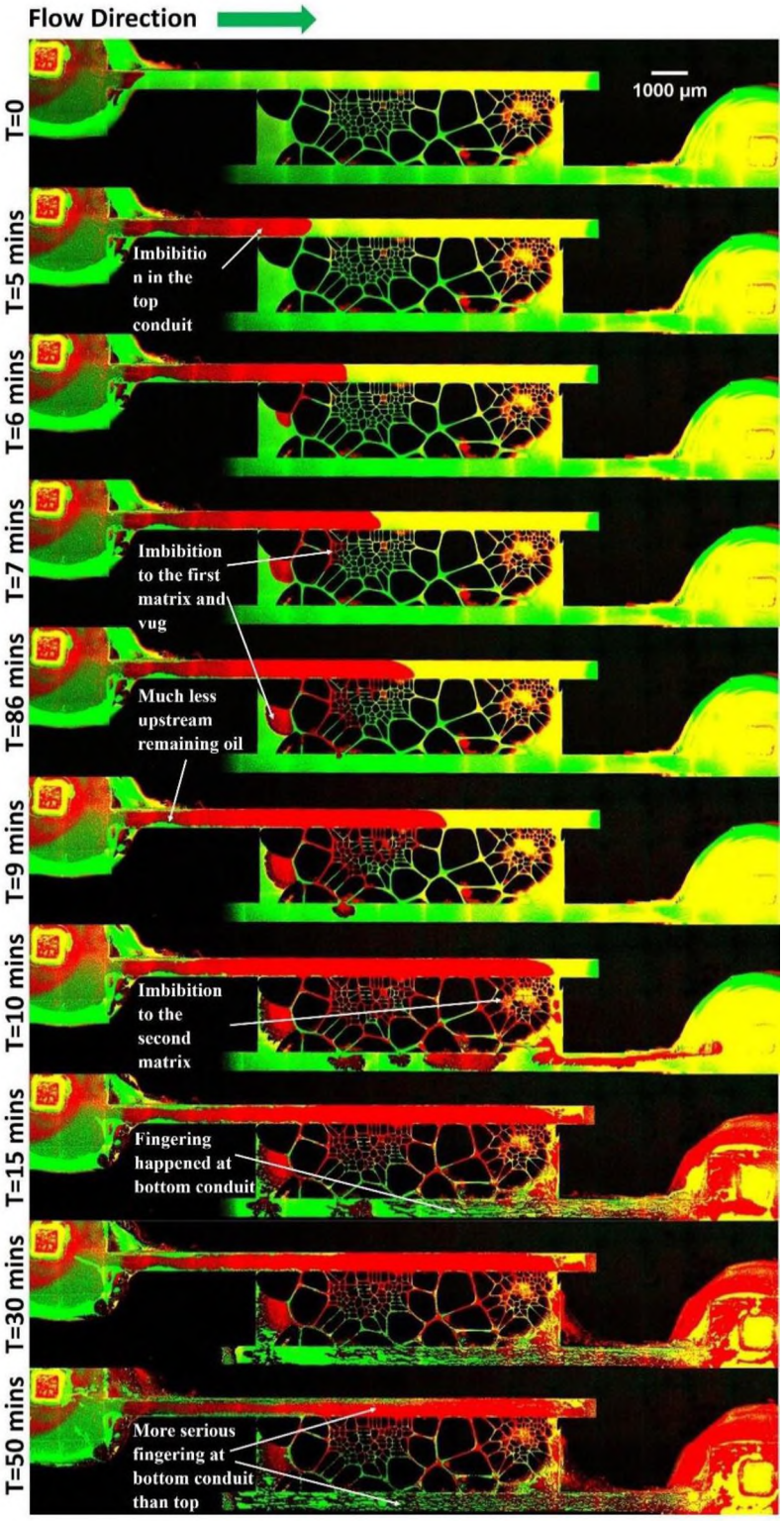

Figure 7. Reverse water imbibition process in a time sequence (top to bottom) with flow direction (left to right)

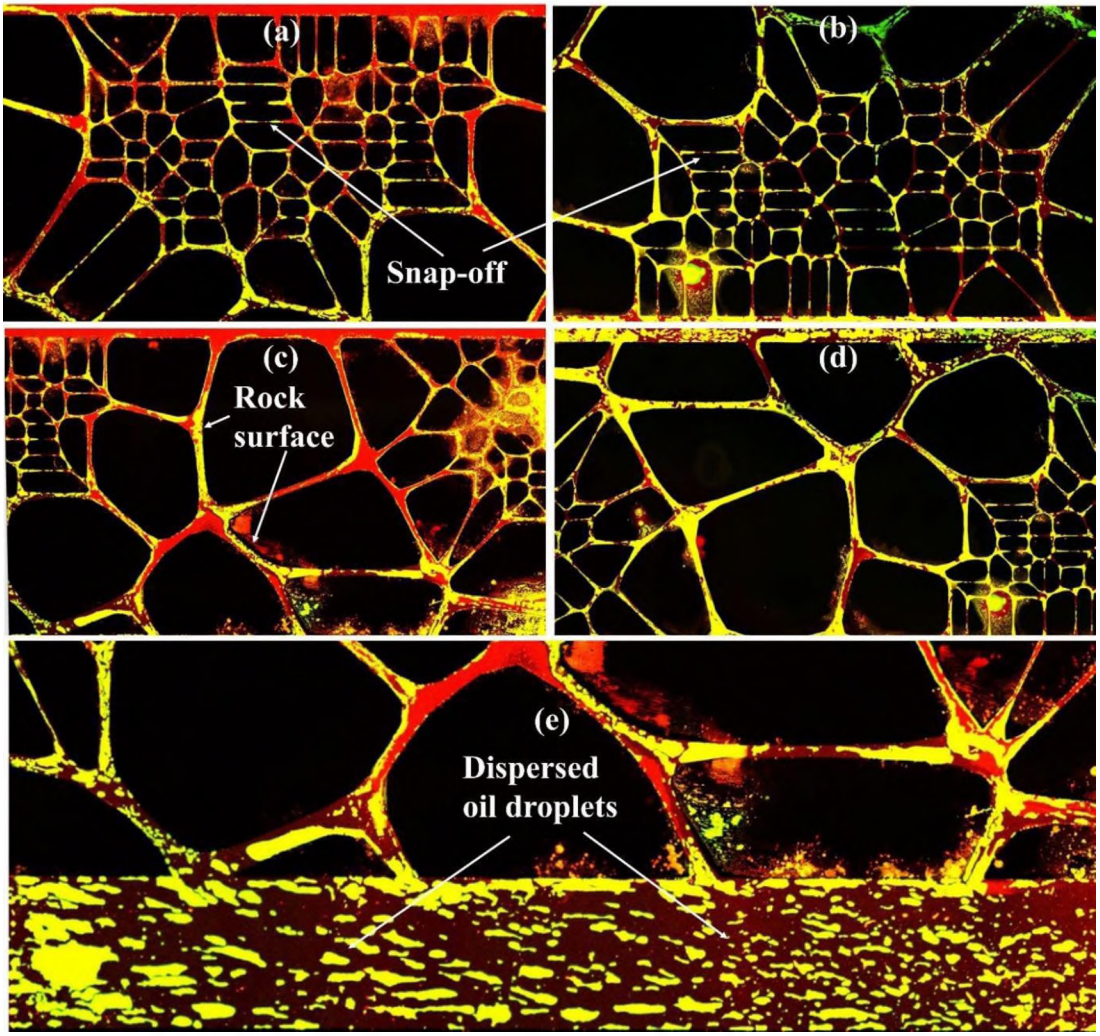

Figure 8. Residual oil distribution conditions comparisons in matrixes, micro-fractures of two different geometries (a) and (c) top conduit with adjacent matrixes; (b) and (d) bottom conduit with adjacent matrixes; (e) bottom conduit

REFERENCES

Alfi, M., Nasrabadi, H., & Banerjee, D. (2016). Experimental investigation of confinement effect on phase behavior of hexane, heptane and octane using lab-on-a-chip technology. Fluid Phase Equilibria, 423, 25-33.

Anbari, A., Chien, H. T., Datta, S. S., Deng, W., Weitz, D. A., & Fan, J. (2018). Microfluidic model porous media: fabrication and applications. Small, 14(18), 1703575.

Berthold, A., Nicola, L., Sarro, P., & Vellekoop, M. (2000). Glass-to-glass anodic bonding with standard IC technology thin films as intermediate layers. Sensors and Actuators A: Physical, 82(1-3), 224-228.

Bien, D., Rainey, P., Mitchell, S., & Gamble, H. (2003). Characterization of masking materials for deep glass micromachining. Journal of Micromechanics and Microengineering, 13(4), S34.

Bora, R., Maini, B., & Chakma, A. (2000). Flow visualization studies of solution gas drive process in heavy oil reservoirs using a glass micromodel. SPE Reservoir Evaluation & Engineering, 3(03), 224-229.

Boruah, A., Rasheed, A., Mendhe, V. A., & Ganapathi, S. (2019). Specific surface area and pore size distribution in gas shales of Raniganj Basin, India. Journal of Petroleum Exploration and Production Technology, 9(2), 1041-1050. doi:10.1007/s13202- 018-0583-8

Bu, M., Melvin, T., Ensell, G. J., Wilkinson, J. S., & Evans, A. G. (2004). A new masking technology for deep glass etching and its microfluidic application. Sensors and Actuators A: Physical, 115(2-3), 476-482.

Buchgraber, M., Al-Dossary, M., Ross, C., & Kovscek, A. R. (2012). Creation of a dual-porosity micromodel for pore-level visualization of multiphase flow. Journal of petroleum science and engineering, 86, 27-38.

Castano-Alvarez, M., Ayuso, D. F. P., Granda, M. G., Fernández-Abedul, M. T., García, J. R., & Costa-García, A. (2008). Critical points in the fabrication of microfluidic devices on glass substrates. Sensors and Actuators B: Chemical, 130(1), 436-448.

Chen, X., & Zhang, L. (2018). Review in manufacturing methods of nanochannels of bio-nanofluidic chips. Sensors and Actuators B: Chemical, 254, 648-659.

Chen, Y.-J., Hsu, J.-H., & Lin, H.-N. (2005). Fabrication of metal nanowires by atomic force microscopy nanoscratching and lift-off process. Nanotechnology, 16(8), 1112.

Civan, F., Rai, C. S., & Sondergeld, C. H. (2011). Shale-gas permeability and diffusivity inferred by improved formulation of relevant retention and transport mechanisms. Transport in porous media, 86(3), 925-944.

Conn, C. A., Ma, K., Hirasaki, G. J., & Biswal, S. L. (2014). Visualizing oil displacement with foam in a microfluidic device with permeability contrast. Lab on a Chip, 14(20), 3968-3977.

Doryani, H., Malayeri, M., & Riazi, M. (2016). Visualization of asphaltene precipitation and deposition in a uniformly patterned glass micromodel. Fuel, 182, 613-622.

Geng, J., Ding, H., Han, P., Wu, Y., & Bai, B. (2018). Transportation and Potential Enhanced Oil Recovery Mechanisms of Nanogels in Sandstone. Energy & fuels, 32(8), 8358-8365.

Geng, J., Pu, J., Wang, L., & Bai, B. (2018). Surface charge effect of nanogel on emulsification of oil in water for fossil energy recovery. Fuel, 223, 140-148.

Grate, J. W., Kelly, R. T., Suter, J., & Anheier, N. C. (2012). Silicon-on-glass pore network micromodels with oxygen-sensing fluorophore films for chemical imaging and defined spatial structure. Lab on a Chip, 12(22), 4796-4801.

Grate, J. W., Warner, M. G., Pittman, J. W., Dehoff, K. J., Wietsma, T. W., Zhang, C., & Oostrom, M. (2013). Silane modification of glass and silica surfaces to obtain equally oil-wet surfaces in glass-covered silicon micromodel applications. Water Resources Research, 49(8), 4724-4729.

Gunda, N. S. K., Bera, B., Karadimitriou, N. K., Mitra, S. K., & Hassanizadeh, S. M. (2011). Reservoir-on-a-Chip (ROC): A new paradigm in reservoir engineering. Lab on a Chip, 11(22), 3785-3792.

Han, A., Wang, O., Graff, M., Mohanty, S. K., Edwards, T. L., Han, K.-H., & Frazier, A. B. (2003). Multi-layer plastic/glass microfluidic systems containing electrical and mechanical functionality. Lab on a Chip, 3(3), 150-157.

Herrick, R. F., McClean, M. D., Meeker, J. D., Baxter, L. K., & Weymouth, G. A. (2004). An unrecognized source of PCB contamination in schools and other buildings. Environmental Health Perspectives, 112(10), 1051-1053.

Hou, J., Qiu, M., He, X., Guo, C., Wei, M., & Bai, B. (2016). A dual-porosity-Stokes model and finite element method for coupling dual-porosity flow and free flow. SIAM Journal on Scientific Computing, 38(5), B710-B739.

Iliescu, C., Chen, B., & Miao, J. (2008). On the wet etching of Pyrex glass. Sensors and Actuators A: Physical, 143(1), 154-161.

Iliescu, C., Taylor, H., Avram, M., Miao, J., & Franssila, S. (2012). A practical guide for the fabrication of microfluidic devices using glass and silicon. Biomicrofluidics, 6(1), 016505.

Jia, Z.-J., Fang, Q., & Fang, Z.-L. (2004). Bonding of glass microfluidic chips at room temperatures. Analytical chemistry, 76(18), 5597-5602.

Kameoka, J., & Craighead, H. (2001). Nanofabricated refractive index sensor based on photon tunneling in nanofluidic channel. Sensors and Actuators B: Chemical, 77(3), 632-637.

Kanno, Y., Ino, K., Shiku, H., & Matsue, T. (2015). A local redox cycling-based electrochemical chip device with nanocavities for multi-electrochemical evaluation of embryoid bodies. Lab on a Chip, 15(23), 4404-4414.

Karadimitriou, N., & Hassanizadeh, S. (2012). A review of micromodels and their use in two-phase flow studies. Vadose Zone Journal, 11(3).

Kawai, K., Yamaguchi, F., Nakahara, A., & Shoji, S. (2010). Fabrication of vertical and high-aspect-ratio glass microfluidic device by borosilicate glass molding to silicon structure. Paper presented at the 14th international conference on miniaturized systems for chemistry and life sciences.

Kazemifar, F., Blois, G., Kyritsis, D. C., & Christensen, K. T. (2015). A methodology for velocity field measurement in multiphase high-pressure flow of CO2 and water in micromodels. Water Resources Research, 51(4), 3017-3029.

Kelly, S. A., Torres-Verdín, C., & Balhoff, M. T. (2016). Subsurface to substrate: dual-scale micro/nanofluidic networks for investigating transport anomalies in tight porous media. Lab on a Chip, 16(15), 2829-2839.

Kim, J., Li, Z., & Park, I. (2011). Direct synthesis and integration of functional nanostructures in microfluidic devices. Lab on a Chip, 11(11), 1946-1951.

Knapkiewicz, P., Cichy, B., Posadowski, W., Tadaszak, K., Sniadek, P., & Dziuban, J. (2011). Anodic bonding of glass-to-glass through magnetron spattered nanometric silicon layer. Procedia Engineering, 25, 1629-1632.

Knowles, K., & Van Helvoort, A. (2006). Anodic bonding. International materials reviews, 51(5), 273-311.

Kovarik, M. L., & Jacobson, S. C. (2009). Nanofluidics in lab-on-a-chip devices. In: ACS Publications.

Kutchoukov, V., Laugere, F., van Der Vlist, W., Pakula, L., Garini, Y., & Bossche, A. (2004). Fabrication of nanofluidic devices using glass-to-glass anodic bonding. Sensors and Actuators A: Physical, 114(2-3), 521-527.

Lee, H. S., & Yoon, J.-B. (2005). A simple and effective lift-off with positive photoresist. Journal of Micromechanics and Microengineering, 15(11), 2136.

Lee, J. N., Park, C., & Whitesides, G. M. (2003). Solvent compatibility of poly (dimethylsiloxane)-based microfluidic devices. Analytical chemistry, 75(23), 6544-6554.

Lefortier, S. G., Hamersma, P. J., Bardow, A., & Kreutzer, M. T. (2012). Rapid microfluidic screening of CO 2 solubility and diffusion in pure and mixed solvents. Lab on a Chip, 12(18), 3387-3391.

Liang, F., Ju, A., Qiao, Y., Guo, J., Feng, H., Li, J. Lu, Z. (2016). A simple approach for an optically transparent nanochannel device prototype. Lab on a Chip, 16(6), 984-991.

Lifton, V. A. (2016). Microfluidics: an enabling screening technology for enhanced oil recovery (EOR). Lab on a Chip, 16(10), 1777-1796.

Lin, Y., Yu, X., Wang, Z., Tu, S.-T., & Wang, Z. (2010). Measurement of temperature-dependent diffusion coefficients using a confocal Raman microscope with microfluidic chips considering laser-induced heating effect. Analytica chimica acta, 667(1-2), 103-112.

Maghzi, A., Mohammadi, S., Ghazanfari, M. H., Kharrat, R., & Masihi, M. (2012). Monitoring wettability alteration by silica nanoparticles during water flooding to heavy oils in five-spot systems: A pore-level investigation. Experimental Thermal and Fluid Science, 40, 168-176.

Mao, P., & Han, J. (2005). Fabrication and characterization of 20 nm planar nanofluidic channels by glass–glass and glass–silicon bonding. Lab on a Chip, 5(8), 837-844.

Mao, P., & Han, J. (2009). Massively-parallel ultra-high-aspect-ratio nanochannels as mesoporous membranes. Lab on a Chip, 9(4), 586-591.

Müller, R., Schmid, P., Munding, A., Gronmaier, R., & Kohn, E. (2004). Elements for surface microfluidics in diamond. Diamond and related materials, 13(4-8), 780-784.

Nelson, P. H. (2009). Pore-throat sizes in sandstones, tight sandstones, and shales. AAPG bulletin, 93(3), 329-340.

Okabe, A., Boots, B., Sugihara, K., & Chiu, S. N. (2009). Spatial tessellations: concepts and applications of Voronoi diagrams (Vol. 501): John Wiley & Sons.

Park, J., Lee, N.-E., Lee, J., Park, J., & Park, H. (2005). Deep dry etching of borosilicate glass using SF6 and SF6/Ar inductively coupled plasmas. Microelectronic engineering, 82(2), 119-128.

Parsa, E., Yin, X., & Ozkan, E. (2015). Direct observation of the impact of nanopore confinement on petroleum gas condensation. Paper presented at the SPE Annual Technical Conference and Exhibition.

Peng, R., & Li, D. (2016). Fabrication of polydimethylsiloxane (PDMS) nanofluidic chips with controllable channel size and spacing. Lab on a Chip, 16(19), 3767-3776.

Piegari, A., & Flory, F. (2018). Optical thin films and coatings: From materials to applications: Woodhead Publishing.

Ren, K., Zhou, J., & Wu, H. (2013). Materials for microfluidic chip fabrication. Accounts of chemical research, 46(11), 2396-2406.

Smith, H. I. (1974). Fabrication techniques for surface-acoustic-wave and thin-film optical devices. Proceedings of the IEEE, 62(10), 1361-1387.

Sohrabi, M., Tehrani, D., Danesh, A., & Henderson, G. (2001). Visualisation of oil recovery by water alternating gas (WAG) injection using high pressure micromodels-oil-wet & mixed-wet systems. Paper presented at the SPE Annual Technical Conference and Exhibition.

Tripathi, C., Jain, S., Joshi, P., Sood, S., & Kumar, D. (2008). Development of low cost set up for anodic bonding and its characterization.

Wan, J., Tokunaga, T. K., Tsang, C. F., & Bodvarsson, G. S. (1996). Improved glass micromodel methods for studies of flow and transport in fractured porous media. Water Resources Research, 32(7), 1955-1964.

Weaver, G. (1984). PCB contamination in and around New Bedford, Mass. Environmental science & technology, 18(1), 22A-27A.

Weichel, S., De Reus, R., & Lindahl, M. (1998). Silicon-to-silicon wafer bonding using evaporated glass. Sensors and Actuators A: Physical, 70(1-2), 179-184.

Widmann, D. W. (1976). Metallization for integrated circuits using a lift-off technique. IEEE Journal of Solid-State Circuits, 11(4), 466-471.

Wu, M., Xiao, F., Johnson-Paben, R. M., Retterer, S. T., Yin, X., & Neeves, K. B. (2012). Single-and two-phase flow in microfluidic porous media analogs based on Voronoi tessellation. Lab on a Chip, 12(2), 253-261.

Wu, Q., Bai, B., Ma, Y., Ok, J. T., Yin, X., & Neeves, K. (2014). Optic imaging of two-phase- flow behavior in 1D nanoscale channels. Spe Journal, 19(05), 793-802.

Wu, Q., Ok, J. T., Sun, Y., Retterer, S., Neeves, K. B., Yin, X. Ma, Y. (2013). Optic imaging of single and two-phase pressure-driven flows in nano-scale channels. Lab on a Chip, 13(6), 1165-1171.

Xu, K., Liang, T., Zhu, P., Qi, P., Lu, J., Huh, C., & Balhoff, M. (2017). A 2.5-D glass micromodel for investigation of multi-phase flow in porous media. Lab on a Chip, 17(4), 640-646.

Xu, K., Zhu, P., Colon, T., Huh, C., & Balhoff, M. (2017). A microfluidic investigation of the synergistic effect of nanoparticles and surfactants in macro-emulsion-based enhanced oil recovery. Spe Journal, 22(02), 459-469.

Yun, W., Ross, C. M., Roman, S., & Kovscek, A. R. (2017). Creation of a dual-porosity and dual-depth micromodel for the study of multiphase flow in complex porous media. Lab on a Chip, 17(8), 1462-1474.

III. DIRECT PORE-LEVEL OBSERVATION AND VERIFICATION OF IN- SITU OIL-IN-WATER PICKERING EMULSIFICATION DURING POLYMERIC NANOGEL FLOODING FOR ENHANCED OIL RECOVERY IN A TRANSPARENT THREE-DIMENSIONAL POROUS MEDIUM

ABSTRACT

Different from inorganic nanoparticles, nano-sized crosslinked polymeric nanoparticles (nanogels) has been proved to generate more stable Pickering emulsions under harsh conditions long-termly owing to its inherent high hydrophilicity and surface energy. It has been found both in core-scale or pore-scale that the in-situ emulsions could be formed during the nanofluid flooding process for an enhanced oil recovery (EOR) process. Due to the limitation for direct visualization in core-scale or deficient pore geometries built by two-dimensional micromodels, the in-situ emulsification by nanofluids and emulsion transportation are still not being well understood. In this work, we used three-dimensional transparent micromodel to directly visualize the in-situ emulsification during nanogel flooding process for EOR after water flooding. By synthesizing the nanogel with fluorescent dye, we found the nanogels adsorbed on the whole oil-water interface to lower the total interfacial energy and emulsify the large oil droplets into small Pickering oil-in-water emulsions. A potential mechanism for in-situ emulsification by nanogels was proposed and discussed. After nanogel flooding, the emulsions trapped in the pore throats and those in the effluents were all found encapsulated by the nanogels. The remaining oil droplets sphericity and diameter changes after nanogel flooding under different flow rates are quantitatively compared and analyzed using grouped boxplots. We concluded that the

in-situ emulsification phenomenon would happen during nanogel injection due to the interfacial tension reduction, which could help increase the oil recoveries as an EOR method under different flow rates and pore geometries.

1. INTRODUCTION

As the fossil energy remains one of the most essential global resources, the demand for oil and natural gas resources is still urgently rising in next few decades (Pan et al., 2020; Ramasamy & Amanullah, 2020; ShamsiJazeyi et al., 2014). It is well-known that there is still much oil, about 60%-70%, left in subsurface after primary and secondary recovery trapped by capillary force (Green & Willhite, 1998). Therefore, different enhanced oil recovery (EOR) methods, such as thermal, miscible and chemical methods were then applied to extract 30%-60% more oil from the reservoir (Thomas, 2008). Nevertheless, new technologies were still inevitably to develop due to the high demand of the energy. Nanoparticles (NPs) have been very attractive to be studied and applied in many areas such as civil engineering(Ganesh, 2012), medical applications(Kubik et al., 2005; Kumari et al., 2010; Liong et al., 2008; Soppimath et al., 2001), food science(Duncan, 2011) and solar cells(Saunders & Turner, 2008). Recently, it also appeared to be successful alternatives for improving different engineering processes in the oil and gas industry, including reservoir characterization(Rahmani et al., 2015), reservoir management(Turkenburg et al., 2012), drilling(Hoelscher et al., 2012; J. Zhang et al., 2015) and completion process(Mohammadizadeh et al., 2014). Besides, injection of nanoparticles in the form of nanodispersions were also caught attention of being used as an potential enhanced oil

recovery method due to its small size (1-100 nm) and many other promising interfacial properties(Alomair et al., 2015; Bennetzen & Mogensen, 2014; Cheraghian & Hendraningrat, 2016; Hashemi et al., 2014; Hendraningrat & Torsaeter, 2014). Currently, it is widely accepted that the NPs could adsorb onto two miscible fluid interface(Bhattacharya & Basu, 2013; Du et al., 2010; C. Tian et al., 2018), which helps recover more oil by reducing the interfacial tension (IFT)(Cheraghian & Hendraningrat, 2016; Du et al., 2010; X. Li et al., 2014; Saigal et al., 2013), altering wettability(Cao et al., 2017; S. Li et al., 2019; Roustaei, 2014), modifying disjoining pressure(Alex Nikolov et al., 2010; AD Nikolov & Wasan, 2003) and stabilizing Pickering emulsions(Shen & Ye, 2011; Son et al., 2014; T. Zhang et al., 2010). However, the mechanisms of nanoparticles for enhanced oil recovery are still not well understood so that field applications were not widely applied and remained mostly based on laboratory core flooding research (Agista et al., 2018; Ding et al., 2019; Hendraningrat et al., 2013; Kanj et al., 2011).

Among the suggested mechanisms of NPs for EOR, oil-in-water Pickering emulsion generation and stabilization by NPs have been increasingly researched in recent years due to its better resistance under harsh conditions than surfactants and can be injected for improved mobility control at high salinity condition(I. Kim et al., 2017; T. Zhang et al., 2010). However, most of current used NPs are inorganic NPs and can be tailor-made for specific surface modifications with grafted polymer chains, without which the stable Pickering emulsion with high resistance to harsh conditions cannot be formed(Saha et al., 2018; ShamsiJazeyi et al., 2014; S. Tian et al., 2020; Zhou et al., 2020; Zhou et al., 2019). These modifications significantly raised the budget and increased production time. Except for polymer grafted NPs, another choice is the hybrid polymer nanofluid suspension by

direct mixing or blending nanoparticles into the polymer. Although it was reported easily synthesized, it is hard to obtain a uniform dispersion due to the strong tendency of nanoparticle aggregation in polymer matrix (Gbadamosi et al., 2018).

Compared to Pickering emulsion stabilized by rigid NPs, the soft nanogel stabilized Pickering emulsions have gained much attention due to their temperature and pH-responsive properties (Geng et al., 2019). When adsorbing onto oil-water interface, their inherent high hydrophilicity, sufficient steric repulsion can prevent coalescence of oil droplets, which enables the long-term stabilization of Pickering emulsions, even in high temperatures (Destribats et al., 2011; Geng, Pu, et al., 2018). Other than injecting prepared micro/nano emulsions or NP-stabilized surfactant or foam injections for EOR (Almahfood & Bai, 2018), it was also observed that the solely nanogel dispersion injection after water flooding in a sandstone could generate in-situ shear-induced oil-in- water emulsion as the produced effluent after water flooding was in bulk oil phase while in oil-in-water emulsion state after nanogel flooding. The adsorbed nanogel layer ensured the emulsified oil droplets were stable and isolated before being produced to the surface (Geng, Ding, et al., 2018).

Due to the difficulty of direct visualization of the fluid flow process within a core, the in-situ emulsification phenomenon during nanogel flooding cannot be easily visualized (Qin et al., 2020). Therefore, microfluidic models have become a powerful tool to investigate the microscopic mechanisms of NPs for EOR, including the in-situ emulsification (S. Li et al., 2013). Since most available microfluidic research were based on a 2D micromodel that is inherently difficult to study emulsion or foam flow due to the limited pore geometry(Conn et al., 2014; Y. Zhang et al., 2019), most of which focused only on the investigations of IFT reduction and wettability alteration caused by

NPs(Cheraghian et al., 2017; Nguyen et al., 2014a; Tajik et al., 2018; K. Xu et al., 2015) while few discussed the NP stabilized emulsion flow using emulsion generator or 2.5D micromodel(K. Xu et al., 2018; K. Xu, Liang, et al., 2017; K. Xu et al., 2015; Yang et al., 2020). The most recent 3D transparent micromodel packed with glass beads were only used to direct visualize the two-phase fluids flow behaviors and a core-shell nanohydrogel for conformance control under a confocal microscope(Datta, Dupin, et al., 2014; do Nascimento et al., 2019; Krummel et al., 2013; L. Zhang et al., 2020). To our best knowledge, no research has been done to direct visualize the in-situ emulsification during nanogel flooding using a 3D micromodel, which is a more proper candidate to study the emulsification mechanism with more realistic discontinuous pore throats and pore bodies.

Therefore, in this work, we investigated the in-situ emulsification of remaining oil brought about by solely fluorescent polymeric nanogel flooding for enhanced oil recovery using a 3D transparent porous media with local heterogeneities. How the in-situ emulsions generated during the nanogel flooding and how the shape and size changed of remaining oil before and after nanogel flooding were visualized and studied. The following contents were mainly divided into two sections. We first introduced the synthesis of the fluorescent nanogels and described the prepared fluids properties. Then, we presented the micromodel characteristics and our detailed experimental procedures. Followed are the results and the discussions to demonstrate our findings. Quantitative analyses were given to prove the in-situ emulsification phenomenon during the nanogel flooding.

2. EXPERIMENTAL SECTION

2.1. MATERIALS

Acrylamide was purchased from Xinwantong company (Daqing, China). Acryloxyethyl thiocarbamoyl Rhodamine B (95-100%) was purchased from Polysciences, Inc. N,N'-methylenebisacrylamide (MBAA, 99%) was purchased from Sigma-Aldrich. Ammonium persulfate (98%) was purchased from ACROS ORGANICS. N-decane (99%) was purchased from Alfa Aesar. Deionized water was prepared in the laboratory using an ultrapure water system. Sorbitan monooleate was purchased from Alfa Aesar. Polyethylene glycol sorbitan monostearate was purchased from Sigma-Aldrich.

2.2. SYNTHEIS OF FLUORESCENT POLYACRYLAMIDE NANOGELS

The fluorescent polyacrylamide nanogels were synthesized using a reverse suspension polymerization. The synthesis process was shown in Figure 1. For a typical experiment, 15 g of acrylamide, 20 mg of acryloxyethyl thiocarbamoyl Rhodamine B, and 2.25 mg of MBAA were dissolved in xx g deionized water. Then, the aqueous solution was added into the mixture of 7 g of Span 80, 3 g of Tween 60, and 40 g of decane. After purging nitrogen for 15 min, a 2 mL of 2% APS aqueous solution was added to initiate the polymerization. The reaction was kept at 40 ℃for 2 hours to form nanogels. Afterwards, the nanogels were precipitated in acetone and washed with acetone three times using centrifugation.

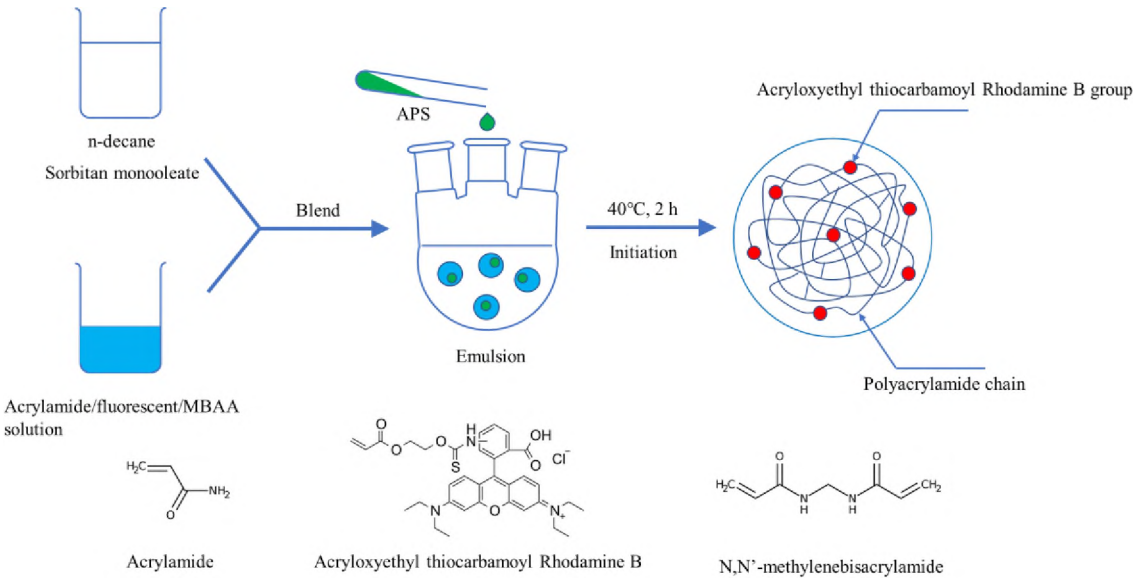

Figure 1. Schematic diagram of the synthesis of the fluorescent dyed cross linked polymeric nanogel

2.3. SIZE AND ZETA POTENTIAL OF THE NANOGELS

The size distribution and zeta potential of the synthesized nanogels were measured using a Malvern ZS90 Nanosizer at a scattering angle of 90° with an incident beam of a wavelength at 633 nm at 30 °C. The prepared nanofluid was directly injected into the glass cuvette and folded capillary zeta cell for size and zeta potential measurements, respectively. The intensity size distribution was obtained from analysis of the correlation functions using the multiple narrow mode algorithms in the instrument software, which repeated three times for the same sample fluid. The final size distribution of the nanogel dispersion fluid was shown in Figure 2a, where the distribution range is from 150 nm to 1000 nm and the peak of the nanogel distribution falls between the range of 250-300 nm. For the zeta potential shown in Figure 2b, it appeared in the range of around -1 to -5 mV, which can be regarded as neutral charged nanogels. It has been studied that neutral charged nanogels exhibited the highest and longest performance on stabilizing the oil-in-water

Pickering emulsions (Geng, Pu, et al., 2018). Even the absolute value of zeta potential is very low, this crosslinked high molecular nanogel could still be stable by providing the steric hinderence(Bizmark, Ioannidis, & Henneke, 2014). Besides, the lightly negative surface charge could minimize the adsorption of the nanogels onto the glass beads, which acquires also a negative surface charge in water (Behrens & Grier, 2001), to reduce the factor that may affect the emulsification process (Johnson & Lenhoff, 1996).

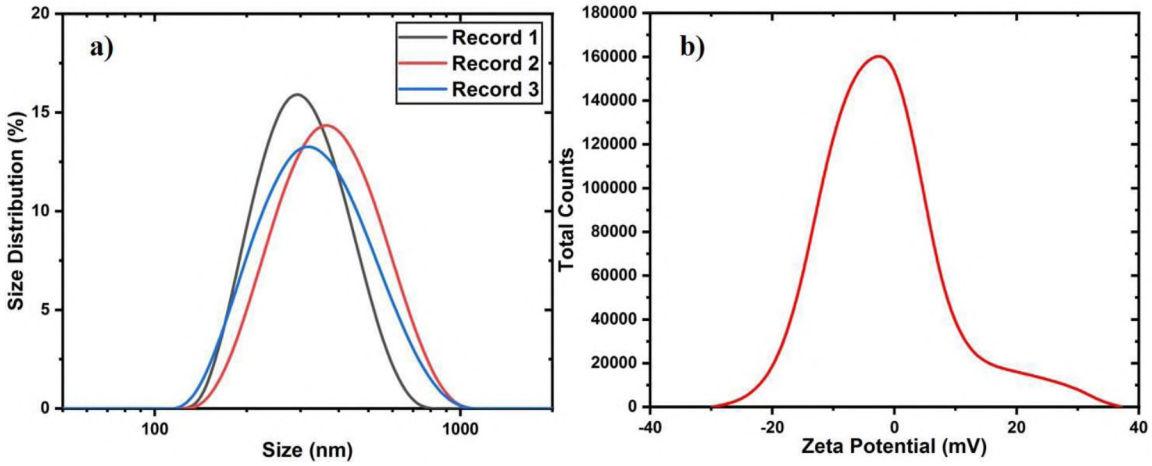

Figure 2. Characteristics of fluorescent dyed nanogel. a) Particle size distribution based on the DLS method. b) Zeta potential distribution

2.4. MICROMODEL CHARACTERISTICS AND FLUID PREPARATION

We fabricated the 3D transparent porous media by lightly sintering the borosilicate glass beads (Mo-Sci) densely packed in a squared quartz capillary tube (L:2 cm; W:0.5 mm; H: 0.5mm;T: 0.25mm; Technical Glass Products, Inc.) under 850 Celsius degree for 100s. The capillary tube was packed with two sizes of glass beads (small to big ratio of 3:1) with the radii of r=17 and 65 μm to mimic the porous media with micro- heterogeneities. The pore diameters are estimated between 5 to 21 μm (Thompson et al., 2008). Due to the

random packing, the pore geometries are different for eight models and the average porosity is 42%. The porosity was determined after oil saturation process and would be discussed in following section. The permeability can thus be estimated as 4.1 μm^2 using Kozeny-Carman relation, $k= a^2\varphi^3/45\ (1-\varphi)^2$, where a is the average sphere radius, φ is the average porosity. To overcome the limitations that scattering lights from interfaces of fluid/fluid and fluid/solid would preclude the direct observation of the multiphase flow within the 3D porous medium, an immersion aqueous liquid (Cargille Labs; ρ=1.921 g/cc; μ=7.684 cP) and immersion oil (Cargille Labs; ρ=0.855 g/cc; μ=18.81 cP) were used as the wetting phase and the non-wetting phase to keep the refractive index the same as the quartz capillary tube and glass beads with RI=1.47. The interfacial tension between two fluids is σ=12mN/m measured by using pendant drop method. The nanofluid was then prepared by adding 0.2 g of fluorescent polyacrylamide nanogels into the 100 mL of immersion aqueous liquid where the concentration of nanogels was controlled as low as 2 wt.% , which would not significantly increase the wetting phase viscosity(Metin, Bonnecaze, & Nguyen, 2013). To ensure the nanogels were in fully swollen state, the prepared nanofluid was stirred for 1 h and then stored at 65 ℃ for 24 h before any characterization and experiments. To distinguish the two kinds of fluids and nanogels under different lasers, they were all fluorescent dyed differently. Alexa Flour 647 for the water phase, Nile Red for the oil phase (Sigma-Aldrich) and Methacryloxyethyl thiocarbamoyl rhodamine B (Poly-sciences) for nanogels, respectively. The water phase was in blue, the oil was in green and nanogels were in red after separately excited by lasers at 488, 561 and 647 nm.

2.5. EXPERIMENTAL SET-UP AND PROCEDURE

To visualize the dynamic fluid flow inside the micromodel, we mounted each micromodel on a Nikon A1R HD inverted confocal laser-scanning microscope (Eclipse Ti2) as shown in Figure 3 for the schematic of the experimental set-up. A syringe pump (Harvard Apparatus PHD ULTRATM) was used to inject the fluids at the inlet of the model through a fused silica capillary tubing with a 100 μm inner diameter and the effluent was collected at the outlet. We used two modes of visualization for each experiment, one is the static global mode and the other is the dynamic local mode. The static global mode was used after oil saturation, water flooding and nanogel flooding to reveal the final fluid phase distribution at each end of the flooding process. We used 20 X objective lens to scan the middle regions of the model to avoid the tubing influences at the inlet and the outlet where the beads were not being compactly packed. The stage was set moved automatically from left corner inlet to the right corner outlet with 13 horizontal steps (7.62mm) along x direction, 2 vertical steps (0.6mm) along y direction and 200 μm in depth along z direction constructed from 40 optical slices spaced by 5 μm. All fields were then stitched together (5% overlap) to obtain a complete 3D image of the model. The dynamic local mode was used to study the zoomed-in displacement process within the porous media in which the region of interest was chosen at the middle of the model. We scanned and recorded the whole injecting process during water and nanogel flooding using resonant scanning mirrors instead of traditional galvanometer mirrors to acquire high scanning speed. Each 3D acquisition was constructed with 20 optical slices in a 0.6mm*0.6mm x-y plane and spaced by 10 μm along z -direction with total of 200 μm in depth along z-direction. Although the resolution became worse when using resonant scanner, the fast acquisition

time for an entire 3D acquisition was approximately 14 seconds, which enables the visualization of the fluid flow details. All experiments were conducted at room temperature.

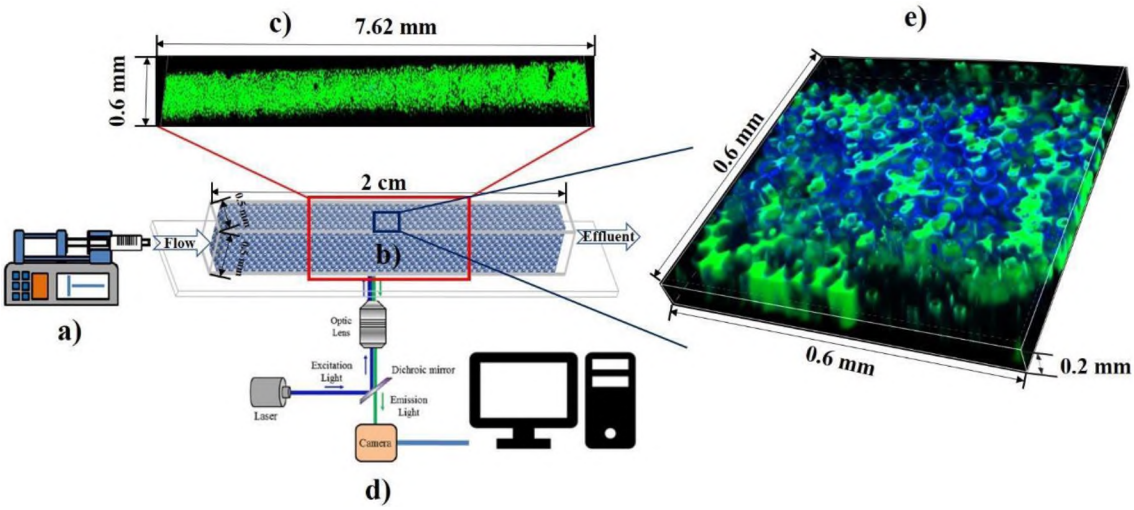

Figure 3. Schematic of experimental set-up. a) syringe pump for injection of fluids. b) the transparent porous media built by packed glass beads. c) an example of static global visualization of an oil saturated model. d) the confocal laser scanning microscope system for visualizing the fluid flow process inside the model. e) an example of the dynamic local visualization of a 3D acquisition during the water flooding. (oil in green and water in blue)

2.6. OIL SATURATION PROCESS

In this research, since our focus is to observe the fluorescent nanogels effect on emulsifying the remaining oil droplets after water flooding, we did not consider the irreducible water saturation to mimic the real reservoir saturation history. Therefore, we directly saturated the model with oil first and then followed by water flooding and nanogel flooding. The micromodel was firstly saturated with the immersion oil injected by using syringe pump (Harvard Apparatus, model 88-3015) for 24 hrs. at the flow rate of 0.005mL/hr through a fused silica capillary tubing with a 100 μm inner diameter. The flow

direction was from left inlet to the right outlet where was always open to the air with no backpressure added. As shown in Figure 4a, the 3D porous medium was fully saturated with the green oil phase. Since the oil occupied all the pore volume, we then use the saturated oil volume to determine the effective porosity as $\phi=Vv/Vt=Vo/Vt$, where Vv is the volume of pore spaces, Vo is the volume of the saturated oil in pore spaces and Vt is the total volume which includes the pore spaces and the glass beads. The total volume is $5.115*10^8$ μm^2 , calculated by multiplying the visualized area and the height. We only chose the middle part of the model to visualize to avoid the tubing influences at the inlet and the outlet where the beads are not being packed compactly. However, the outlet region with tubing inserted can be used to verify the assumption for the interface conditions governing the coupled flow in a dual-porosity medium and its adjacent conduits as the two different sized glass beads and the void spaces between the tubing and the tube wall can be regarded as the dual-porosity medium and the conduits, respectively (Hou et al., 2016).

2.7. WATER AND NANOGEL FLOODING PROCESS

We conducted the forced water imbibition processes after oil saturation with different constant flow rates of 0.002, 0.02, 0.04, 0.06, 0.08, 0.1, 0.8, 20 mL/hr, spanning the capillary number, which is defined as $Ca=\mu_{nw}Q_{inj}/A\sigma$ (where μ_{nw} is the injection fluid viscosity, Q_{inj} is the injection rate, A is the cross-section area of the micromodel, σ is the interfacial tension between the wetting and non-wetting fluids), from 10^{-6} to 10^{-2}. To better show the flooding performances, we here chose one representative 2D layer of water flooding under 0.8mL/hr as an example shown in Figure 4b. The oil phase and water phase were in color of green and blue, respectively. All flooding processes were stopped after 10

PV (pore volume) of injection when no more significant phase changes within the models. The later chased nanogel floodings were also conducted using the same flow rates and PVs. As shown in Figure 4c, the nanogel suspension fluid was in red with dispersed fluorescent dyed nanogels. After finishing all the experiments, we used NIS Elements software to binarized and segmented the water, oil and nanogel fluid and do the quantitative analysis. Detailed results and discussions were presented in next section.

3. RESULTS AND DISCUSSION

3.1. IN-SITU EMULSIFICATION

The in-situ emulsification process and results were observed during and after nanogel flooding using two modes of visualization. We found that for all experiments under different flow rates, the number of remaining oil droplets increased after nanogel flooding while the total remaining oil volume decreased. As shown in Figure 5a, it does not show a clear relationship between different flow rates and remaining oil droplets volume due to the random packed porous geometries of different micromodels.

However, it does show that the remaining oil droplet volumes after nanogel flooding are less than those of after water flooding under each flow rate. For the remaining oil droplet numbers as shown in Figure 5b, it shows a decrease from lowest to highest flow rate for both after water and nanogel flooding. Besides, the numbers of remaining oil droplets after nanogel flooding are always more than those of after water flooding for all cases. Shown in Figure 5c and d are the representative cases of the final remaining oil droplets distribution after water flooding and nanogel flooding under the flow rate of

0.8mL/hr. We only included the green color for oil only to eliminate other interference. It is obvious that, especially in the red circle, the bigger remaining oil droplets after water flooding became smaller oil droplets after nanogel flooding.

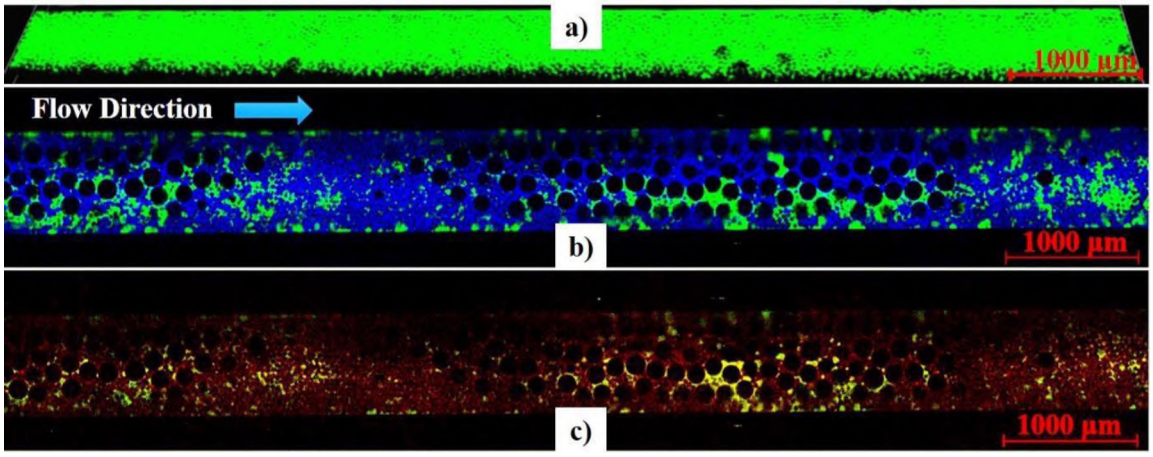

Figure 4. Static global visualization examples after a) oil saturation. b) water flooding process. c) nanogel flooding process. (oil in green, water in blue and nanofluid in red)

An in-situ emulsification process in a local region under the flow rate of 20 mL/hr was shown in Figure 6a to Figure 6f. At T=0, the remaining oil after water flooding was distributed as connected large clusters and the nanogel fluid was about to enter this region. At T=14s, most of the bulk remaining oil was emulsified and displaced while there were still some oil droplets trapped in the pores. From T=14s to T=70s, we observed that the emulsified oil droplets were still being displaced within the pore throats, but some emulsions were left and trapped in the end which cannot be recovered. Especially for the middle group of oil droplets which were easily being displaced through the pore space between two bigger glass beads from T=14s to T=42s in figure to figure, they began to snap-off when they went through the thinner pore throats consisted of smaller glass beads

from T=42s to T=70s in figure to figure. Finally, at T=70s, there were no more emulsions moving in the whole region and some emulsions that cannot be displaced under current scenario were trapped as residual oil-in-water emulsion droplets.

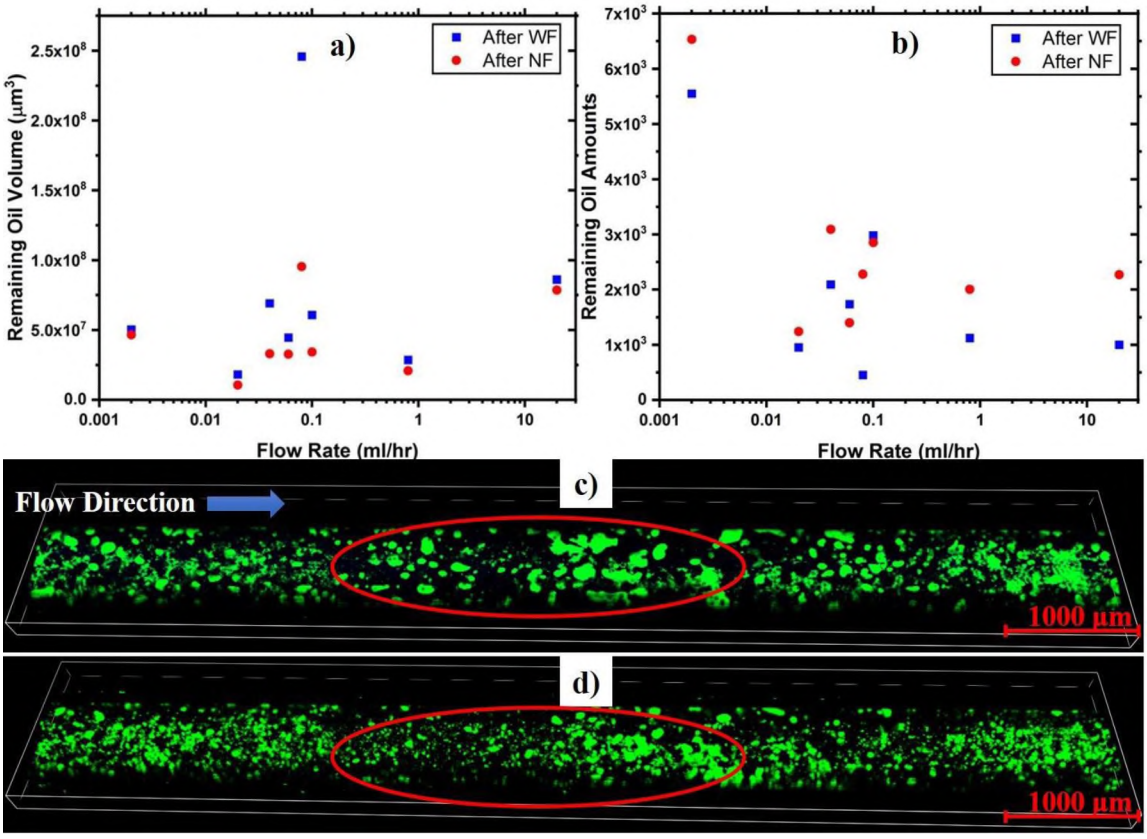

Figure 5. The a) remaining oil volume and b) remaining oil amounts under different flow rates after water and nanogel flooding and the remaining oil distribution after c) water flooding and d) nanogel flooding under flow rate of 0.8 mL/hr. (oil in green)

We collected a small amount of effluent after nanogel flooding and visualized within a local region. As shown in Figure 6g, the 2D view on the left shows all the emulsions are in perfect round shapes and the sizes of the emulsions were mostly from about 2 to 20 μm in diameter. However, we found the minimum trapped oil droplet diameter is around 6 μm, which closes to the minimum pore size of 5 μm.

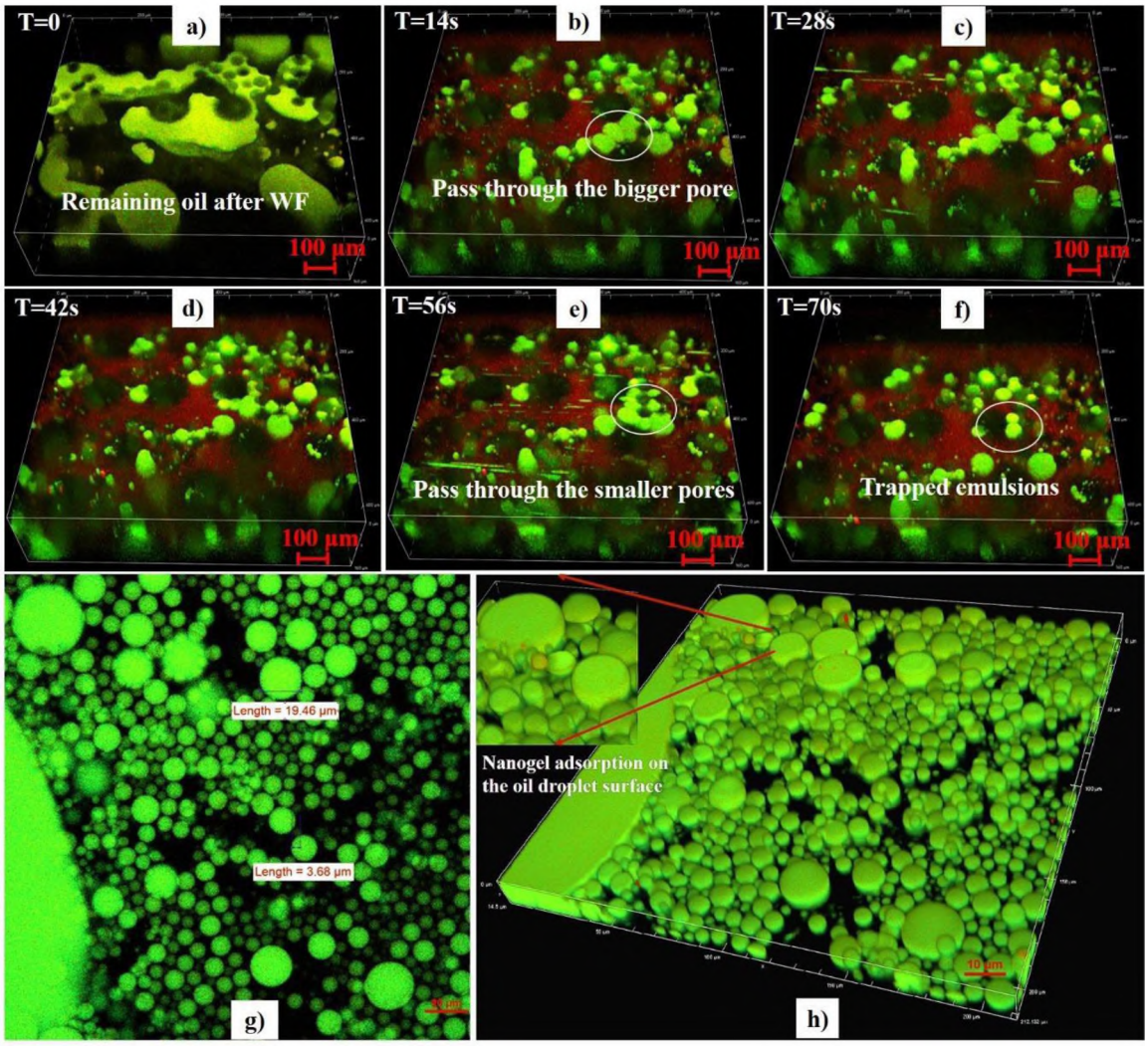

Figure 6. a) to f) An in-situ emulsification process example in a local region under the flow rate of 20 mL/hr and the emulsion droplets in the effluents in a g) 2D and h) 3D view, showing the diameters of the displaced emulsions were around 2-20 µm and the adsorbed red nanogels on the interface. (oil in green and nanogel/fluid in red)

It indicated that the emulsified oil droplets that smaller than the pore throat were displaced out of the model completely as the continuous phase. From the 3D view on the right in Figure 6h, we found it clearer that the red nanogels were absorbed on the droplet sphere surface, although the sizes were small and the signal intensities were not as strong as the microgels which are much easier to be detected (Kwok & Ngai, 2016). The video in

supportive files showed the local water flooding process and nanogel flooding process, where one could observe the clear emulsification process during nanogel flooding to displace more remaining oil droplets out of the porous media.

However, not all remaining trapped oil droplets after water flooding can be emulsified and displaced during the nanogel flooding process although it was stated snap-off would happen at higher capillary numbers if the pore size is much smaller than the droplet size (Soo & Radke, 1984).

Figure 7a to Figure 7f displayed an unsuccessful emulsification process for a trapped remaining oil droplet after water flooding under the capillary number of 10-2. At T=0, the original droplet was trapped in the pore space between the glass beads. From T=16s, we observed that the red nanogels adsorbed onto the front meniscus of the droplet and started to emulsify and drag the droplet. The droplet deformation reached the maximum at T=57s but back to original shape at T=71s. Then the second emulsification attempt occurred at T=114s when the droplet was once again dragged into the pore throat. Finally, as the droplet failed to be emulsified, it changed back to the original shape for the second time at T=268 and no further deformation was observed. The final shape of the droplet was shown to have larger surface area than the initial form which indicated a sphericity decrease. Besides, more nanogels were shown adsorbed on the front meniscus, which indicated that the nanogels could be trapped together with the droplet at the entrance of the pore throat and kept it a stabilized oil-in-water emulsion droplet. This finding is consistent with the Lattice Boltzmann simulation result(Fu, Zhao, Bai, Jin, & Cheng, 2016), which showed the viscous shear force was supplied by the outer fluid (nanofluid in our experiments) against the interfacial tension when flows pass the oil droplet that caused the

droplet snap-off near the pore throat exit. The unsuccessful emulsification would lead to the capillary trapping of the residual oil droplets shown in figure, which were also regarded as the trapped oil-in-water emulsion droplets. The trapped emulsion droplet may play a role for in-depth diversion agent for conformance control (Rezaei & Firoozabadi, 2014). As shown in Figure 4b, the low permeability region s of small glass beads were barely swept but it turned red after nanogel flooding in Figure 4c, indicating the bigger pores consist of bigger glass beads have been clogged by the trapped oil-in-water emulsions. As we expected, the residual oil droplets were in low sphericity and the nanogels were mostly found on the front meniscus of the droplets with the flow direction from left to right.

3.2. REMAINING OIL DROPLETS CHARACTERIZATIONS

Sphericity of an oil droplet defined as $\psi=(6\pi^{1/2}Vp)^{2/3}$ (where Vp and Ap are the droplet volume and surface area, respectively), is a measure of a how spherical an oil droplet is. By definition, the more the shape of an oil droplet close to a sphere, the more spherical it is as the sphericity is closer to ψ =1. Oppositely, non-spherical oil droplets always have the sphericity less than ψ =1 and close to ψ =0 when they are having larger volumes and surface areas that the shapes are far from spherical. To compare the sphericity after water flooding and nanogel flooding under different capillary numbers, we plotted the grouped box plot to give an intuitive comparison as shown in Figure 9a. Interestingly, we found the mean sphericity of the remaining oil droplets after nanogel flooding decreased compared to water flooding in five out of eight experiments, which were conducted under lower capillary numbers. However, the sphericity of the remaining oil droplets after nanogel flooding increased compared to water flooding for two experiments

under higher capillary numbers. For the smallest capillary number, the sphericity did not show much change but a slight increase. The reason to cause the remaining oil droplet sphericity difference after water and nanogel flooding mainly due to the oil/water interfacial tension reduced by nanogel adsorption (M. Liu et al., 2015). The adsorption on the oil/water interface may also change the oil droplet surface wettability, which would lead to the sphericity reduce of the trapped remaining oil droplets after water flooding. We therefore raised a discussion for how this wettability change induced sphericity reduce in the porous media based on our direct observation using confocal microscope. The suggested sphericity changing process for a trapped remaining oil droplet by nanogel adsorption is shown in Figure 8c. Originally, a hydrophobic remaining oil droplet was trapped in a pore throat due to the capillary pressure after water flooding. The hydrophilicity of the glass bead made the contact angle between the oil droplet and the glass bead very large (over 100 degree) so that the trapped oil droplet remained very spherical shape of high sphericity close to ψ =1. As the later chased nanogel fluid flew towards the oil droplet, they climbed immediately onto the oil/water interface and encapsulated the whole droplet, which was very similar to the climbing of recent reported Janus amphiphilic nanosheets climbing onto the oil-water interface (Luo et al., 2016). An oil droplet sphericity change example after water and nanogel flooding were shown in Figure 8a and b. It is obvious that the sphericity decreased after nanogel flooding that the droplets became non-spherical (droplets were highlighted for better segmentation). Even though we were unable to capture this climbing process due to the limitation of the frame rate, we found the trapped oil droplets after nanogel flooding were all encapsulated completely by red nanogels as shown in Figure 7g and also the displaced emulsion droplets

in Figure 6g and h. Therefore, it indicated that the nanogels can climb into the gap between the oil droplet and the glass bead to form a thin nanogel layer.

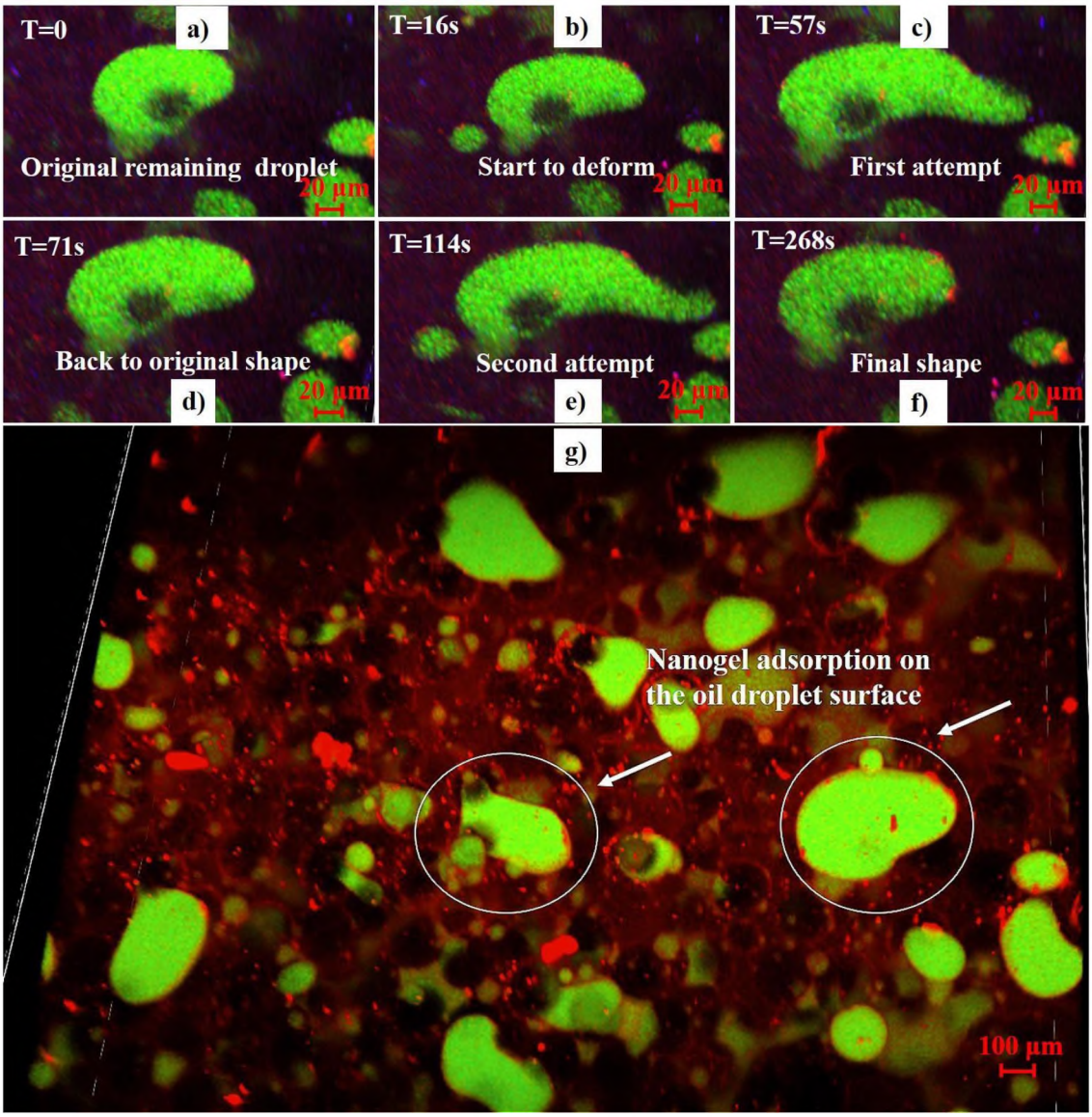

Figure 7. a) to f) An unsuccessful in-situ emulsification process example for a large trapped oil droplet in a local region under the flow rate of 20 mL/hr. g) the trapped emulsions in the porous media were encapsulated by the adsorbed red nanogels with mostly on droplet front meniscus. (oil in green and nanogel/fluid in red)

Since the glass bead and the nanogel were both hydrophilic, the contact angle between the oil droplet with adsorbed nanogels and the glass beads became smaller as the nanogel thin layer tends to spread along the glass bead. As a result, the shape of the oil droplet became less spherical due to the nanogel adsorption and climbing. At the meantime, part of the oil droplet was emulsified by the passing flow into micro-sized oil-in-water emulsions that cannot be trapped. If the emulsion droplet size is very small compared with the pore and throat diameters of a porous media, the emulsion can be regarded as a continuous phase. As shown in Figure 8a, the remaining oil droplets exhibited high sphericity after water flooding while decreased a lot after nanogel flooding as shown in Figure 8b where the shapes became more irregular, meanwhile proving the interfacial tension was decreased due to the nanogel adsorption.

However, sphericity of the oil droplets after nanogel flooding increased when flow rates became higher. As shown from the grouped boxplots Figure 9a, when the flow rates were at 0.8mL/hr and 20mL/hr, the sphericity of the oil droplets after nanogel flooding increased. It indicated that higher flow rate could induce higher shear rate, under which the bigger residual oil droplets at the model boundary could be emulsified into more small oil droplets. The total volume and the surface area of the residual oil droplets both decreased a lot, hence the sphericity increased thereafter. At lower flow rates, the bigger residual oil droplets stuck to the boundary were not likely to be emulsified and displaced, thus the sphericity was still decreased even the residual oil droplets in porous media decreased since the total volume were not decreased a lot but the surface area increased a lot. The equivalent diameters of the remaining droplets under different flow rates were also displayed in a grouped boxplot as shown in Figure 9b. At lower flow rates, the diameters of the oil

droplets did not change very much as the driving force was not enough to move large amount of oil.

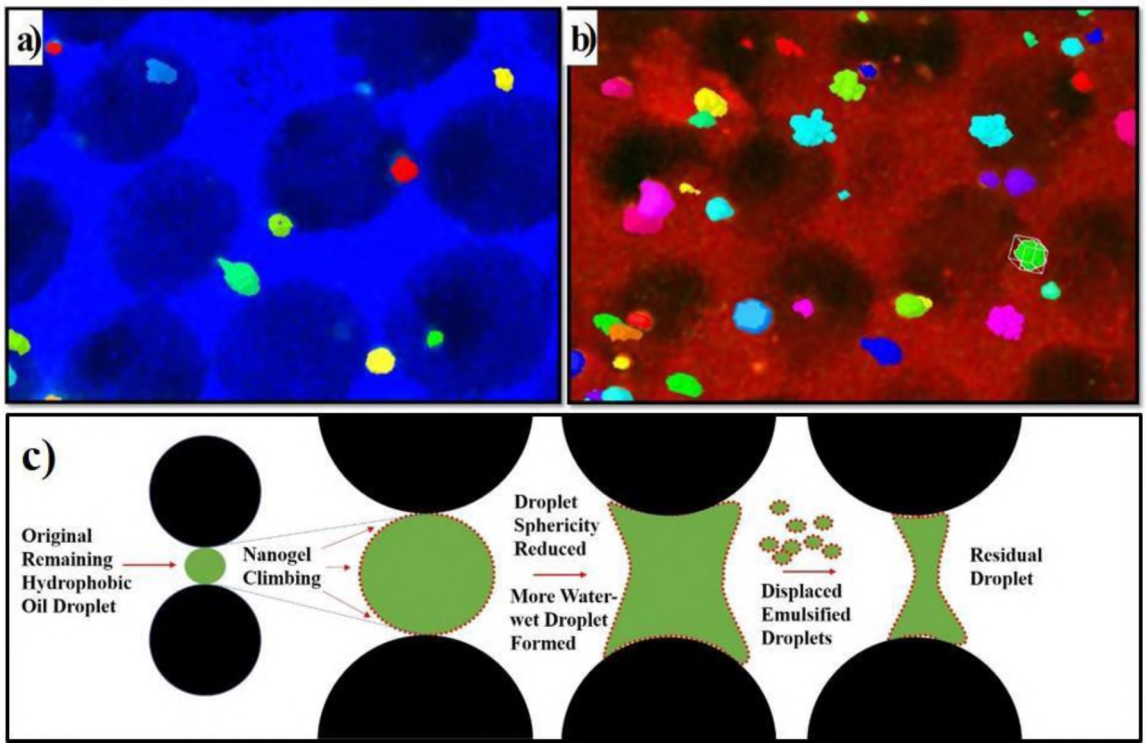

Figure 8. The remaining oil droplets sphericity after a) water and b) nanogel flooding. (all droplets were highlighted in colors for better segmentation purpose). c) suggested mechanism emulsification process of remaining oil droplets by nanogel in a pore throat

However, as the flow rates became higher, the oil droplet diameters increased as the pressure gradient became higher to emulsify more remaining oil, which caused some bigger emulsion droplets trapped in the porous media. It showed that the emulsion flow during nanogel flooding was not sensitive at flow rates but became unstable at higher flow rates(Soo & Radke, 1984), which is also consistent with recent study of pore-scale emulsion flow in porous media(Yazhou, Demin, Zhipeng, & Rui, 2017).

Figure 9c to Figure 9j displays the relationship between the remaining oil droplets volume and the sphericity after water and nanogel flooding under different flow rates. These figures first give an intuitive visualization that the red dots that are remaining oil droplets after nanogel flooding are more than the blue dots that are remaining oil droplets after water flooding. Besides, we found the sphericity of a trapped oil droplet decreases as its volume increases under each flow rate, indicating that a larger oil droplet has a relatively higher surface area compared to its volume. For an oil droplet with volume larger than 0.001 mm^3, the sphericity is smaller than $\psi<0.2$. This kind of larger remaining oil cluster was often found stuck to the tube walls which are less water wet and in flat sheet-like shape far from spherical, which could hardly being emulsified and displaced at low flow rates and almost remained the same volume after nanogel flooding.

We found that under high flow rate of 20 mL/hr most of the remaining oil volume after water flooding have low sphericity even the volume is small, indicating they were unswept and trapped due to the viscous fingering. However, the mean sphericity increased after nanogel flooding and it can be found in figure that the oil clusters with low sphericity have been swept and emulsified into small oil droplets with higher sphericity. This observation indicated that nanogel flooding at high flow rates, other than low flow rates, is more likely to improve the micro-heterogeneity of the porous media and emulsify large oil clusters into small oil droplets, resulting in an increase of mean sphericity due to the decrease of the total volume and the surface area.

3.3. ENHANCED OIL RECOVERY

The oil recovery after water flooding, nanogel flooding and total oil recovery under different flow rates were shown in Table 1.

We found that the oil recoveries after water flooding were not simply increased as the capillary number increased due to the disordered packing of the glass beads(Datta, Chiang, Ramakrishnan, & Weitz, 2013), which is inconsistent to the result of homogeneous porous media consists of one-sized glass beads(do Nascimento et al., 2019). Besides, the increased oil recoveries after nanogel flooding were higher when the oil recoveries after water flooding were low. On the contrary, when oil recoveries after water flooding were high, the oil recoveries after followed nanogel floodings were relatively low. As shown in Table 1, the experiment under flow rate of 0.08mL/hr only achieved 34.4% oil recovery after water flooding, which can be regarded as a special case due to the loose packing of the micromodel. However, the total oil recovery increased to 74.5% after nanogel flooding, which is a 40.2% increasement compared to water flooding. When the oil recovery after water flooding was 89.6% under the flow rate of 0.8mL/hr, the increased oil recovery by followed nanogel flooding was only 2.8%.

Therefore, the remaining oil saturation after water flooding may affect the nanogel flooding performance. When the remaining oil saturation is high, most of the trapped oil in the unswept zone was maintained in the form of connected bulk phase. When there were less remaining trapped oil droplets dispersed in separated pores, they were much harder for the nanogel to emulsify and recover due to the increased capillary force even though the nanogels could still help recover small amount of remaining oil droplets by reducing the interfacial tension and emulsification. All in all, no matter under what conditions of the

pore geometries, flow rates or water flooding performances, the nanogels did show oil recovery improvement after water flooding and contribute to the total recovery.

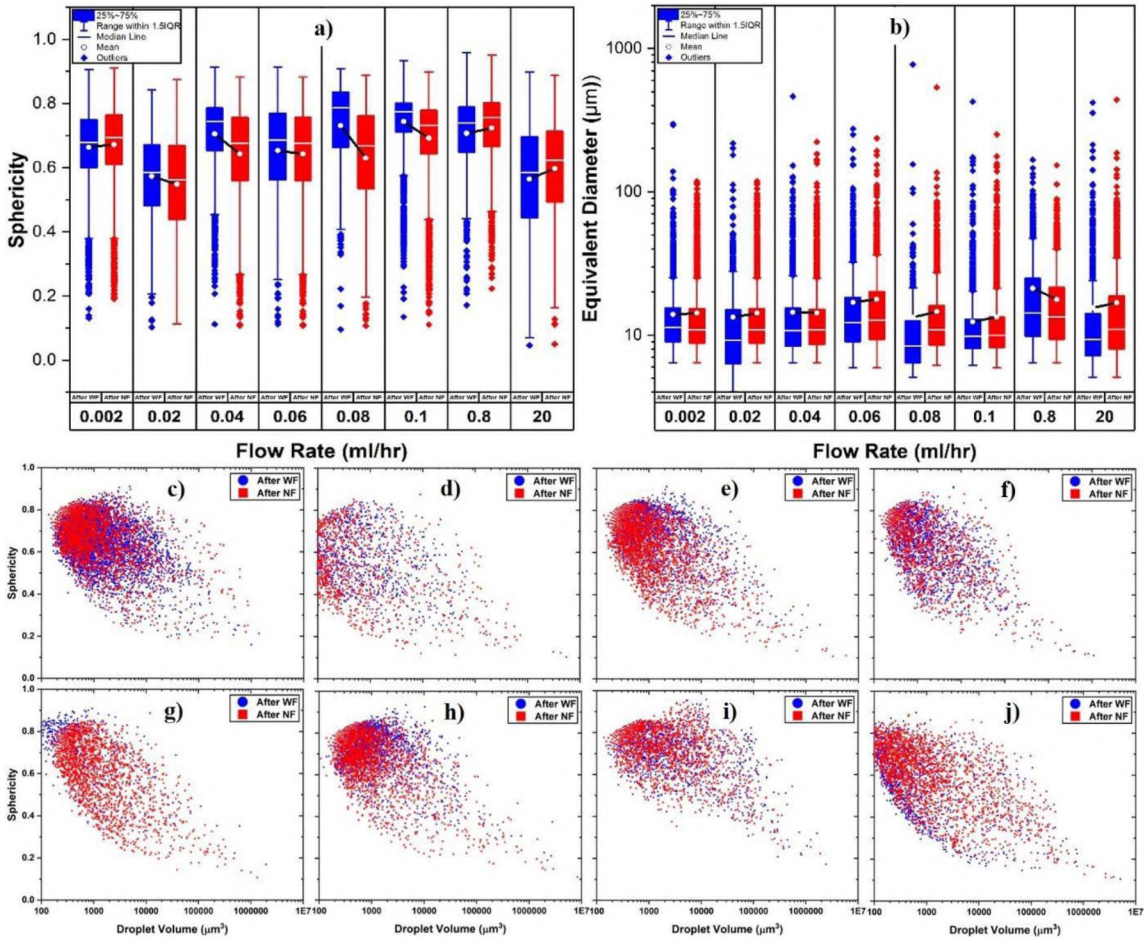

Figure 9. The grouped box plots of a) remaining oil droplets sphericities and b) equivalent diameters after water and nanogel flooding under different flow rates. c) to j) the relationship between the remaining oil droplets sphericity and the volume after water and nanogel flooding under different flow rates from 0.002 to 20 mL/hr

Table 1. Enhanced oil recovery under different flow rates

Flow Rate /ml^hr^{-1}	Capillary Number	Oil Recovery (WF)/%	Oil Recovery (NF)/%	Oil Recovery (Total)/%
0.002	$1.4*10^{-6}$	78.1	1.7	79.7
0.02	$1.4*10^{-5}$	88.2	5.0	93.1
0.04	$2.8*10^{-5}$	76.1	12.5	88.6
0.06	$4.3*10^{-5}$	46.8	14.1	60.9
0.08	$5.7*10^{-5}$	34.4	40.2	74.5
0.1	$7.1*10^{-5}$	82.7	7.6	90.2
0.8	$5.7*10^{-3}$	89.6	2.8	92.4
20	$1.4*10^{-2}$	82.4	1.5	83.9

4. CONCLUSION

To conclude, we successfully synthesized the polymeric nanoparticles with fluorescent dye and directly visualized their roles on emulsifying the remaining oil droplets during the nanogel flooding under different flow rates within a 3D transparent micromodel using the confocal microscope. Under dynamic local visualization mode, we captured the in-situ emulsification process and demonstrated two scenarios. For the successful emulsification scenario, we found the bulk form of remaining oil clusters after water flooding were emulsified by nanogels into small oil droplets and some of the emulsion droplets were trapped in the end of the nanogel flooding. For the unsuccessful one, we found some bigger droplets cannot be displaced and emulsified through the pore throat due to the capillary pressure and the nanogels were found adsorbed on the droplet front meniscus the most. Potential mechanisms for in-situ emulsification by nanogels were proposed and discussed. Under static global mode, we segmented the remaining oil droplets before and after nanogel flooding and their sphericity and diameter changes were compared and analyzed under different flow rates. The oil recovery for each experiment

was shown enhanced by nanogel flooding, proving the feasibility of the nanogel as a potential EOR agent. However, the in-situ emulsion by nanogels for EOR still need further research using the 3D micromodel. The wettability effect on nanogel in-situ emulsification could be investigated by altering the glass beads originally to hydrophobic instead of hydrophilic. Besides, nanogel concentration and the surface charges effect could also be studied for better understanding the in-situ emulsion generation and transportation under different conditions.

REFERENCES

Agista, M. N., Guo, K., & Yu, Z. (2018). A state-of-the-art review of nanoparticles application in petroleum with a focus on enhanced oil recovery. Applied Sciences, 8(6), 871.

Almahfood, M., & Bai, B. (2018). The synergistic effects of nanoparticle-surfactant nanofluids in EOR applications. Journal of petroleum science and engineering, 171, 196-210.

Alomair, O. A., Matar, K. M., & Alsaeed, Y. H. (2015). Experimental study of enhanced-heavy-oil recovery in Berea sandstone cores by use of nanofluids applications. SPE Reservoir Evaluation & Engineering, 18(03), 387-399.

Behrens, S. H., & Grier, D. G. (2001). The charge of glass and silica surfaces. The Journal of Chemical Physics, 115(14), 6716-6721.

Bennetzen, M. V., & Mogensen, K. (2014). Novel applications of nanoparticles for future enhanced oil recovery. Paper presented at the International petroleum technology conference.

Bhattacharya, R., & Basu, J. (2013). Microscopic dynamics of nanoparticle monolayers at air–water interface. Journal of colloid and interface science, 396, 69-74.

Bizmark, N., Ioannidis, M. A., & Henneke, D. E. (2014). Irreversible adsorption-driven assembly of nanoparticles at fluid interfaces revealed by a dynamic surface tension probe. Langmuir, 30(3), 710-717.

Cao, N., Mohammed, M. A., & Babadagli, T. (2017). Wettability alteration of heavy-oil-bitumen-containing carbonates by use of solvents, high-pH solutions, and nano/ionic liquids. SPE Reservoir Evaluation & Engineering, 20(02), 363-371.

Cheraghian, G., & Hendraningrat, L. (2016). A review on applications of nanotechnology in the enhanced oil recovery part A: effects of nanoparticles on interfacial tension. International Nano Letters, 6(2), 129-138.

Cheraghian, G., Kiani, S., Nassar, N. N., Alexander, S., & Barron, A. R. (2017). Silica nanoparticle enhancement in the efficiency of surfactant flooding of heavy oil in a glass micromodel. Industrial & Engineering Chemistry Research, 56(30), 8528-8534.

Conn, C. A., Ma, K., Hirasaki, G. J., & Biswal, S. L. (2014). Visualizing oil displacement with foam in a microfluidic device with permeability contrast. Lab on a Chip, 14(20), 3968-3977.

Datta, S. S., Chiang, H., Ramakrishnan, T., & Weitz, D. A. (2013). Spatial fluctuations of fluid velocities in flow through a three-dimensional porous medium. Physical review letters, 111(6), 064501.

Datta, S. S., Dupin, J.-B., & Weitz, D. A. (2014). Fluid breakup during simultaneous two-phase flow through a three-dimensional porous medium. Physics of Fluids, 26(6), 062004.

Destribats, M., Lapeyre, V., Wolfs, M., Sellier, E., Leal-Calderon, F., Ravaine, V., & Schmitt, V. (2011). Soft microgels as Pickering emulsion stabilisers: role of particle deformability. Soft Matter, 7(17), 7689-7698.

Ding, H., Zhang, N., Zhang, Y., Wei, M., & Bai, B. (2019). Experimental data analysis of nanoparticles for enhanced oil recovery. Industrial & Engineering Chemistry Research, 58(27), 12438-12450.

Do Nascimento, D. F., Junior, J. R. V., Paciornik, S., & Carvalho, M. S. (2019). Pore scale visualization of drainage in 3D porous media by confocal microscopy. Scientific reports, 9(1), 1-11.

Du, K., Glogowski, E., Emrick, T., Russell, T. P., & Dinsmore, A. D. (2010). Adsorption energy of nano-and microparticles at liquid− liquid interfaces. Langmuir, 26(15), 12518-12522.

Duncan, T. V. (2011). Applications of nanotechnology in food packaging and food safety: barrier materials, antimicrobials and sensors. Journal of colloid and interface science, 363(1), 1-24.

Fu, Y., Zhao, S., Bai, L., Jin, Y., & Cheng, Y. (2016). Numerical study of double emulsion formation in microchannels by a ternary Lattice Boltzmann method. Chemical Engineering Science, 146, 126-134.

Ganesh, V. K. (2012). Nanotechnology in civil engineering. European Scientific Journal, 8(27).

Gbadamosi, A. O., Junin, R., Manan, M. A., Yekeen, N., Agi, A., & Oseh, J. O. (2018). Recent advances and prospects in polymeric nanofluids application for enhanced oil recovery. Journal of Industrial and Engineering Chemistry, 66, 1-19.

Geng, J., Ding, H., Han, P., Wu, Y., & Bai, B. (2018). Transportation and potential enhanced oil recovery mechanisms of nanogels in sandstone. Energy & fuels, 32(8), 8358-8365.

Geng, J., Pu, J., Wang, L., & Bai, B. (2018). Surface charge effect of nanogel on emulsification of oil in water for fossil energy recovery. Fuel, 223, 140-148.

Geng, J., Pu, J., Zhao, Y., Lin, B., Bai, B., & Thomas, S. P. (2019). pH-Responsive crude oil- in-water Pickering emulsion stabilized by polyacrylamide nanogels. Fuel, 258, 116159.

Green, D. W., & Willhite, G. P. (1998). Enhanced oil recovery (Vol. 6): Henry L. Doherty Memorial Fund of AIME, Society of Petroleum Engineers ….

Hashemi, R., Nassar, N. N., & Almao, P. P. (2014). Nanoparticle technology for heavy oil in-situ upgrading and recovery enhancement: Opportunities and challenges. Applied Energy, 133, 374-387.

Hendraningrat, L., Li, S., & Torsæter, O. (2013). A coreflood investigation of nanofluid enhanced oil recovery. Journal of petroleum science and engineering, 111, 128-138.

Hendraningrat, L., & Torsaeter, O. (2014). Unlocking the potential of metal oxides nanoparticles to enhance the oil recovery. Paper presented at the offshore technology conference-Asia.

Hoelscher, K. P., De Stefano, G., Riley, M., & Young, S. (2012). Application of nanotechnology in drilling fluids. Paper presented at the SPE international oilfield nanotechnology conference and exhibition.

Hou, J., Qiu, M., He, X., Guo, C., Wei, M., & Bai, B. (2016). A dual-porosity-Stokes model and finite element method for coupling dual-porosity flow and free flow. SIAM Journal on Scientific Computing, 38(5), B710-B739.

Johnson, C. A., & Lenhoff, A. M. (1996). Adsorption of charged latex particles on mica studied by atomic force microscopy. Journal of colloid and interface science, 179(2), 587-599.

Kanj, M. Y., Rashid, M., & Giannelis, E. (2011). Industry first field trial of reservoir nanoagents. Paper presented at the SPE Middle East oil and gas show and conference.

Kim, I., Worthen, A. J., Lotfollahi, M., Johnston, K. P., DiCarlo, D. A., & Huh, C. (2017). Nanoparticle-stabilized emulsions for improved mobility control for adverse-mobility waterflooding. Paper presented at the IOR 2017-19th European Symposium on Improved Oil Recovery.

Krummel, A. T., Datta, S. S., Münster, S., & Weitz, D. A. (2013). Visualizing multiphase flow and trapped fluid configurations in a model three-dimensional porous medium. AIChE journal, 59(3), 1022-1029.

Kubik, T., Bogunia-Kubik, K., & Sugisaka, M. (2005). Nanotechnology on duty in medical applications. Current pharmaceutical biotechnology, 6(1), 17-33.

Kumari, A., Yadav, S. K., & Yadav, S. C. (2010). Biodegradable polymeric nanoparticles based drug delivery systems. Colloids and surfaces B: biointerfaces, 75(1), 1-18.

Kwok, M.-h., & Ngai, T. (2016). A confocal microscopy study of micron-sized poly (N-isopropylacrylamide) microgel particles at the oil–water interface and anisotopic flattening of highly swollen microgel. Journal of colloid and interface science, 461, 409-418.

Li, S., Hendraningrat, L., & Torsaeter, O. (2013). Improved oil recovery by hydrophilic silica nanoparticles suspension: 2 phase flow experimental studies. Paper presented at the IPTC 2013: International Petroleum Technology Conference.

Li, S., Torsæter, O., Lau, H. C., Hadia, N. J., & Stubbs, L. P. (2019). The impact of nanoparticle adsorption on transport and wettability alteration in water-wet Berea sandstone: an experimental study. Frontiers in Physics, 7, 74.

Li, X., ShamsiJazeyi, H., Pesek, S. L., Agrawal, A., Hammouda, B., & Verduzco, R. (2014). Thermoresponsive PNIPAAM bottlebrush polymers with tailored side-chain length and end-group structure. Soft Matter, 10(12), 2008-2015.

Liong, M., Lu, J., Kovochich, M., Xia, T., Ruehm, S. G., Nel, A. E. Zink, J. I. (2008). Multifunctional inorganic nanoparticles for imaging, targeting, and drug delivery. ACS nano, 2(5), 889-896.

Liu, M., Liu, Y., Li, J., Chen, S., Li, J., Su, L. Zhang, Z. (2015). Improvement of sphericity of thick-walled polystyrene shell. Colloids and Surfaces A: Physicochemical and Engineering Aspects, 484, 463-470.

Luo, D., Wang, F., Zhu, J., Cao, F., Liu, Y., Li, X. Ren, Z. (2016). Nanofluid of graphene-based amphiphilic Janus nanosheets for tertiary or enhanced oil recovery: High performance at low concentration. Proceedings of the National Academy of Sciences, 113(28), 7711-7716.

Metin, C., Bonnecaze, R., & Nguyen, Q. (2013). The viscosity of silica nanoparticle dispersions in permeable media. SPE Reservoir Evaluation & Engineering, 16(03), 327-332.

Mohammadizadeh, M., Pourabbas, B., Mahmoodian, M., Foroutani, K., & Fallahian, M. (2014). Facile and rapid production of conductive flexible films by deposition of polythiophene nanoparticles on transparent poly (ethyleneterephthalate): Electrical and morphological properties. Materials science in semiconductor processing, 20, 74-83.

Nguyen, P., Fadaei, H., & Sinton, D. (2014). Nanoparticle stabilized CO2 in water foam for mobility control in enhanced oil recovery via microfluidic method. Paper presented at the SPE Heavy Oil Conference-Canada.

Nikolov, A., Kondiparty, K., & Wasan, D. (2010). Nanoparticle self-structuring in a nanofluid film spreading on a solid surface. Langmuir, 26(11), 7665-7670.

Nikolov, A., & Wasan, D. (2003). Spreading of nanofluids on solids. Nature, 423(6936), 156-159.

Pan, X., Wang, L., Dai, J., Zhang, Q., Peng, T., & Chen, W. (2020). Analysis of China's oil and gas consumption under different scenarios toward 2050: An integrated modeling. Energy, 195, 116991.

Qin, T., Goual, L., Piri, M., Hu, Z., & Wen, D. (2020). Pore-scale dynamics of nanofluid-enhanced NAPL displacement in carbonate rock. Journal of contaminant hydrology, 230, 103598.

Rahmani, A. R., Bryant, S., Huh, C., Athey, A., Ahmadian, M., Chen, J., & Wilt, M. (2015). Crosswell magnetic sensing of superparamagnetic nanoparticles for subsurface applications. Spe Journal, 20(05), 1,067-061,082.

Ramasamy, J., & Amanullah, M. (2020). Nanocellulose for oil and gas field drilling and cementing applications. Journal of petroleum science and engineering, 184, 106292.

Rezaei, N., & Firoozabadi, A. (2014). Macro-and Microscale Waterflooding Performances of Crudes which form w/o Emulsions upon Mixing with Brines. Energy & fuels, 28(3), 2092-2103.

Roustaei, A. (2014). An evaluation of spontaneous imbibition of water into oil-wet carbonate reservoir cores using nanofluid. Petrophysics, 55(01), 31-37.

Saha, R., Uppaluri, R. V., & Tiwari, P. (2018). Silica nanoparticle assisted polymer flooding of heavy crude oil: emulsification, rheology, and wettability alteration characteristics. Industrial & Engineering Chemistry Research, 57(18), 6364-6376.

Saigal, T., Yoshikawa, A., Kloss, D., Kato, M., Golas, P. L., Matyjaszewski, K., & Tilton, R. D. (2013). Stable emulsions with thermally responsive microstructure and rheology using poly (ethylene oxide) star polymers as emulsifiers. Journal of colloid and interface science, 394, 284-292.

Saunders, B. R., & Turner, M. L. (2008). Nanoparticle–polymer photovoltaic cells. Advances in colloid and interface science, 138(1), 1-23.

ShamsiJazeyi, H., Miller, C. A., Wong, M. S., Tour, J. M., & Verduzco, R. (2014). Polymer- coated nanoparticles for enhanced oil recovery. Journal of applied polymer science, 131(15).

Shen, X., & Ye, L. (2011). Interfacial molecular imprinting in nanoparticle-stabilized emulsions. Macromolecules, 44(14), 5631-5637.

Son, H., Kim, H., Lee, G., Kim, J., & Sung, W. (2014). Enhanced oil recovery using nanoparticle-stabilized oil/water emulsions. Korean Journal of Chemical Engineering, 31(2), 338-342.

Soo, H., & Radke, C. (1984). Velocity effects in emulsion flow through porous media. Journal of colloid and interface science, 102(2), 462-476.

Soppimath, K. S., Aminabhavi, T. M., Kulkarni, A. R., & Rudzinski, W. E. (2001). Biodegradable polymeric nanoparticles as drug delivery devices. Journal of controlled release, 70(1-2), 1-20.

Tajik, S., Shahrabadi, A., Rashidi, A., Jalilian, M., & Yadegari, A. (2018). Application of functionalized silica-graphene nanohybrid for the enhanced oil recovery performance. Colloids and Surfaces A: Physicochemical and Engineering Aspects, 556, 253-265.

Thomas, S. (2008). Enhanced oil recovery-an overview. Oil & Gas Science and Technology-Revue de l'IFP, 63(1), 9-19.

Thompson, K. E., Willson, C. S., White, C. D., Nyman, S., Bhattacharya, J. P., & Reed, A. H. (2008). Application of a new grain-based reconstruction algorithm to microtomography images for quantitative characterization and flow modeling.

Tian, C., Feng, J., Cho, H. J., Datta, S. S., & Prud'homme, R. K. (2018). Adsorption and denaturation of structured polymeric nanoparticles at an interface. Nano letters, 18(8), 4854-4860.

Tian, S., Gao, W., Liu, Y., Kang, W., & Yang, H. (2020). Effects of surface modification Nano-SiO2 and its combination with surfactant on interfacial tension and emulsion stability. Colloids and Surfaces A: Physicochemical and Engineering Aspects, 124682.

Turkenburg, D., Chin, P., & Fischer, H. (2012). Use of modified nanoparticles in oil and gas reservoir management. Paper presented at the SPE International Oilfield Nanotechnology Conference and Exhibition.

Xu, K., Agrawal, D., & Darugar, Q. (2018). Hydrophilic nanoparticle-based enhanced oil recovery: microfluidic investigations on mechanisms. Energy & fuels, 32(11), 11243-11252.

Xu, K., Liang, T., Zhu, P., Qi, P., Lu, J., Huh, C., & Balhoff, M. (2017). A 2.5-D glass micromodel for investigation of multi-phase flow in porous media. Lab on a Chip, 17(4), 640-646.

Xu, K., Zhu, P., Huh, C., & Balhoff, M. T. (2015). Microfluidic investigation of nanoparticles' role in mobilizing trapped oil droplets in porous media. Langmuir, 31(51), 13673-13679.

Yang, Y., Cheng, T., Wu, H., You, Z., Shang, D., & Hou, J. (2020). Enhanced Oil Recovery Using Oleic Acid-Modified Titania Nanofluids: Underlying Mechanisms and Oil-Displacement Performance. Energy & fuels, 34(5), 5813-5822.

Yazhou, Z., Demin, W., Zhipeng, W., & Rui, C. (2017). The formation and viscoelasticity of pore-throat scale emulsion in porous media. Petroleum Exploration and Development, 44(1), 111-118.

Zhang, J., Li, L., Wang, S., Wang, J., Yang, H., Zhao, Z. Zhang, Z. (2015). Novel micro and nano particle-based drilling fluids: Pioneering approach to overcome the borehole instability problem in shale formations. Paper presented at the SPE Asia Pacific Unconventional Resources Conference and Exhibition.

Zhang, L., Abbaspourrad, A., Parsa, S., Tang, J., Cassiola, F. M., Zhang, M., Weitz, D. A. (2020). Core-shell Nanohydrogels with Programmable Swelling for Conformance Control in Porous Media. ACS Applied Materials & Interfaces.

Zhang, T., Davidson, D., Bryant, S. L., & Huh, C. (2010). Nanoparticle-stabilized emulsions for applications in enhanced oil recovery. Paper presented at the SPE improved oil recovery symposium.

Zhang, Y., Zhou, C., Qu, C., Wei, M., He, X., & Bai, B. (2019). Fabrication and verification of a glass–silicon–glass micro-/nanofluidic model for investigating multi-phase flow in shale-like unconventional dual-porosity tight porous media. Lab on a Chip, 19(24), 4071-4082.

Zhou, Y., Wu, X., Zhong, X., Reagen, S., Zhang, S., Sun, W. Zhao, J. X. (2020). Polymer nanoparticles based nano-fluid for enhanced oil recovery at harsh formation conditions. Fuel, 267, 117251.

Zhou, Y., Wu, X., Zhong, X., Sun, W., Pu, H., & Zhao, J. X. (2019). Surfactant-Augmented functional silica nanoparticle based nanofluid for enhanced oil recovery at high temperature and salinity. ACS Applied Materials & Interfaces, 11(49), 45763-45775.

SECTION

3. CONCLUSIONS AND RECOMMENDATIONS

3.1. CONCLUSIONS

This research has contributed to fabricate 1D, 2D and 3D micro-/nanofluidic models using lab-based, cost-effective, and time-saving methods. By using the fabricated micromodels, the fluid dynamics under seismic stimulation, fluid behavior in nanoconfined porous media and in-situ emulsification process during nanogel flooding were investigated. The conclusions reached from each paper are summarized as follow:

In Paper I, 1D Silanized-constricted tubes with high hydrophilicity were made to analyze the dynamic behavior of two immiscible fluids stimulated by a shaker. Three non-wetting fluids with different viscosities were used for the analysis. The motion of downstream meniscus and tube wall were tracked manually using a high-speed camera. The experimental amplitude amplification and absolute displacements in the oscillation experiments, as well as the critical acceleration amplitudes and absolute displacements in the mobilization experiments, were compared with the theoretical results. The experimental observation shows that a simple harmonic seismic stimulation can only cause a simple harmonic droplet oscillation response without higher modes of vibration in an overdamped condition. The oscillation experiments show that the amplitude amplification decreases monotonically with the frequency, and the effect of viscosity in the range we considered on the amplitude amplification-frequency relationship is not significant when the flow is in an overdamped condition. The mobilization experiments show that the

critical acceleration amplitude could be affected by both the resonance of the droplet and the initial trapping position of the front meniscus. Droplet resonance not occurring at a small input acceleration amplitude could occur at a large input acceleration amplitude due to the nonlinearity of the droplet oscillation system. When resonance occurs, it can help reduce the required critical acceleration amplitude to mobilize the droplet. The effect of initial trapping position of the front meniscus can be comparable to or even greater than the effect of the frequency on the critical acceleration amplitude. In the experiment, droplet mobilization could be achieved after multiple periods of vibration instead of occurring suddenly. Based on the comparisons of the experimental and theoretical results, we concluded that the theoretical model was reliable for predicting the dynamics of the non-wetting droplet in response to seismic stimulation in the experiments with different combinations of critical experimental parameters considered in this study. The minor discrepancy between the experimental and theoretical results can be explained by the known limitations of the theoretical model.

In Paper II, 2D fully transparent, shale-like dual-porosity glass-silicon-glass micro-/nanofluidic model was successfully fabricated using e-beam physical evaporation deposition, lift-off process and anodic bonding method in a simple, fast and low-cost way. The fabrication process gets rid of the time-consuming and complicated etching method while still generates complex porous media network with uniform channels in a much shorter time. To verify the functionally and practicability of the model, two phase fluid flow displacement experiments with two injection modes were conducted separately and visualized using confocal laser scanning microscope. Owing to the large width-to-depth

ratio range (12-2000) of the model, especially for two conduits at top and bottom, the fingering phenomena that may happen in a Hele-Shaw cell were brought into sight.

Moreover, we observed that it is possible the fingering problem could exist when displacing phase viscosity is higher than that of the displaced phase due to the geometry of the porous media. Besides, the residual oil distributed as different forms in the matrixes, micro-fractures and conduits. Snap-offed oil droplets trapped in thin channel pore throat, oil chains left in the wider matrix channels, boundary-adhered oil films due to the surface roughness, and the dispersed oil droplets in the conduits were found, respectively. By changing the flow pattern by shifting two matrixes adjacent to the bottom and then top conduits, we demonstrated that different matrix/micro- fracture/ macro-fracture interlacing geometries that may affect flow patterns, which would affect the oil recovery seriously for dual-porosity heterogeneous shale porous media.

In Paper III, 3D transparent glass beads packed micromodel was built to directly visualize polymeric nanoparticles with fluorescent dye on emulsifying the remaining oil droplets during the nanogel flooding under different flow rates using the confocal microscope. Under dynamic local visualization mode, we captured the in-situ emulsification process and demonstrated two scenarios. For the successful emulsification scenario, we found the bulk form of remaining oil clusters after water flooding were emulsified by nanogels into small oil droplets and some of the emulsion droplets were trapped in the end of the nanogel flooding. For the unsuccessful one, we found some bigger droplets cannot be displaced and emulsified through the pore throat due to the capillary pressure and the nanogels were found adsorbed on the droplet front meniscus the most. Potential mechanisms for in-situ

emulsification by nanogels were proposed and discussed. Under static global mode, we segmented the remaining oil droplets before and after nanogel flooding and their sphericity and diameter changes were compared and analyzed under different flow rates. The oil recovery for each experiment was shown enhanced by nanogel flooding, proving the feasibility of the nanogel as a potential EOR agent.

3.2. RECOMMENDATIONS

Although the 2D micro-/nanofluidic model provides with a quick and simple platform for direct visualizing the fluid flow dynamically in a dual-scale porous media, there are still further expectations for the future work. The micro-/nanofluidic model can be improved by designing more different patterns that representing more complicated reservoir conditions. The limitation of depth-to-width aspect ratio by using glass-glass anodic bonding method still needs further investigated, which would provide the possibility of fabricating the micromodel even at sub-10 nm scale. The residual oil distribution, flow velocity, pressure difference and fingering problem are still need further researched quantitatively and systematically to get a comprehensive understanding of the fluid flow within dual-scale micro-/nano channels at pore level.

Besides, the in-situ emulsion by nanogels for EOR still need further research using the 3D micromodel. The wettability effect on nanogel in-situ emulsification could be investigated by altering the glass beads originally to hydrophobic instead of hydrophilic. Besides, nanogel concentration and the surface charges effect could also be studied for better understanding the in-situ emulsion generation and transportation under different conditions.

REFERENCES

Alzahid, Y. A., Mostaghimi, P., Gerami, A., Singh, A., Privat, K., Amirian, T., & Armstrong, R. T. (2018). Functionalisation of polydimethylsiloxane (PDMS)-microfluidic devices coated with rock minerals. Scientific reports, 8(1), 1-15.

Amani, H. (2015). Study of enhanced oil recovery by rhamnolipids in a homogeneous 2D micromodel. Journal of petroleum science and engineering, 128, 212-219.

Armstrong, R. T., & Wildenschild, D. (2012). Investigating the pore-scale mechanisms of microbial enhanced oil recovery. Journal of petroleum science and engineering, 94, 155-164.

Au, A. K., Huynh, W., Horowitz, L. F., & Folch, A. (2016). 3D-printed microfluidics. Angewandte Chemie International Edition, 55(12), 3862-3881.

Blunt, M. J., Bijeljic, B., Dong, H., Gharbi, O., Iglauer, S., Mostaghimi, P. Pentland, C. (2013). Pore-scale imaging and modelling. Advances in Water resources, 51, 197-216.

Bora, R., Maini, B., & Chakma, A. (2000). Flow visualization studies of solution gas drive process in heavy oil reservoirs using a glass micromodel. SPE Reservoir Evaluation & Engineering, 3(03), 224-229.

Bounds, C. O., Upadhyay, J., Totaro, N., Thakuri, S., Garber, L., Vincent, M. Pojman, J.A. (2013). Fabrication and characterization of stable hydrophilic microfluidic devices prepared via the in situ tertiary-amine catalyzed michael addition of multifunctional thiols to multifunctional acrylates. ACS Applied Materials & Interfaces, 5(5), 1643-1655.

Bowden, S. A., Tanino, Y., Akamairo, B., & Christensen, M. (2016). Recreating mineralogical petrographic heterogeneity within microfluidic chips: assembly, examples, and applications. Lab on a Chip, 16(24), 4677-4681.

Bu, M., Melvin, T., Ensell, G. J., Wilkinson, J. S., & Evans, A. G. (2004). A new masking technology for deep glass etching and its microfluidic application. Sensors and Actuators A: Physical, 115(2-3), 476-482.

Buchgraber, M., Kovscek, A. R., & Castanier, L. M. (2012). A study of microscale gas trapping using etched silicon micromodels. Transport in porous media, 95(3), 647-668.

Bultreys, T., De Boever, W., & Cnudde, V. (2016). Imaging and image-based fluid transport modeling at the pore scale in geological materials: A practical introduction to the current state-of-the-art. Earth-Science Reviews, 155, 93-128.

Castano-Alvarez, M., Ayuso, D. F. P., Granda, M. G., Fernández-Abedul, M. T., García, J. R., & Costa-García, A. (2008). Critical points in the fabrication of microfluidic devices on glass substrates. Sensors and Actuators B: Chemical, 130(1), 436-448.

Chang, C., Kneafsey, T. J., Wan, J., Tokunaga, T. K., & Nakagawa, S. (2020). Impacts of Mixed-Wettability on Brine Drainage and Supercritical CO2 Storage Efficiency in a 2.5 - D Heterogeneous Micromodel. Water Resources Research, e2019WR026789.

Chatenever, A., & Calhoun Jr, J. C. (1952). Visual examinations of fluid behavior in porous media-part i. Journal of petroleum technology, 4(06), 149-156.

Conn, C. A., Ma, K., Hirasaki, G. J., & Biswal, S. L. (2014). Visualizing oil displacement with foam in a microfluidic device with permeability contrast. Lab on a Chip, 14(20), 3968-3977.

Crandall, D., Ahmadi, G., Leonard, D., Ferer, M., & Smith, D. H. (2008). A new stereolithography experimental porous flow device. Review of Scientific Instruments, 79(4), 044501.

Datta, S. S., Dupin, J.-B., & Weitz, D. A. (2014). Fluid breakup during simultaneous two-phase flow through a three-dimensional porous medium. Physics of Fluids, 26(6), 062004.

Datta, S. S., Ramakrishnan, T., & Weitz, D. A. (2014). Mobilization of a trapped non-wetting fluid from a three-dimensional porous medium. Physics of Fluids, 26(2), 022002.

Do Nascimento, D. F., Junior, J. R. V., Paciornik, S., & Carvalho, M. S. (2019). Pore scale visualization of drainage in 3D porous media by confocal microscopy. Scientific reports, 9(1), 1-11.

Doryani, H., Malayeri, M., & Riazi, M. (2016). Visualization of asphaltene precipitation and deposition in a uniformly patterned glass micromodel. Fuel, 182, 613-622.

Gad-el-Hak, M. (1999). The fluid mechanics of microdevices—the Freeman scholar lecture.

George, D., Hayat, O., & Kovscek, A. (2005). A microvisual study of solution-gas-drive mechanisms in viscous oils. Journal of petroleum science and engineering, 46(1-2), 101-119.

Gerami, A., Armstrong, R. T., Johnston, B., Warkiani, M. E., Mosavat, N., & Mostaghimi, P. (2017). Coal-on-a-chip: visualizing flow in coal fractures. Energy & fuels, 31(10), 10393-10403.

Gitlin, L., Schulze, P., Ohla, S., Bongard, H. J., & Belder, D. (2015). Surface modification of PDMS microfluidic devices by controlled sulfuric acid treatment and the application in chip electrophoresis. Electrophoresis, 36(3), 449-456.

Grate, J. W., Kelly, R. T., Suter, J., & Anheier, N. C. (2012). Silicon-on-glass pore network micromodels with oxygen-sensing fluorophore films for chemical imaging and defined spatial structure. Lab on a Chip, 12(22), 4796-4801.

Grate, J. W., Warner, M. G., Pittman, J. W., Dehoff, K. J., Wietsma, T. W., Zhang, C., & Oostrom, M. (2013). Silane modification of glass and silica surfaces to obtain equally oil-wet surfaces in glass-covered silicon micromodel applications. Water Resources Research, 49(8), 4724-4729.

Heshmati, M., & Piri, M. (2014). Experimental investigation of dynamic contact angle and capillary rise in tubes with circular and noncircular cross sections. Langmuir, 30(47), 14151-14162.

Hiller, T., Ardevol-Murison, J., Muggeridge, A., Schröter, M., & Brinkmann, M. (2019). The Impact of Wetting-Heterogeneity Distribution on Capillary Pressure and Macroscopic Measures of Wettability. Spe Journal, 24(01), 200-214.

Hu, R., Wan, J., Kim, Y., & Tokunaga, T. K. (2017). Wettability effects on supercritical CO2–brine immiscible displacement during drainage: Pore-scale observation and 3D simulation. International Journal of Greenhouse Gas Control, 60, 129-139.

Iliescu, C., Chen, B., & Miao, J. (2008). On the wet etching of Pyrex glass. Sensors and Actuators A: Physical, 143(1), 154-161.

Iliescu, C., Taylor, H., Avram, M., Miao, J., & Franssila, S. (2012). A practical guide for the fabrication of microfluidic devices using glass and silicon. Biomicrofluidics, 6(1), 016505.

Ishutov, S., Hasiuk, F. J., Fullmer, S. M., Buono, A. S., Gray, J. N., & Harding, C. (2017). Resurrection of a reservoir sandstone from tomographic data using three-dimensional printing. AAPG bulletin, 101(9), 1425-1443.

Jatukaran, A., Zhong, J., Abedini, A., Sherbatian, A., Zhao, Y., Jin, Z. Sinton, D. (2019). Natural gas vaporization in a nanoscale throat connected model of shale: multi-scale, multi-component and multi-phase. Lab on a Chip, 19(2), 272-280.

Karadimitriou, N., Musterd, M., Kleingeld, P., Kreutzer, M., Hassanizadeh, S., & Joekar-Niasar, V. (2013). On the fabrication of PDMS micromodels by rapid prototyping, and their use in two-phase flow studies. Water Resources Research, 49(4), 2056-2067.

Karadimitriou, N. K., Mahani, H., Steeb, H., & Niasar, V. (2019). Nonmonotonic Effects of Salinity on Wettability Alteration and Two-Phase Flow Dynamics in PDMS Micromodels. Water Resources Research, 55(11), 9826-9837.

Kazemifar, F., Blois, G., Kyritsis, D. C., & Christensen, K. T. (2015). A methodology for velocity field measurement in multiphase high-pressure flow of CO2 and water in micromodels. Water Resources Research, 51(4), 3017-3029.

Keller, A. A., Blunt, M. J., & Roberts, A. P. V. (1997). Micromodel observation of the role of oil layers in three-phase flow. Transport in porous media, 26(3), 277-297.

Kong, L., Ostadhassan, M., Liu, B., Li, C., & Liu, K. (2019). Multifractal Characteristics of MIP-Based Pore Size Distribution of 3D-Printed Powder-Based Rocks: A Study of Post-Processing Effect. Transport in porous media, 129(2), 599-618.

Kong, L., Ostadhassan, M., Zamiran, S., Liu, B., Li, C., & Marino, G. G. (2019). Geomechanical Upscaling Methods: Comparison and Verification via 3D Printing. Energies, 12(3), 382.

Krummel, A. T., Datta, S. S., Münster, S., & Weitz, D. A. (2013). Visualizing multiphase flow and trapped fluid configurations in a model three-dimensional porous medium. AIChE journal, 59(3), 1022-1029.

Kutchoukov, V., Laugere, F., van Der Vlist, W., Pakula, L., Garini, Y., & Bossche, A. (2004). Fabrication of nanofluidic devices using glass-to-glass anodic bonding. Sensors and Actuators A: Physical, 114(2-3), 521-527.

Lee, H., Lee, S. G., & Doyle, P. S. (2015). Photopatterned oil-reservoir micromodels with tailored wetting properties. Lab on a Chip, 15(14), 3047-3055.

Lee, J. N., Park, C., & Whitesides, G. M. (2003). Solvent compatibility of poly (dimethylsiloxane)-based microfluidic devices. Analytical chemistry, 75(23), 6544-6554.

Lee, S. G., Lee, H., Gupta, A., Chang, S., & Doyle, P. S. (2016). Site-Selective In Situ Grown Calcium Carbonate Micromodels with Tunable Geometry, Porosity, and Wettability. Advanced Functional Materials, 26(27), 4896-4905.

Li, H., Raza, A., Ge, Q., Lu, J.-Y., & Zhang, T. (2020). Empowering microfluidics by micro- 3D printing and solution-based mineral coating. Soft Matter, 16(29), 6841-6849.

Li, S., & Torsæter, O. (2014). An experimental investigation of EOR mechanisms for nanoparticles fluid in glass micromodel. Paper presented at the Paper SCA2014-022 was prepared for presentation at the International Symposium of the Society of Core Analysts held in Avignon, France.

Lifton, V. A. (2016). Microfluidics: an enabling screening technology for enhanced oil recovery (EOR). Lab on a Chip, 16(10), 1777-1796.

Liu, Z., Li, Y., Luan, H., Gao, W., Guo, Y., & Chen, Y. (2019). Pore scale and macroscopic visual displacement of oil-in-water emulsions for enhanced oil recovery. Chemical Engineering Science, 197, 404-414.

Lv, M., Liu, Z., Ji, C., Jia, L., & Jiang, Y. (2018). Investigation of Pore-Scale Behaviors of Foam Flow in a Polydimethylsiloxane Micromodel. Industrial & Engineering Chemistry Research, 57(44), 15172-15180.

Lv, M., Liu, Z., Jia, L., & Ji, C. (2020). Visualizing pore-scale foam flow in micromodels with different permeabilities. Colloids and Surfaces A: Physicochemical and Engineering Aspects, 124923.

Ma, K., Rivera, J., Hirasaki, G. J., & Biswal, S. L. (2011). Wettability control and patterning of PDMS using UV–ozone and water immersion. Journal of colloid and interface science, 363(1), 371-378.

Maghzi, A., Mohammadi, S., Ghazanfari, M. H., Kharrat, R., & Masihi, M. (2012). Monitoring wettability alteration by silica nanoparticles during water flooding to heavy oils in five-spot systems: A pore-level investigation. Experimental Thermal and Fluid Science, 40, 168-176.

Marcinkevičius, A., Juodkazis, S., Watanabe, M., Miwa, M., Matsuo, S., Misawa, H., & Nishii, J. (2001). Femtosecond laser-assisted three-dimensional microfabrication in silica. Optics Letters, 26(5), 277-279.

Marin, A. C., Grossi, T., Bianchi, E., Dubini, G., & Lacroix, D. (2017). 2D μ-particle image velocimetry and computational fluid dynamics study within a 3D porous scaffold. Annals of biomedical engineering, 45(5), 1341-1351.

Meybodi, H. E., Kharrat, R., & Araghi, M. N. (2011). Experimental studying of pore morphology and wettability effects on microscopic and macroscopic displacement efficiency of polymer flooding. Journal of petroleum science and engineering, 78(2), 347-363.

Mittal, K. L. (2007). Silanes and other coupling agents (Vol. 4): CRC Press.

Murison, J., Semin, B., Baret, J.-C., Herminghaus, S., Schröter, M., & Brinkmann, M. (2014). Wetting heterogeneities in porous media control flow dissipation. Physical Review Applied, 2(3), 034002.

Nguyen, P., Fadaei, H., & Sinton, D. (2014). Pore-scale assessment of nanoparticle-stabilized CO2 foam for enhanced oil recovery. Energy & fuels, 28(10), 6221- 6227.

Oosterbroek, R., Hermes, D., Kakuta, M., Benito-Lopez, F. Gardeniers, J., Verboom, W., . . . van den Berg, A. (2006). Fabrication and mechanical testing of glass chips for high-pressure synthetic or analytical chemistry. Microsystem technologies, 12(5), 450-454.

Osei-Bonsu, K., Grassia, P., & Shokri, N. (2017). Investigation of foam flow in a 3D printed porous medium in the presence of oil. Journal of colloid and interface science, 490, 850-858.

Porter, M. L., Jiménez-Martínez, J., Martinez, R., McCulloch, Q., Carey, J. W., & Viswanathan, H. S. (2015). Geo-material microfluidics at reservoir conditions for subsurface energy resource applications. Lab on a Chip, 15(20), 4044-4053.

Ren, K., Zhou, J., & Wu, H. (2013). Materials for microfluidic chip fabrication. Accounts of chemical research, 46(11), 2396-2406.

Rostami, P., Sharifi, M., Aminshahidy, B., & Fahimpour, J. (2019). The effect of nanoparticles on wettability alteration for enhanced oil recovery: micromodel experimental studies and CFD simulation. Petroleum Science, 16(4), 859-873.

Sandengen, K., Kristoffersen, A., Melhuus, K., & Jøsang, L. O. (2016). Osmosis as mechanism for low-salinity enhanced oil recovery. Spe Journal, 21(04), 1,227-221,235.

Schneider, M., Kozlov, B., Willaime, H., Tran, Y., Rezgui, F., & Tabeling, P. (2010). Wettability patterning in microfluidic systems by poly (acrylic acid) graft polymerization. Paper presented at the conference MicroTas.

Schneider, M. H., & Tabeling, P. (2011). Lab-on-chip methodology in the energy industry: wettability patterns and their impact on fluid displacement in oil reservoir models. American Journal of Applied Sciences, 8(10), 927.

Singh, R., Sivaguru, M., Fried, G. A., Fouke, B. W., Sanford, R. A., Carrera, M., & Werth, C.J. (2017). Real rock-microfluidic flow cell: A test bed for real-time in situ analysis of flow, transport, and reaction in a subsurface reactive transport environment. Journal of contaminant hydrology, 204, 28-39.

Sohrabi, M., Tehrani, D., Danesh, A., & Henderson, G. (2001). Visualisation of oil recovery by water alternating gas (WAG) injection using high pressure micromodels-oil-wet & mixed-wet systems. Paper presented at the SPE Annual Technical Conference and Exhibition.

Song, W., de Haas, T. W., Fadaei, H., & Sinton, D. (2014). Chip-off-the-old-rock: the study of reservoir-relevant geological processes with real-rock micromodels. Lab on a Chip, 14(22), 4382-4390.

Song, W., & Kovscek, A. R. (2015). Functionalization of micromodels with kaolinite for investigation of low salinity oil-recovery processes. Lab on a Chip, 15(16), 3314-3325.

Song, W., & Kovscek, A. R. (2016). Direct visualization of pore-scale fines migration and formation damage during low-salinity waterflooding. Journal of Natural Gas Science and Engineering, 34, 1276-1283.

Soulaine, C., Roman, S., Kovscek, A., & Tchelepi, H. A. (2017). Mineral dissolution and wormholing from a pore-scale perspective. Journal of Fluid Mechanics, 827, 457-483.

Sun, Q., Li, Z., Li, S., Jiang, L., Wang, J., & Wang, P. (2014). Utilization of surfactant-stabilized foam for enhanced oil recovery by adding nanoparticles. Energy & fuels, 28(4), 2384-2394.

Tagavifar, M., Xu, K., Jang, S. H., Balhoff, M. T., & Pope, G. A. (2017). Spontaneous and flow-driven interfacial phase change: dynamics of microemulsion formation at the pore scale. Langmuir, 33(45), 13077-13086.

Tiggelaar, R. M., Benito-López, F., Hermes, D. C., Rathgen, H., Egberink, R. J., Mugele, F. G. Gardeniers, H. J. (2007). Fabrication, mechanical testing and application of high-pressure glass microreactor chips. Chemical Engineering Journal, 131(1-3), 163-170.

Vavra, E. D., Zeng, Y., Xiao, S., Hirasaki, G. J., & Biswal, S. L. (2018). Microfluidic Devices for Characterizing Pore-scale Event Processes in Porous Media for Oil Recovery Applications. JoVE (Journal of Visualized Experiments)(131), e56592.

Wan, J., Tokunaga, T. K., Tsang, C. F., & Bodvarsson, G. S. (1996). Improved glass micromodel methods for studies of flow and transport in fractured porous media. Water Resources Research, 32(7), 1955-1964.

Wang, W., Chang, S., & Gizzatov, A. (2017). Toward reservoir-on-a-chip: fabricating reservoir micromodels by in situ growing calcium carbonate nanocrystals in microfluidic channels. ACS Applied Materials & Interfaces, 9(34), 29380-29386.

Wu, M., Xiao, F., Johnson-Paben, R. M., Retterer, S. T., Yin, X., & Neeves, K. B. (2012). Single-and two-phase flow in microfluidic porous media analogs based on Voronoi tessellation. Lab on a Chip, 12(2), 253-261.

Wu, Q., Bai, B., Ma, Y., Ok, J. T., Yin, X., & Neeves, K. (2014). Optic imaging of two-phase- flow behavior in 1D nanoscale channels. Spe Journal, 19(05), 793-802.

Wu, Q., Ok, J. T., Sun, Y., Retterer, S., Neeves, K. B., Yin, X. Ma, Y. (2013). Optic imaging of single and two-phase pressure-driven flows in nano-scale channels. Lab on a Chip, 13(6), 1165-1171.

Xu, K., Agrawal, D., & Darugar, Q. (2018). Hydrophilic nanoparticle-based enhanced oil recovery: microfluidic investigations on mechanisms. Energy & fuels, 32(11), 11243-11252.

Xu, K., Bonnecaze, R., & Balhoff, M. (2017). Egalitarianism among bubbles in porous media: an ostwald ripening derived anticoarsening phenomenon. Physical review letters, 119(26), 264502.

Xu, K., Liang, T., Zhu, P., Qi, P., Lu, J., Huh, C., & Balhoff, M. (2017). A 2.5-D glass micromodel for investigation of multi-phase flow in porous media. Lab on a Chip, 17(4), 640-646.

Xu, W., Ok, J. T., Xiao, F., Neeves, K. B., & Yin, X. (2014). Effect of pore geometry and interfacial tension on water-oil displacement efficiency in oil-wet microfluidic porous media analogs. Physics of Fluids, 26(9), 093102.

Yeh, H.-L., & Juárez, J. J. (2019). Oil phase displacement by acoustic streaming in a reservoir-on-a-chip. Microfluidics and Nanofluidics, 23(10), 113.

Zhang, L., Abbaspourrad, A., Parsa, S., Tang, J., Cassiola, F. M., Zhang, M. Weitz, D. A. (2020). Core-shell Nanohydrogels with Programmable Swelling for Conformance Control in Porous Media. ACS Applied Materials & Interfaces.

Zhang, Y., Zhou, C., Qu, C., Wei, M., He, X., & Bai, B. (2019). Fabrication and verification of a glass–silicon–glass micro-/nanofluidic model for investigating multi-phase flow in shale-like unconventional dual-porosity tight porous media. Lab on a Chip, 19(24), 4071-4082.

Zhong, J., Abedini, A., Xu, L., Xu, Y., Qi, Z., Mostowfi, F., & Sinton, D. (2018). Nanomodel visualization of fluid injections in tight formations. Nanoscale, 10(46), 21994- 22002.

VITA

Yandong Zhang was born in Karamay, Xinjiang Province, China. He was admitted to the China University of Petroleum - Beijing (CUPB), Beijing, China in Sep. 2009 and received his bachelor's degree in Geological Engineering in Jun. 2013. He later joined Dr. Baojun Bai's research group in Aug. 2013 and received his Master of Science in Petroleum Engineering from Missouri University of Science and Technology, U.S. in Dec. 2015. He continued to pursue a Ph.D. degree in the same research group and received his Doctor of Philosophy in Petroleum Engineering from Missouri University of Science and Technology in December 2020.